Kinematic Correction for Energy Resolution Improvement Using a Position Sensitive Detector

Ossama A. Abouzeid
Department of Physics
University of Manitoba
Winnipeg, Man., Canada.

A thesis submitted to the Faculty of Graduate Studies of the University of Manitoba in partial fulfillment of the requirements for the Degree of Master of Science

February 1977

"KINEMATIC CORRECTION FOR ENERGY RESOLUTION IMPROVEMENT USING A POSITION SENSITIVE DETECTOR"

by

OSSAMA A. ABOUZEID

A dissertation submitted to the Faculty of Graduate Studies of the University of Manitoba in partial fulfillment of the requirements of the degree of

MASTER OF SCIENCE

TO MY PARENTS

ACKNOWLEDGMENTS

I would like to express my gratitude to my advisor Dr. W.R. Falk for his assistance and guidance during this work. I would like also to thank Dr. L.Ph. Roesch and Dr. P. Debenham for their help.

In addition I would like to thank the members of the electronic and mechanical shops.

Finally I would like to express my appreciation for the financial support given by Physics Department and Cyclotron Laboratory .

Abstract

A technique has been developed that improves the energy resolution in scattering experiments that use a highly divergent accelarator beam.

The technique is described in the main body of this thesis and involves shifting the usual beam waist (an upright phase space ellipse) at the target position to a point downstream from the target. The distance to which the waist should be moved depends on the scattering angle, target angle, and the beam properties.

The technique was tested by computer program and an improvement in the energy resolution by a factor of 4 - 8 was obtained. Experimental measurements on carbon and hydrogen targets were performed using a position sensitive detector. The results showed the technique to be effective. Angular resolution is improved as a consequence of energy resolution improvement.

The introductory chapter contains a summary of the details and the design consideration of the momentum analysis system of the high resolution beam line. An understanding of the entire system is mandatory for the experimental tests of the theory put forward in this thesis.

contents

List of tables

List of Figures

Introduction

The beam delivered by the momentum analysis system of the high resolution beam line of the University of Manitoba Cyclotron will result in an angular divergence of up to $\pm 2^{\circ}$ on the target. The kinematic energy resulting from this divergence is very serious for the lighter nuclei where the kinematic energy spread per degree is large. For heavier nuclei, where the kinematic energy spread may not be serious, this angular divergence may, however, be unacceptably large for measurement of an angular distribution.

This thesis describes a technique that improves remarkably the energy resolution in scattering experiments, and results in a corresponding improvement in the angular resolution of the experiment. The latter point is of importance in studying angular distributions that vary rapidly with angle, while utilizing the full beam acceptance. The technique involves shifting the usual beam waist at the target position to a point downstream from the target. A similar technique, known as dispersion matching[15], is well known and applied in magnetic spectrograph detector systems which are matched to the characteristics of the beam incident on target by appropriate shifting of the strengths of quadrupole singlets in the transport system to give a dipersion such that all

particles (for certain reaction) are brought to the same point in the focal plane of the spectrograph. The detector system used in this work is a more conventional one comprising a solid state position sensitive detector with a solid angle of up to 7 mstr, where the position information can be used to apply kinematic correction from the angular information.

The thesis is divided into 4 chapters and is comprised of two parts. The first is described in chapter 1 and represents a summary of the essential design considerations, beam behaviour, and the details of the momentum analysis system of the high resolution beam line. This work was done mainly by P. Debenham and W. Falk during the period 1970 1974[1]. Furthermore, the effect of the second-order aberrations on the quality of the image at the focal plane of the analysis system has been investigated.

The second part of this thesis then represents a description of the technique mentioned earlier to improve the energy resolution and it is described in the remaining 3 chapters.

Chapter 2 describes the theory and conditions that should be satisfied in order to improve the energy resolution. It also contains the theoretical calculations done to test the theory using a special computer program.

Chapter 3 contains the experimental procedure, electronics used, and description of the computer programs used with the position sensitive detector.

Chapter 4 describes all the experimental results obtained for the reactions $^{12}C(p, \ )^{9}B$, and $^{1}H(p,p)^{1}H$. Also it gives a comparison between the measured energy resolution improvement and the energy resolution improvement predicted by the theory.

CHAPTER 1

High Resolution Beam Analysis System

1.1 Introduction

The high resolution beam analysis system has been designed to accept as an input a beam of emittance as high as 15 mm.mrad (half width times half divergence) and provide at the targrt position a beam of intensity 1% of the intensity on slits s1 shown in fiq(1.1) , and a final intirinsic energy resolution $\frac{\Delta E}{E} = 5 \times 10^{-4}$ (1).

The system was built on the 15° right beam line.For economic reasons and space limitation the system was choosen to consist of two 90° single focusinq analyzinq magnets of 30 in. radius .The two maqnets bend in opposite directions to each other,so in this way the dispersions of the two magnets will add (3).
Technical data for the two analyzinq maqnets is qiven in Table(1.1). Fiq(1.2)shows a schematic diaqram for the maqnet pole piece .

1.2 System Layout

Fiq(1.3) shows the layout of the system . It should be noticed that the dimensions indicated are measured between the effective field boundaries (EFB) of maqnets and centre of slits.

1.3 Uniform Field Measurement

The average fields on the central orbit in both magnets were measured using Hall probe type BHT 910 .

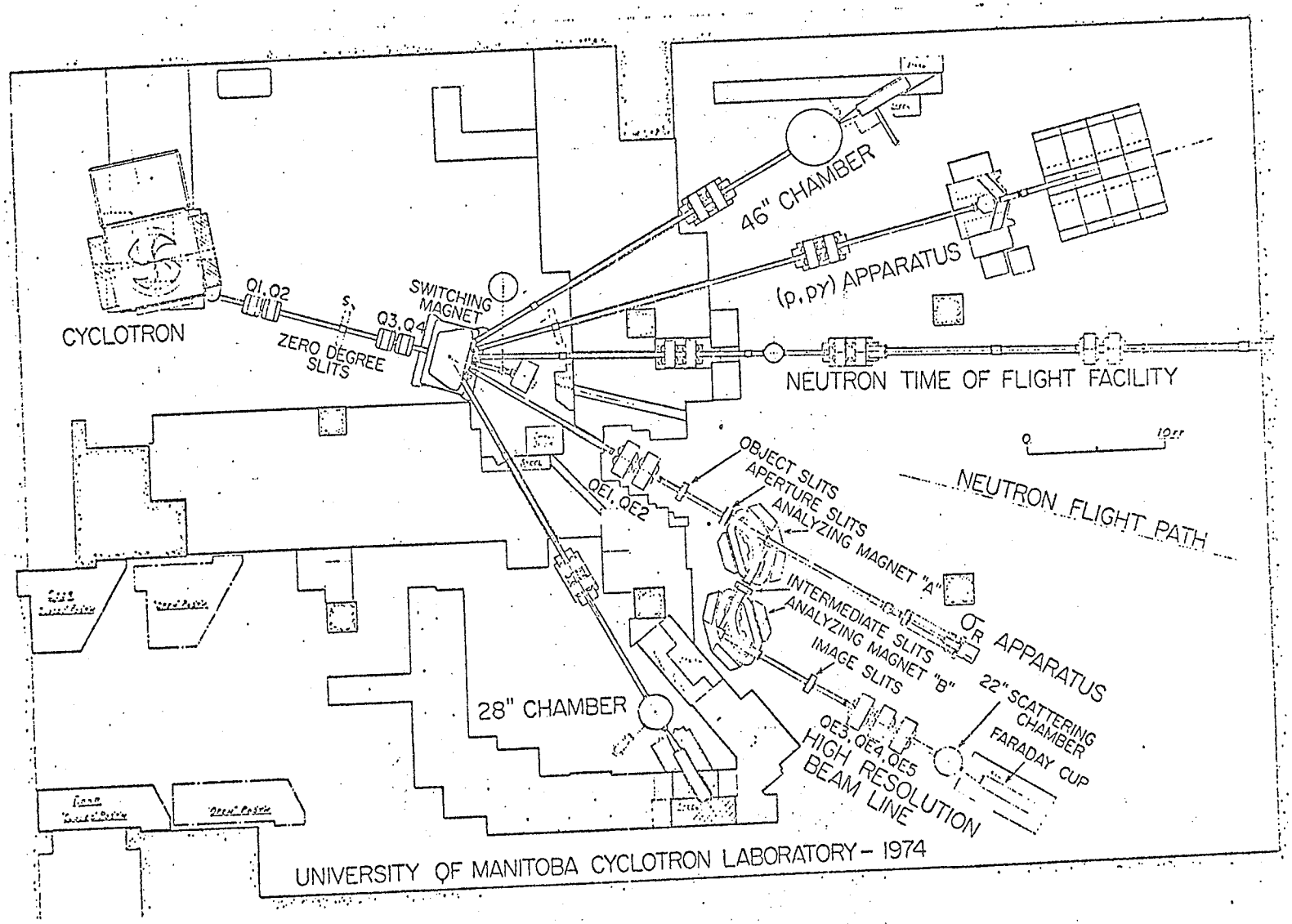
CYCLOTRON
Q1, Q2
ZERO DEGREE SLITS
Q3, Q4
SWITCHING MAGNET
46" CHAMBER
(p, pγ) APPARATUS
NEUTRON TIME OF FLIGHT FACILITY
NEUTRON FLIGHT PATH
OBJECT SLITS
APERTURE SLITS
ANALYZING MAGNET "A"
QE1, QE2
INTERMEDIATE SLITS
ANALYZING MAGNET "B"
IMAGE SLITS
QR APPARATUS
22" SCATTERING CHAMBER
FARADAY CUP
QE3, QE4, QE5
HIGH RESOLUTION BEAM LINE
28" CHAMBER
UNIVERSITY OF MANITOBA CYCLOTRON LABORATORY – 1974

Fig (1.1)

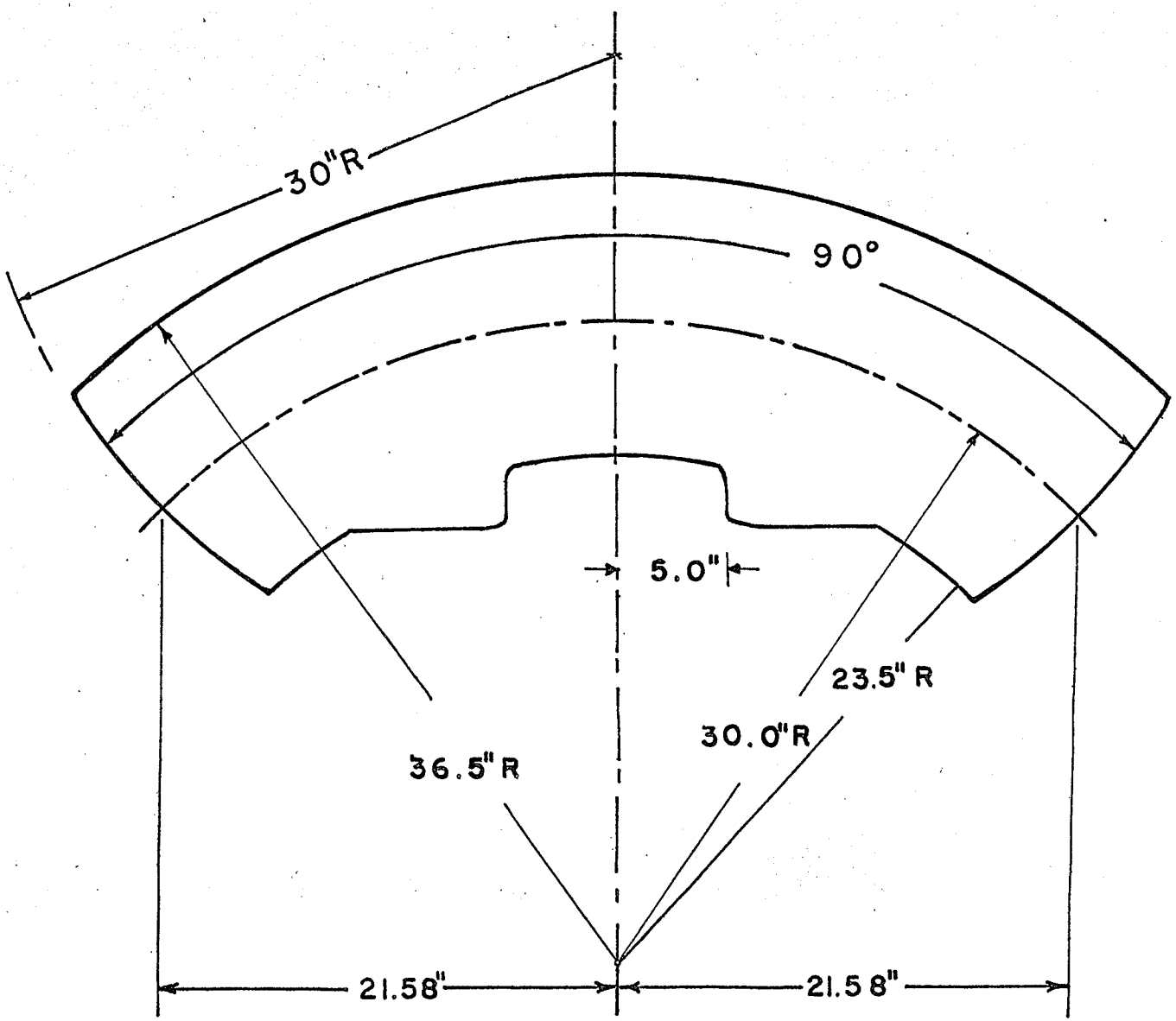

Fig (1.2) The Analyzing Magnet

TABLE (1.1)

ANALYZING MAGNET DATA

Bending radius	30 in.
Magnetic bending angle	90°
Air gap	1.75 in.
Pole width	13 in.
Max. field	14 KG
Entrance angle	0°
Exit angle	0°
Curvature of entrance angle	30 in.
Curvature of exit edge	30 in.
EFB (inside the pole root)	0.52 in.
Magnetic field index	0

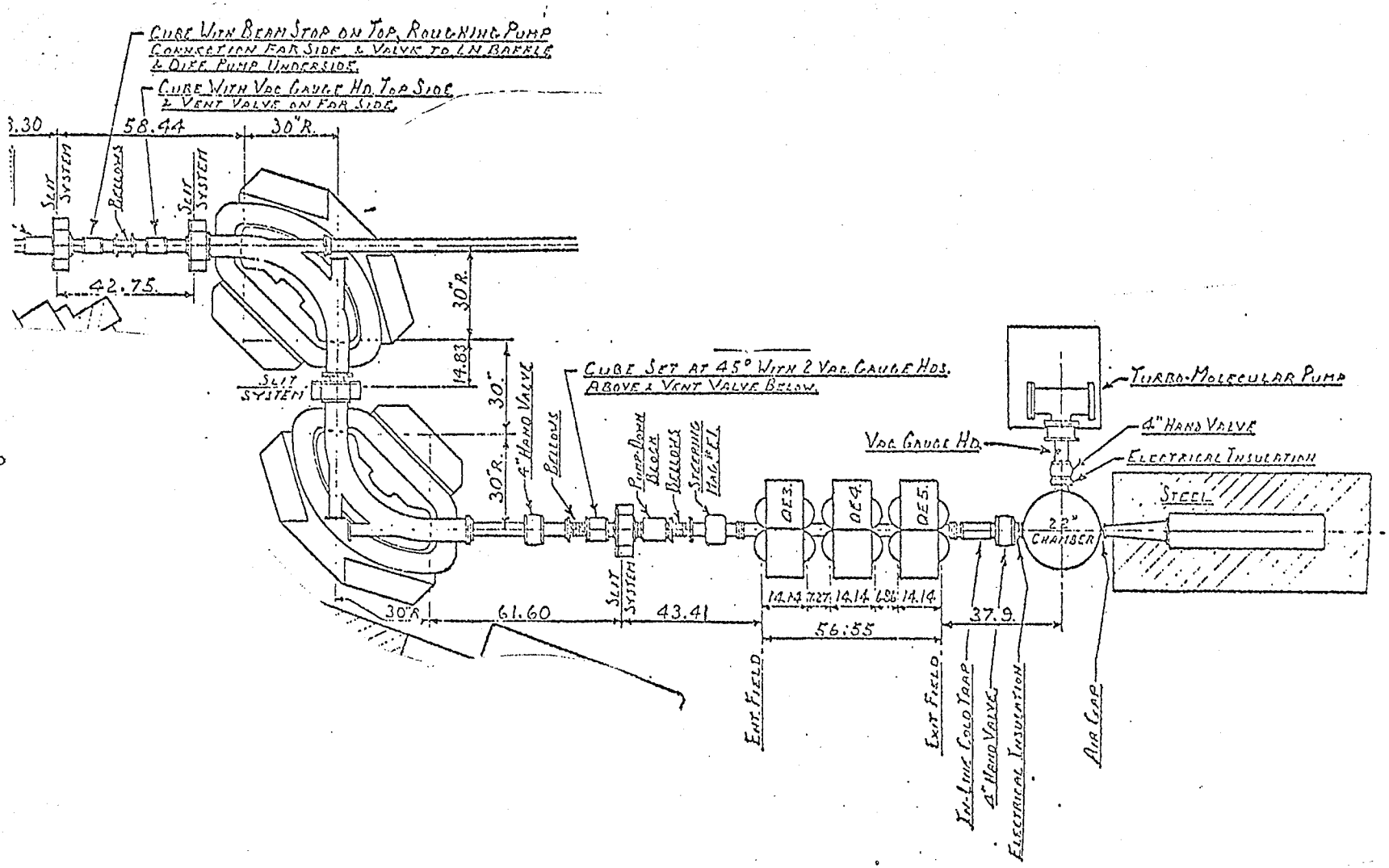

Fig (I.3) Momentum Analysis System Layout

The field non-reproducibility was found to be $\Delta B/B = \pm 5 \times 10^{-4}$. This was interpreted to be due to hysteresis. An investigation was made on the effect of this non-reproducibility on the quality of the image at the focal position, but it was found that it has a negligible effect.

The ratio between the average fields on the central orbits in both magnets was also measured . It was found that this ratio varies from 1.004 to 1.006 as the excitation varies from 9.5 KG to 12.5 KG. This required a proper adjustment of the trim coil current in order to maintain the same value of the field in both magnets.

The most intersting result of this mapping was that the field actually is not uniform(n=0) but it is slightly non-uniform. If we express the field in the form :

$$B(R) = B(R_0)\left[1 - n\left(\frac{R-R_0}{R_0}\right) + \beta\left(\frac{R-R_0}{R_0}\right)^2 + \gamma\left(\frac{R-R_0}{R_0}\right)^3 + \cdots\right]$$

where

$B(R_0)$ is the nominal field on the central ray (radius=R_0)

$B(R)$ is the field on the ray with bending radius = R

n, β, γ are the field indices.

It was found that the value of the field indices for both magnets are not the same. these values were :

1. For the first magnet : (the upsteam one)

   $n = -9.379 \times 10^{-3}$

   $\beta = -5.21 \times 10^{-2}$

   $\gamma = -.7253$

2. For the second magnet : (the downstream one)

$n = 2.7323 \times 10^{-3}$

$\beta = 1.05 \times 10^{-3}$

$\gamma = .2963$

This non-uniformity was found to have a negligible effect on both the quality and the position of the image.

1.4 Fringing Field Mapping

The actual bending radius increases steadily in the fringing field, so the real and the effective edge paths are separated by a small displacement which can be neglected in first order theory[3]. But for second-order calculations, this should be taken into consideration.

So, a mapping of the fringing field should be done carefully for both magnets. It was found that both magnets have similar fringing fields for both entrance and exit. Fig(1.4) shows the mapped median plane fringing field for the entrance of the first magnet (the upstream one) at an excitation of 11.5KG. The value of the tail was found to vary with the excitation from 1/4%B_o at excitation 9.5 KG to 1/2%B_o at excitation 13.5 KG, where B_o is the average field on the central orbit inside the magnet. This tail value implied the change of the object and the image distances from the ideal theoretical values to those appearing in Fig(1.3) in order to get an optimized image.

A theoretical fit for the measured fringing field was done, and it was found that the following Fermi function

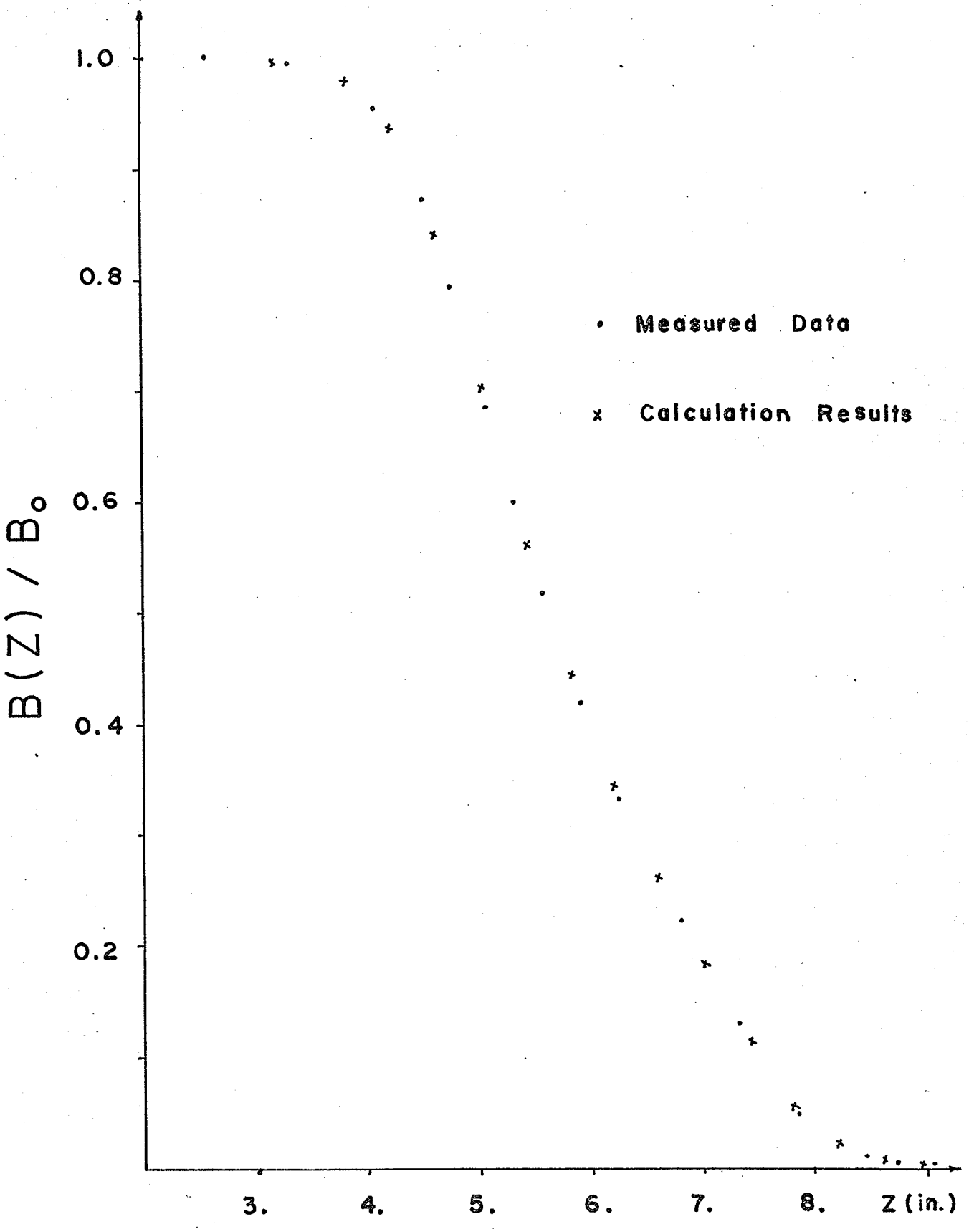
1.0
0.8
0.6
0.4
0.2
B(Z) / B₀
• Measured Data
x Calculation Results
3.
4.
5.
6.
7.
8.
Z (in.)

Fig (1·4)

gave an appropriate fit :

$$B(Z) = B_o \Big/ 1 + e^{c_o + c_1 S + c_2 S^2 + \cdots + c_5 S^5} \qquad (1.1)$$

where

B(Z) = The value of the field at distance Z measured from the pole root of the magnet.

B = Field on the central ray inside the magnet.

$S = Z - Z_{EFB} / G$

G = Air gap.

$c_o, c_1, c_2, c_3, c_4, c_5$ are constants.

The values of the constants $c_o, c_1, c_2, c_3, c_4, c_5$ which gave the best fit for both magnets were calculated to be as follows :

$c_o = 0.135$

$c_1 = 2.0857$

$c_2 = -0.508$

$c_3 = 0.7223$

$c_4 = 0.0252$

$c_5 = -0.0128$

Fig (1.4) shows the fringing field shape as calculated using the above values.

1.5 Computer Programs

Several computer programs were used to study the magnetic analysis system and the beam behaviour through the system. So, it may be helpful to discuss these computer codes before we proceed any further.

1.5.1 Program TRANSPORT[4]

This is a first- and second-order matrix multiplication ccmputer program. At any specified position in the system an arbitrary charged particle is represented by a vector (single column matrix) as follows :

$$X = \begin{bmatrix} x \\ x' \\ y \\ y' \\ l \\ d \end{bmatrix} \qquad (1.2)$$

where

x = The horizontal displacement of the arbitrary ray with respect to the assumed central trajectory.

x' = The angle this ray makes in the horizontal plane with respect to the assumed central trajectory.

y = The vertical displacement of the ray with respect to the assumed central trajectory.

y' = The vertical angle of the ray with respect to the assumed central trajectory.

l = The path length difference between the ray and the central trajectory.

d = The fractional momentum deviation of the ray from the assumed central trajectory.

Any element in the beam line is represented to the first-order by a square matrix R which describes the

action of this element on the particles coordinates. Thus the passage of a charged particle through the system may be represented by :

$$X(1) = R\ X(0)$$

where

$X(1)$ = The final coordinates of the particle under consideration.

$X(0)$ = The initial coordinates of the same particle.

If the particle has to traverse n elements so the matrix R will be the product of the individual matrices of the system elements :

$$R = R(n).R(n-1). \ldots .R(1)$$

The program calculates this cumulative transfer matrix and prints it out where desired.

Furthermore, the program calculates the second-order transfer matrix by adding another term to the above formalism. The components of the final vector in terms of the original , are now given by :

$$X_i\ (1) = \sum_j R_{ij}\ X_j\ (0) + \sum_{jk} T_{ijk}\ X_j\ (0)\ X_k\ (0) \qquad (1.3)$$

where R_{ij} and T_{ijk} are the elements of the first- and second-order transfer matrices, respectively. The suffixes i,j,k runs from 1 to 6 where x_1, x_2, x_3, x_4, x_5 ,and x_6 stands for x, x', y, y', l , and d respectively. The construction of the first- and secod-order transformation matrices is gives in appedix I.

Provision is made in this program to vary some

physical parameters of the elements comprising the system and to impose various constraints on the beam design. For example, varying the field strength values in a quadrupole triplet in order to get a waist at certain position.

1.5.2 Program RAYTRACE[5]

This Fortran program integrates the Lorentz equations of motion for a charged particle moving through an arbitrary magnetic field. Analytic expressions for the field (fringing or central) in the median plane is used as determined from the experimental data and/or mathematical models. A Taylor's expansion is used to determine the components of the field off the median plane (up to second-order terms). Using the expressions for the field the program is capable of tracing rays with arbitrary initial conditions through the system.

Besides, the program has the option of calculating the second-order transfer matrix and investigating higher order effects (third-order).

1.5.3 Program OPTIK[6]

This computer code calculates first-order transfer matrix based on the same theory discussed above in TRANSPORT. Moreover, the program investigates the second-order chromatic aberration effect.

1.6 Beam Behaviour

Rays were traced through the analysis system to study beam behaviour in both vertical and horizontal planes. The final coordinates of each ray at different points along the system were calculated using the computer code OPTIK described in section 1.5.3 .

1.6.1 The vertical behaviour

Fig(1.5) shows the behaviour of 42 Mev proton trajectories in the vertical plane (YZ). Starting with a vertically converging beam at slits S shown in Fig(1.1), a vertical waist can be formed between the quadrupole Q4 and the switching magnet. The initial values of the beam coordinates at the slits S were choosen such that they reflecl t the actual emittance measured there. Quadrupole doublet QE1,QE2 forms a large vertical waist half way between magnets. In this way the vertical beam envelope is approximately parallel and passes through the analyzing magnets gaps.

1.6.2 The horizontal behaviour

The horizontal behaviour of the beam (XZ-plane) through the system is shown in Fig(1.6). The quadrupole doublet QE1,QE2 shown in Fig(1.1) produces a horizontal waist of width 1mm and a negligible dispersion at the object slits. This will serve as an object for the first analyzing magnet, which forms a dispersed image half way between the two magnets. The second magnet will form a

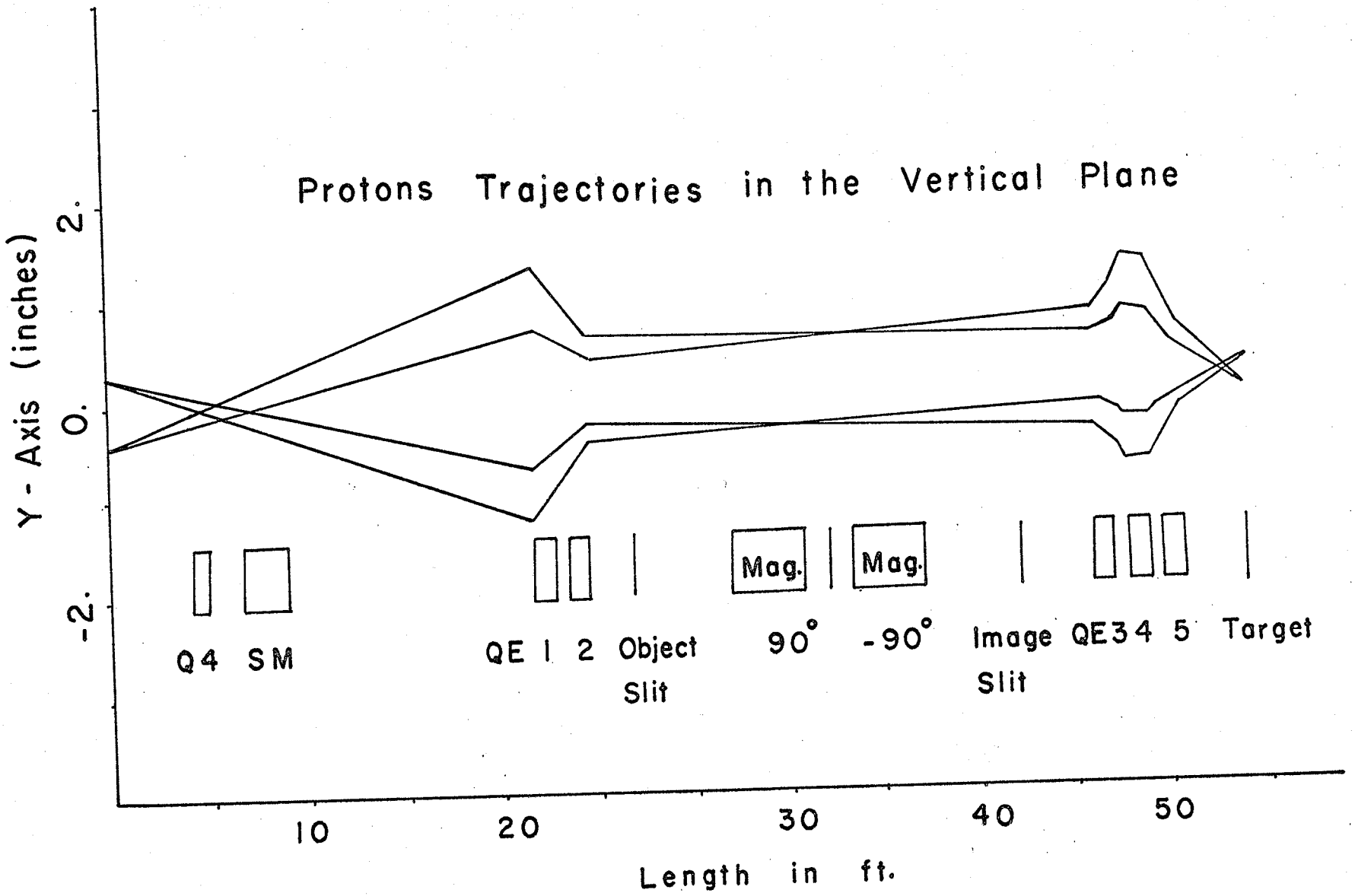
Protons Trajectories in the Vertical Plane
Y - Axis (inches)
2.
0.
-2.
Q4
SM
QE 1 2
Object Slit
Mag.
Mag.
90°
-90°
Image Slit
QE3 4 5
Target
10
20
30
40
50
Length in ft.

Fig (1.5)

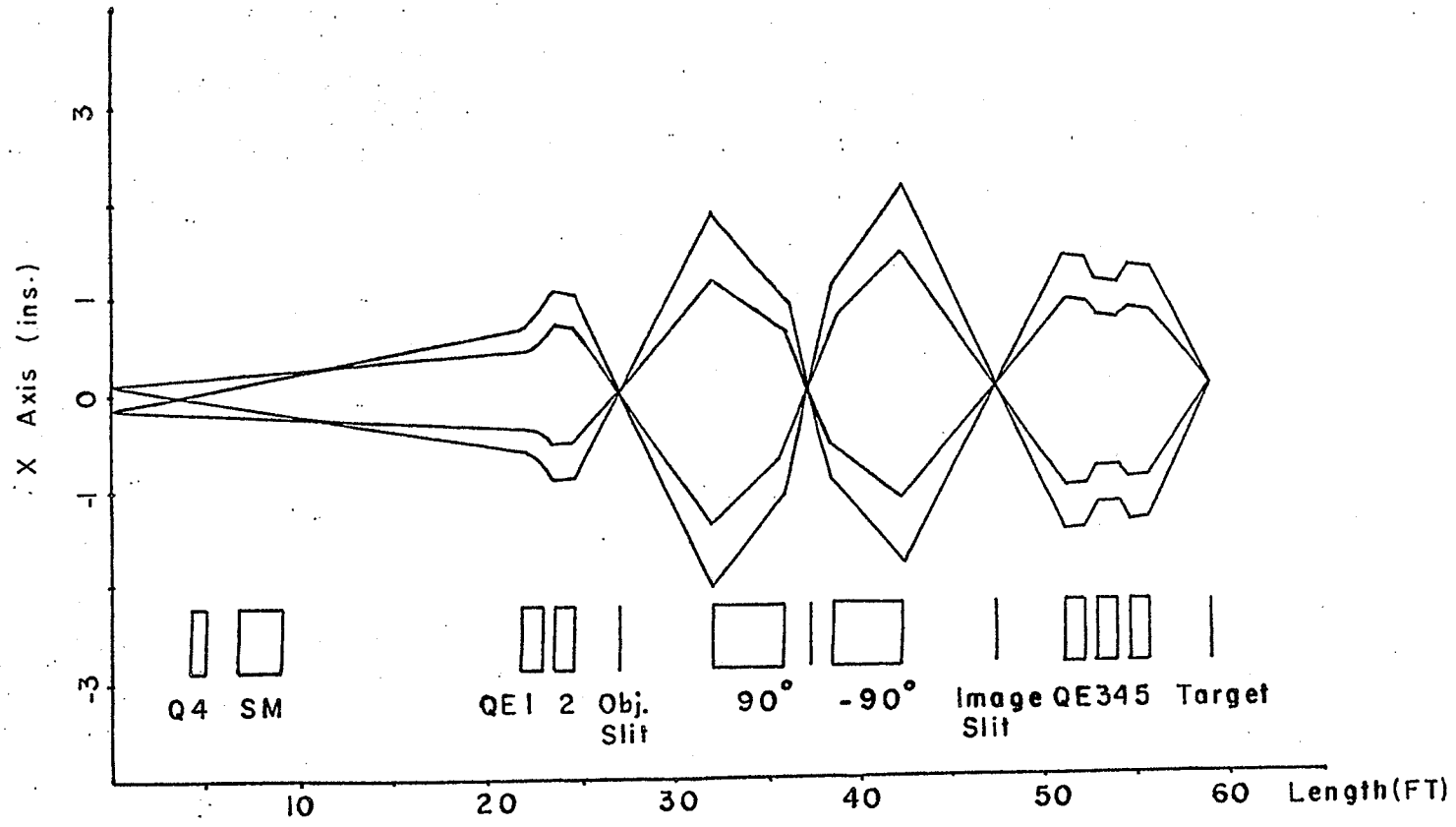

Fig (I.6) Protons Trjectories in the Horizontal Plane

more dispersed image at the image slits. The quadrupole triplet QE3-5 will form a horizontal waist on target.

Now, it is clear from Fig(1.6) that the beam divergence at the entrance of the first magnet is large (the max. divergence $x' = 30$ mrad), so the term that depends on x'^2 in the transport equation (eq.1.3) will be large enough to form geometric aberration at the image slits. To minimize the effect of this aberration, the analyzing magnets have been designed with curved entrance and exit edges with radius of curvature = 30 in.[3] . This has been verified to be effective by tracing rays through the system using the program code RAYTRACE and simulating the horizontal phase space ellipse at the image slits. The resulting phase space ellipse is shown in Fig(1.7). (meaning and properties of the phase space ellipse will be given in chapter 2).

The following data were used in this tracing :

Object distance = 149.403 cm

Image distance = 156.5 cm

Magnetic field index = those values given in sec(1.3)

The phase space ellipse at the image slits shown in Fig(1.7) can be considered as an an upright ellipse. This approximation is useful as will be shown in chapter 3.

1.7 Energy-Field Calibration

The average magnetic field (B) on the central orbit in

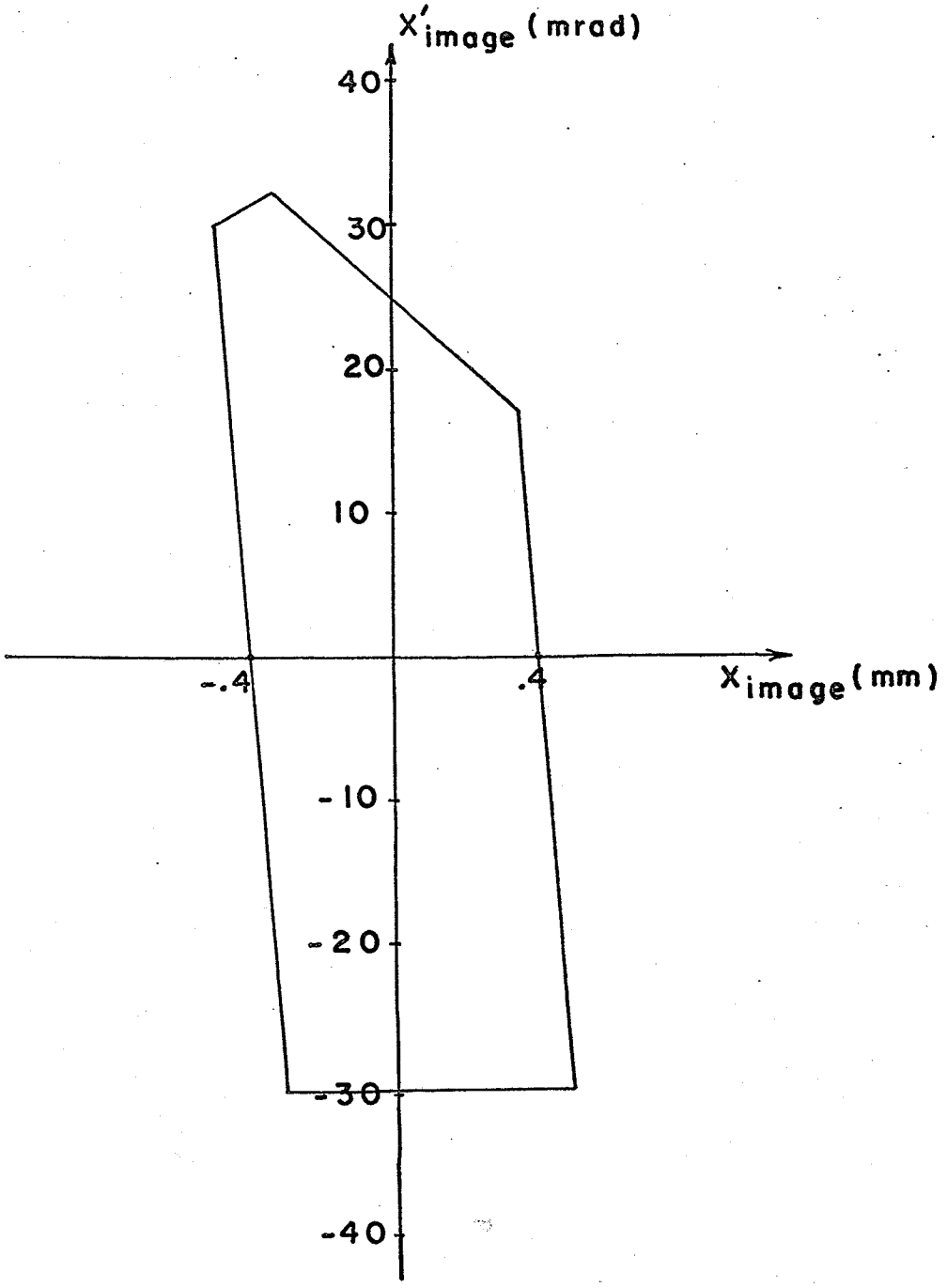

Fig (1·7)

Phase Space Ellipse at the Image Slits

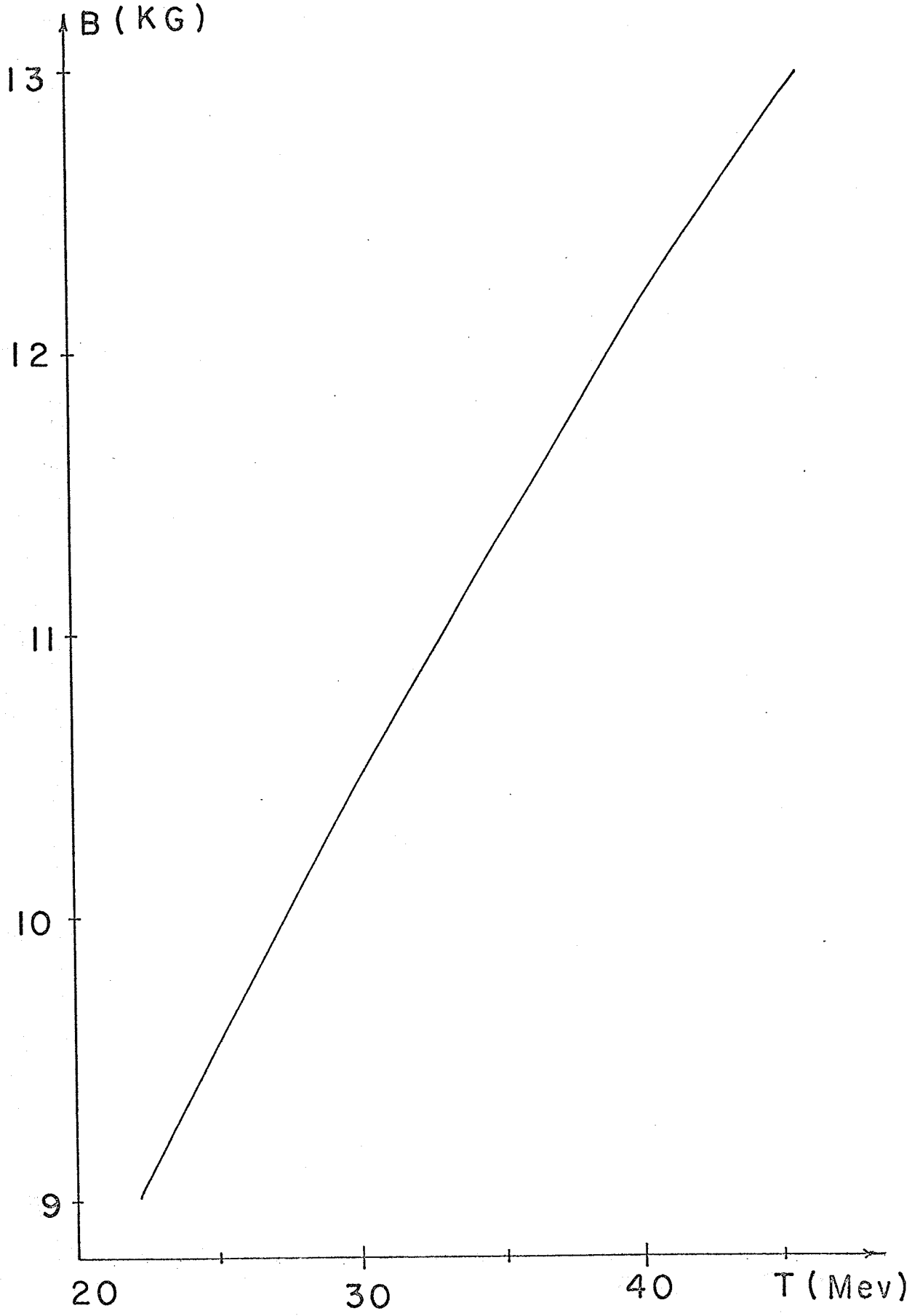

Fig (1·8)

both analyzing magnets is determined for a given proton kinetic energy (T_p) and bending radius of 30 in. from the relation :

$$B(KG) = \left\{ T_p(Mev) \left[T_p(Mev) + 1876.5 \right]^{\frac{1}{2}} \right\} \div 22.6 \qquad (1.4)$$

Fig(1.8) shows a plot of T vs. B as calculated from eq.(1.4). Also shown in Fig(1.9) a plot of the trim coils current vs. B together with a plot of B vs. the coarse dial setting . These two Figs. are used to excite the analyzing magnets properly for any specified proton energy T .

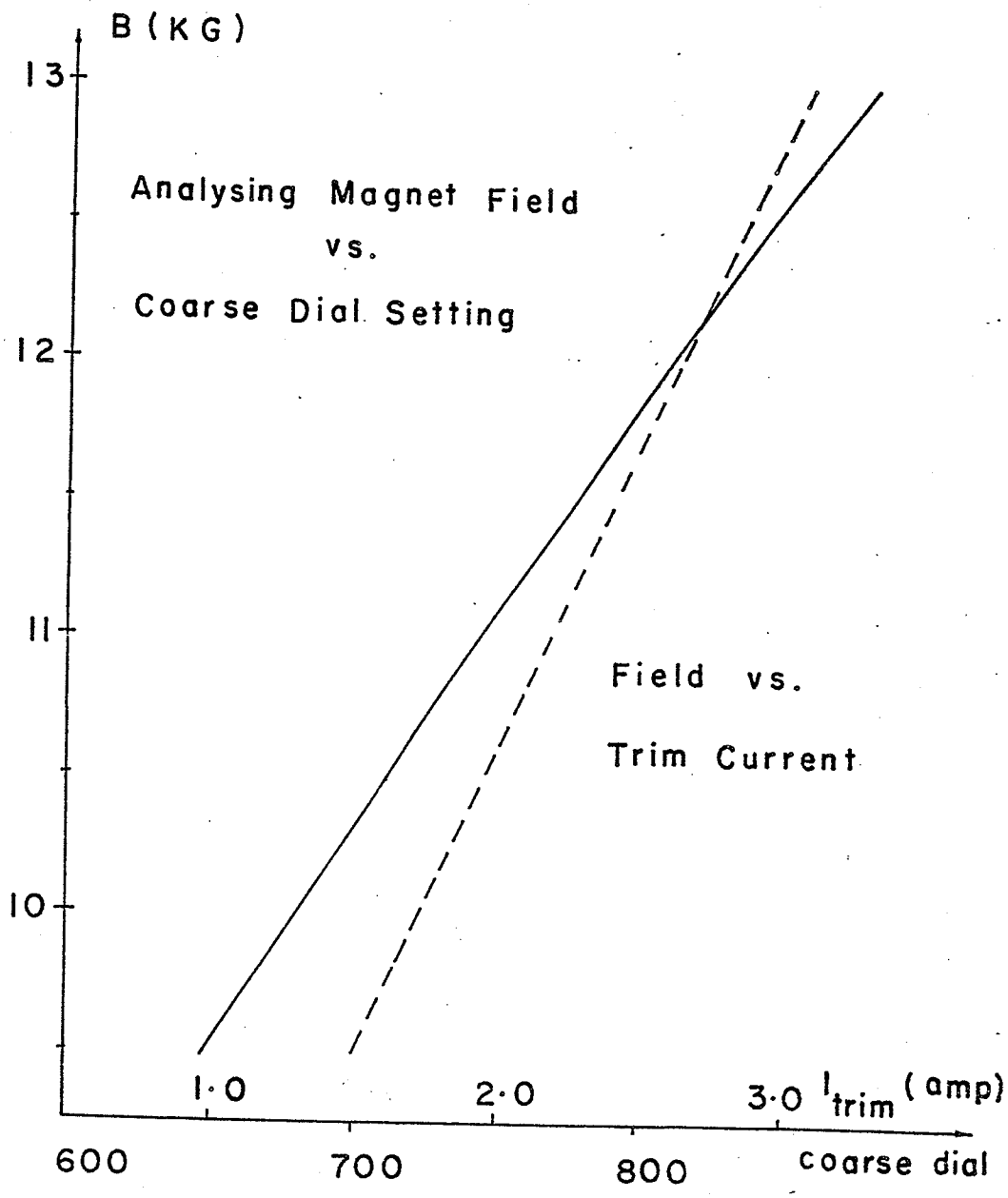
B (KG)
13
12
11
10
Analysing Magnet Field
vs.
Coarse Dial Setting
Field vs.
Trim Current
1·0
2·0
3·0 I_{trim} (amp)
600
700
800
coarse dial

Fig (1·9)

CHAPTER 2

THEORY

2.1 Description of the technique

In nuclear reaction experiments, the energy resolution is deteriorated by the kinematic effect . For the high resolution beam line, the 15 mm.mrad beam results in an angular divergence of $\pm 2^{\circ}$ on the target if the full acceptance of the beam is utulized. For lighter target nuclei , the resulting kinematic energy spread is large enough to nullify the advantages of the momentum analysis system discussed in chapter 1. For example, in the reaction $^{12}C(P,\alpha)^{9}B$ at 40 Mev and a scattering angle of 30° the kinematic energy spread is 109 kev/$^{\circ}$, increasing to 165 kev/$^{\circ}$ at 70°. For heavier target nuclei, the kinematic energy spread is less but the angular divergence is still unacceptably large for measurement of an angular distribution. This situation can be remarkably improved by beam matching.

Fig (2.1) shows a scattering geometry for a projectile beam incident on a target, the detector is placed at a laboratory scattering angle θ .

It is clear that if the scattering angle to the detector is to have the same value θ for each incident projectile, a one -to- one correspondence between the position of the projectile on the target (x_t) and its slope (x'_t) is implied. So, equality of the scattering angles obviously eliminates the kinematic energy spread,

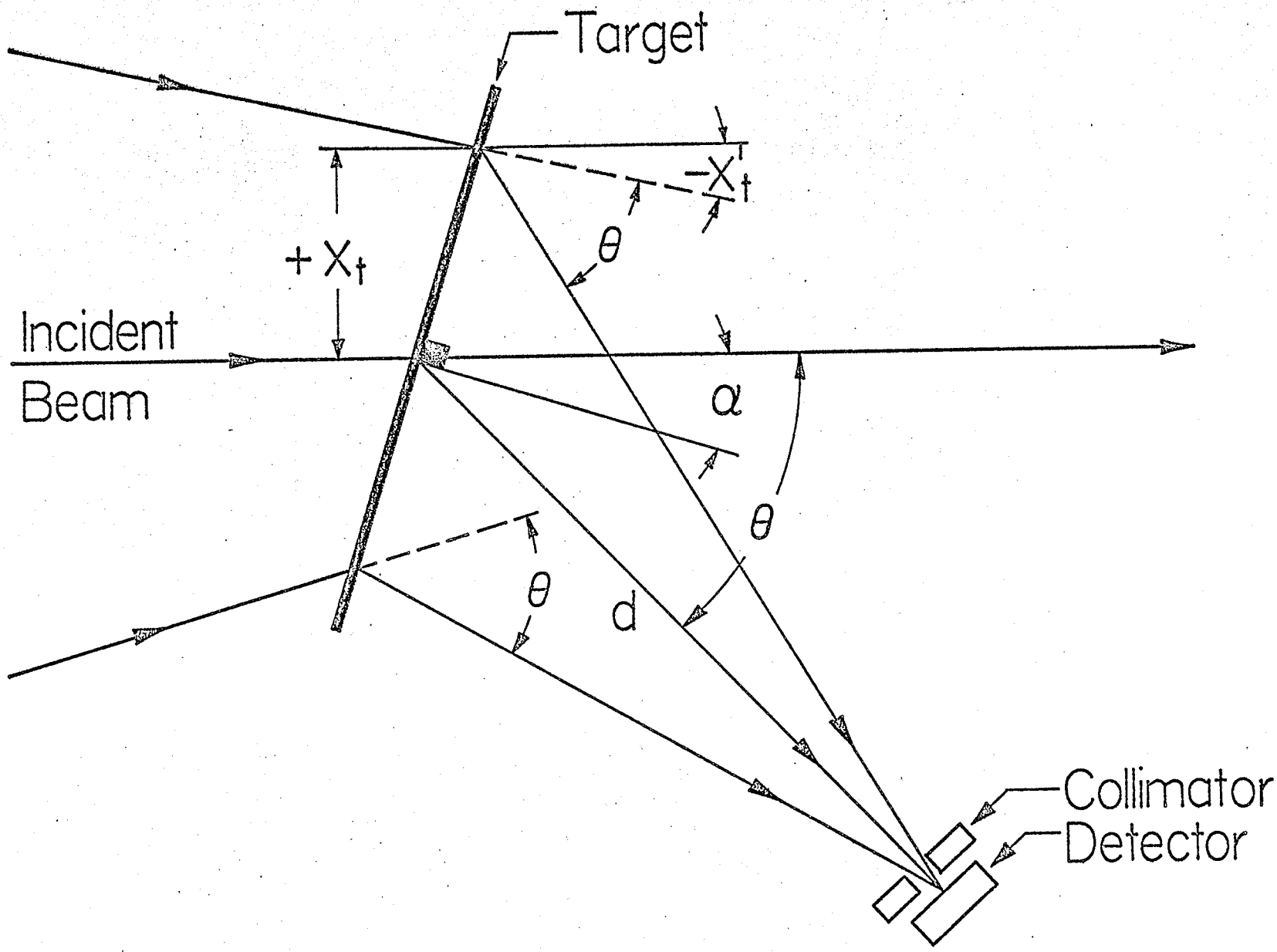
Target
$+X_t$
$-X_t$
θ
Incident
Beam
α
θ
θ
d
Collimator
Detector

Fig (2.1)

not only for elastic scattering but for any and all nuclear reactions as well. Simultaneously, the unique value of the scattering angle removes the problem of the angular resolution in determining the angular distribution.

2.2 Kinematic matching condition

The relation between the projectile position on the target (x_t) and its slope (x_t') necessary to achieve the one -to- one correspondence condition is derived below for both forward and backward scattering angles.

a. For forward scattering angles

Fig(2.2) shows a diagram of the target and detector which has been assumed to subtend a negligibly small horizontal angle and placed at scattering angle θ, distance d away from target. For all projectiles incident on target to have the same scattering angle θ we should have the focus beyond the target so that the beam on target will be converging.

From the geometry of the figure we can write :

$$\gamma + \theta - x_t' = 90 + \alpha$$

i.e.

$$\gamma = 90 + \alpha - \theta + x_t'$$

and

$$\beta = -x_t'$$

Also we can write :

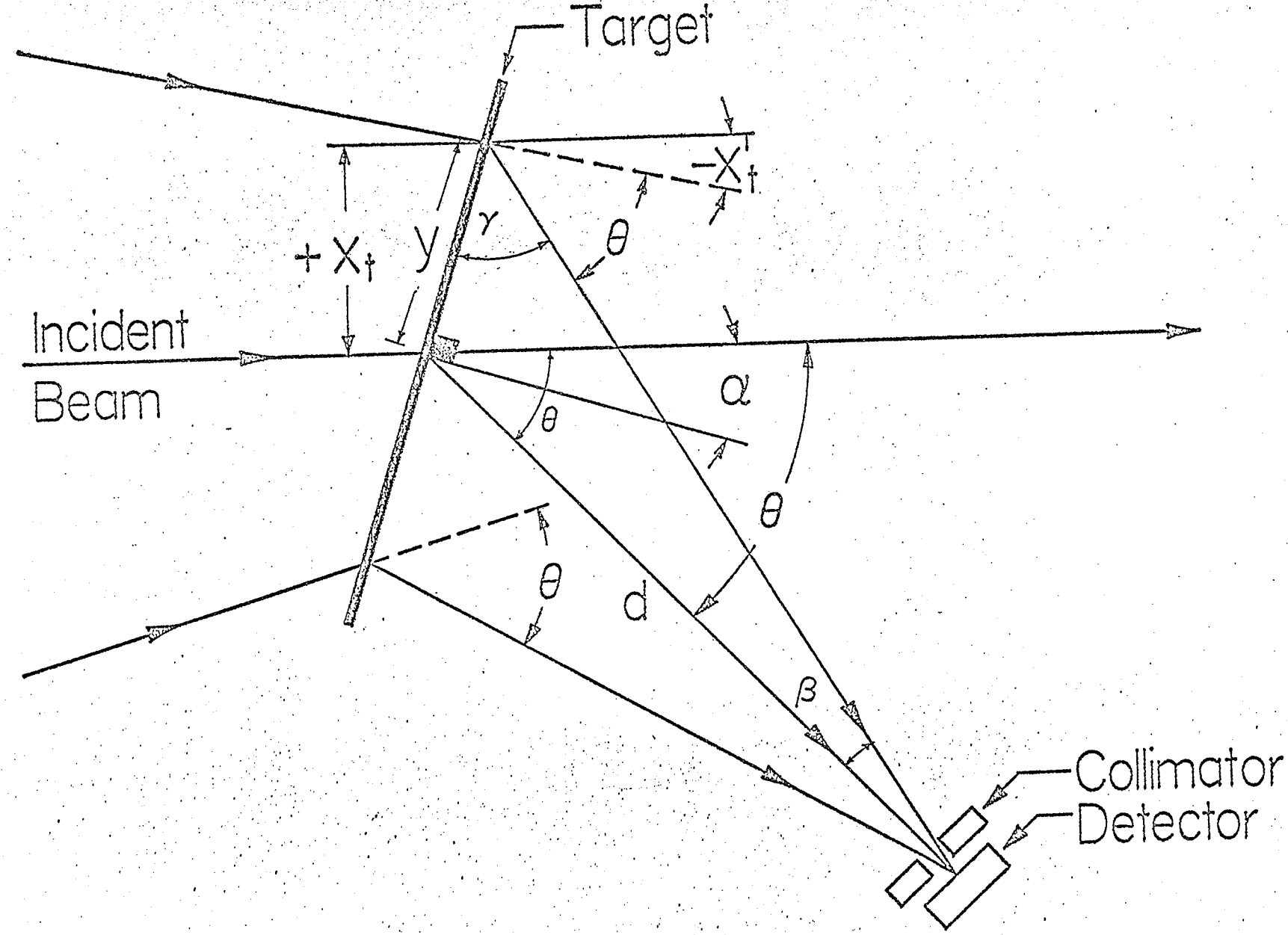
Target
$-X_t$
$+X_t$
y
γ
θ
Incident
Beam
θ
α
θ
θ
d
β
Collimator
Detector

Fig (2.2)

$$y = -d \sin x_t' / \sin\gamma \qquad (2.1)$$

$$x_t = y \cos\alpha \qquad (2.2)$$

$$\therefore x_t = \frac{-d\cos\alpha \sin x_t'}{\sin(90+\alpha-\theta-x_t')} = \frac{-d\cos\alpha \sin x_t'}{\cos(\alpha-\theta+x_t')} \qquad (2.3)$$

Since $x_t' \ll 1$ and $(\theta - \alpha)$ is generally selected by the experimenter to be less than $\pi/4$, we can write eq. (2.3) as :

$$x_t \cong \frac{-d\cos\alpha \cdot x_t'}{\cos(\theta-\alpha) - x_t' \sin(\theta-\alpha)}$$

$$\therefore \frac{x_t}{x_t'} \simeq \frac{-d\cos\alpha}{\cos(\theta-\alpha)} \qquad (2.4)$$

Eq. (2.4) gives the relation between x and x in order to achieve kinematic matching required.

b. For backward scattering angle

For scattering angles $> 90^\circ$ a waist in front of the target is required so that we can have the same scattering angle for all the projectiles on target. This geometry is shown in Fig (2.3). By following the same steps as in the case of forward scattering angles, we can easily get :

$$\frac{x_t}{x_t'} = -\frac{d\cos\alpha}{\cos(\theta-\alpha-x_t')}$$

$$\frac{x_t}{x_t'} \simeq \frac{-d\cos\alpha}{\cos(\theta-\alpha)} \qquad (2.5)$$

which is the same as eq. (2.4).

Eq. (2.4) gives the kinematic matching condition for any scattering angle. Table (2.1) shows the values of $-x_t/dx_t'$ for different scattering angles and target angles as calculated from eq. (2.4). Also shown in Fig (2.4) is a plot of $-x_t/dx_t'$ vs. θ for different values

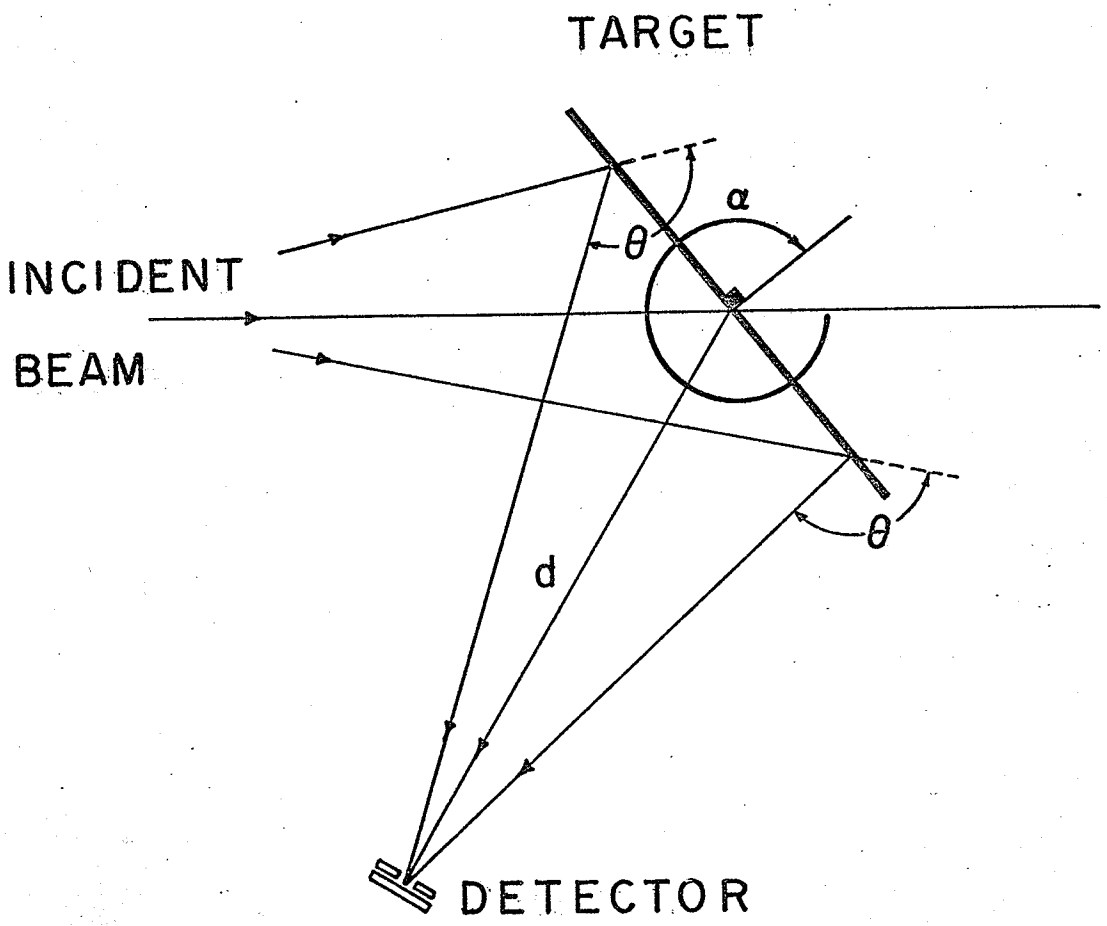

Fig (2.3)

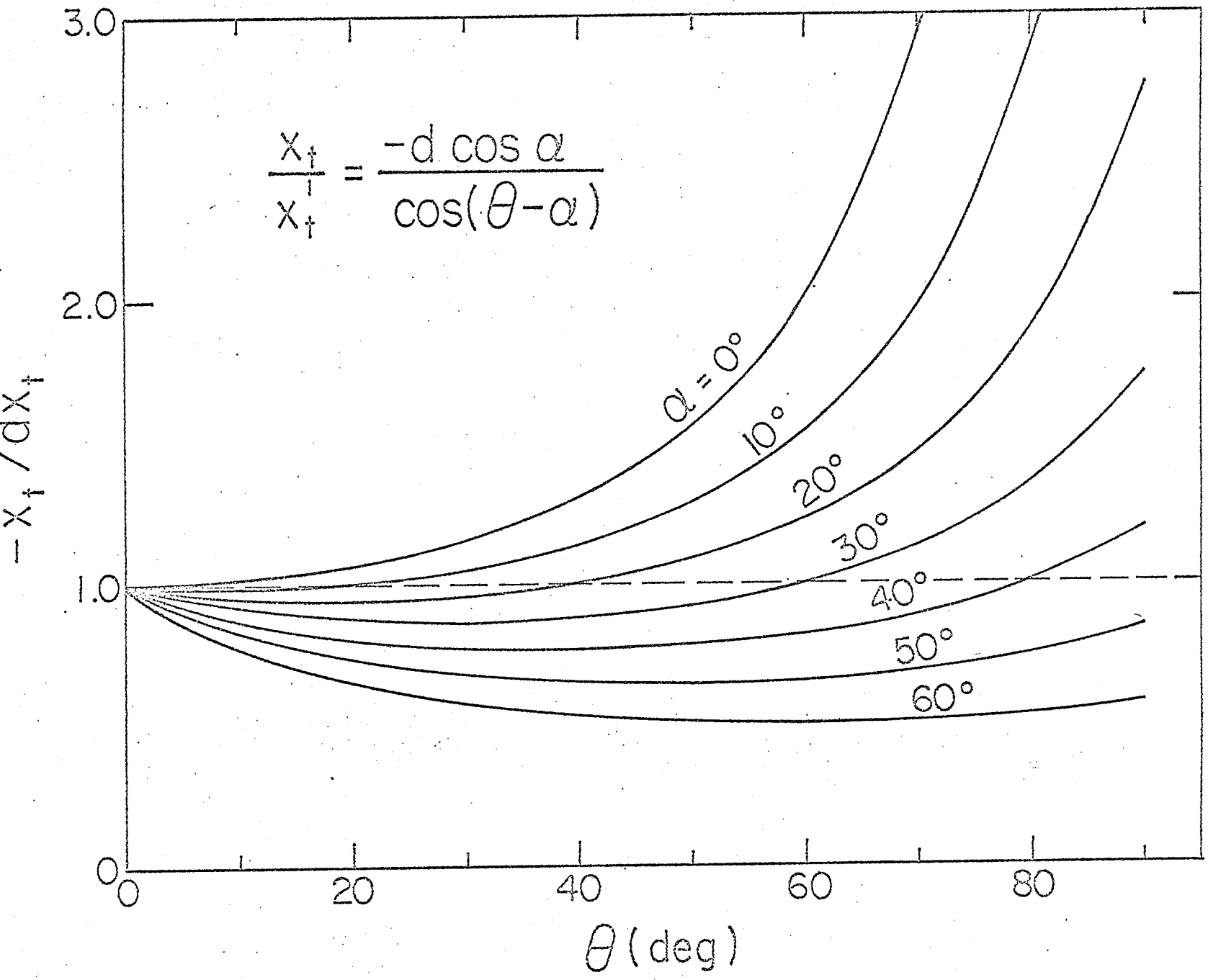
$\frac{X_t}{X_t'} = \frac{-d\cos\alpha}{\cos(\theta-\alpha)}$
$-X_t/dX_t'$
3.0
2.0
1.0
0
0
20
40
60
80
θ (deg)
$\alpha = 0°$
10°
20°
30°
40°
50°
60°

Fig (2.4)

Table (2.1)

Values of $-x_t/dx_t'$ for different scattering and target angles

Scattering angle	Target angle	$-x_t/dx_t'$
10	10	.985
15	15	.966
20	20	.94
25	20	.943
30	15	1.
35	15	1.028
40	20	1.
45	20	1.03
50	25	1.
55	25	1.047
60	30	1.
65	30	1.057
70	35	1.
75	35	.819
80	40	1.

of α . This table (or set of curves) are useful as we will see later.

Of course this unique correlation between x_t and x'_t for particles from an accelerator beam can not be achieved for all particles because of the nature of the phase space ellipse (see the following section). Nonetheless, it is possible to approximate the desired condition.

At this point it is helpful to introduce the following discussion to explain what is meant by the phase space ellipse, and to note some of its properties.

2.3 Phase space ellipse[3]

Particles from accelerator excute radial oscillations in the horizontal (scattering) plane about the central path. These excursions can be represented by :

$$x = x_o \sin \omega t \qquad (2.6)$$

$$= x_o \sin \frac{2\pi v t}{\lambda}$$

$$= x_o \sin \frac{2\pi z}{\lambda} \qquad (2.7)$$

where x_o is the amplitude, ω is the radial angular velocity, z is the distance travelled at velocity v in time t, and λ is the wave legth of the oscillation.

The slope of the path given by eq.(2.7) is given by :

$$x' = \frac{dx}{dz} = x_o \frac{2\pi}{\lambda} \cos \frac{2\pi z}{\lambda}$$

$$= x'_o \cos \frac{2\pi z}{\lambda}$$

where

$$x'_o = x_o \cdot \frac{2\pi}{\lambda} \qquad (2.8)$$

From eq. (2.7) and (2.8) we can write :

$$\frac{x^2}{x_o^2} + \frac{x'^2}{x'^2_o} = 1 \qquad (2.9)$$

This equation represents an ellipse in the x-x' plane, called the phase space ellipse ,as shown in Fig(2.5). The intercept of this ellipse with the axes x and x' are the max. displacement (x_o) and the max. slope (x'_o), respectively. A single particle obeying eq. (2.9) is represented as a single point on the ellipse, and as time and distance advances, the point moves clockwise round the ellipse. Particles executing oscillations of the same amplitude but different phase are also represented by points moving on the same ellipse, while particles with smaller amplitudes will move on smaller ellipses. The distribution inside the ellipse is not uniform but can be assumed to have a Gaussian shape .

2.4 Behaviour of the phase space ellipse[8]

In this section we will discuss the behaviour of the ellipse in the drift space (field free) only, because the knowledge of this behaviour is important in this experiment .

As shown in Fig(2.6) the beam's envelope widens as it traverses a drift space, but the maximum slope remains fixed, in other words every point on the envelope will be displaced parallel to the x-axis while the projection of the ellipse on the x'-axis remains constant, as shown in Fig(2.7). This can be described as a shearing motion,

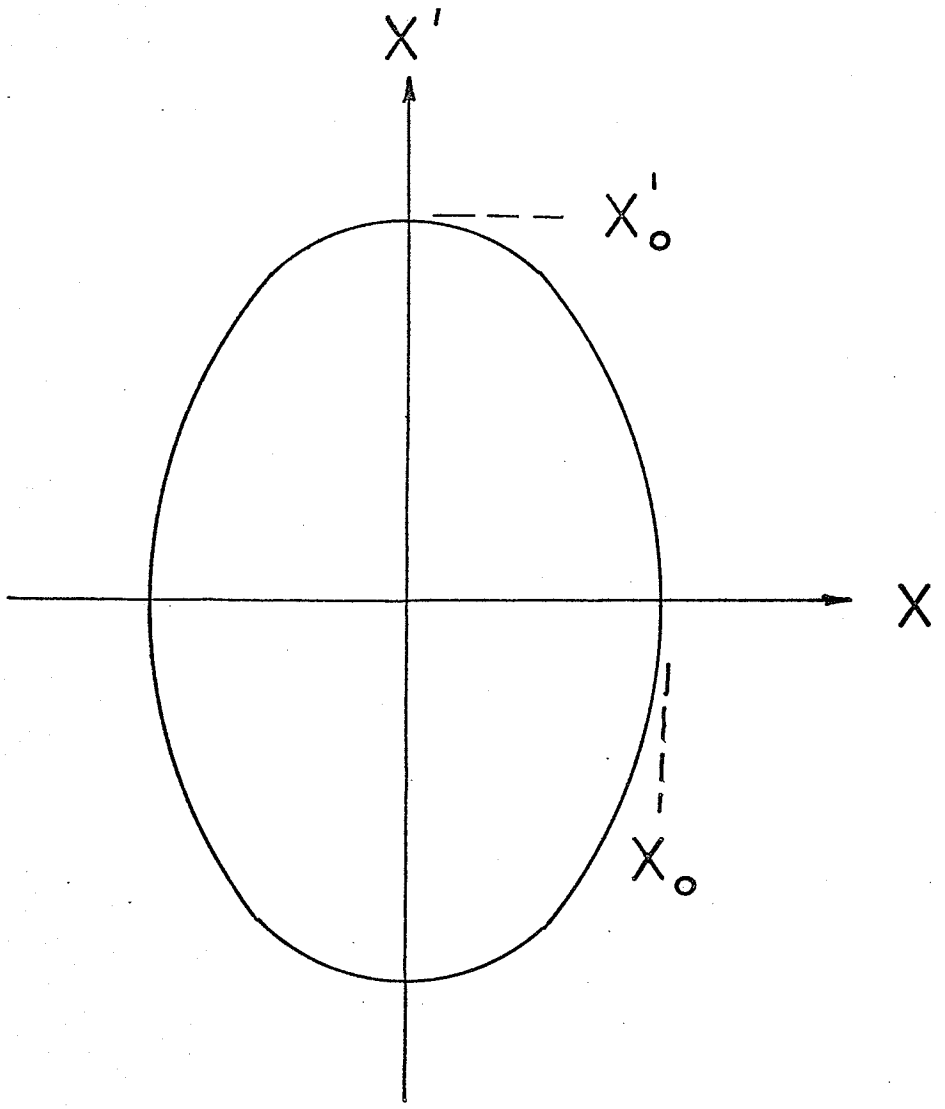

The Phase Space Ellipse

Fig (2.5)

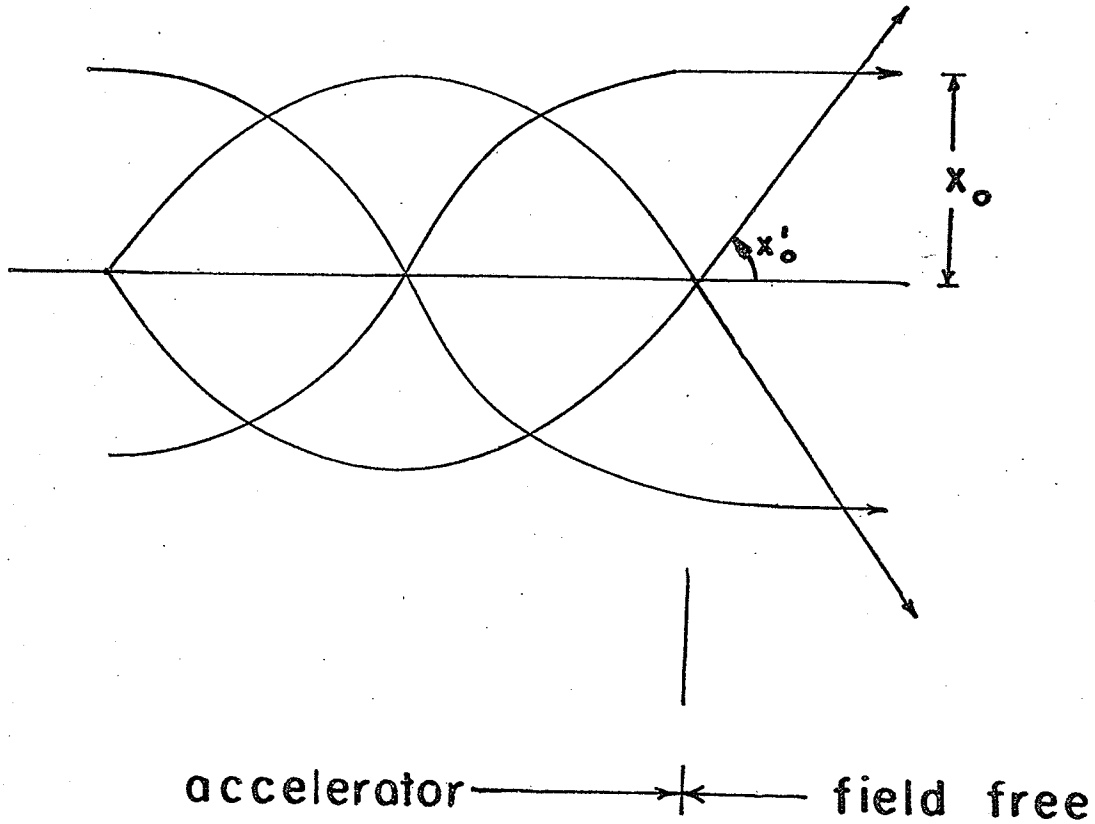

Fig (2.6)

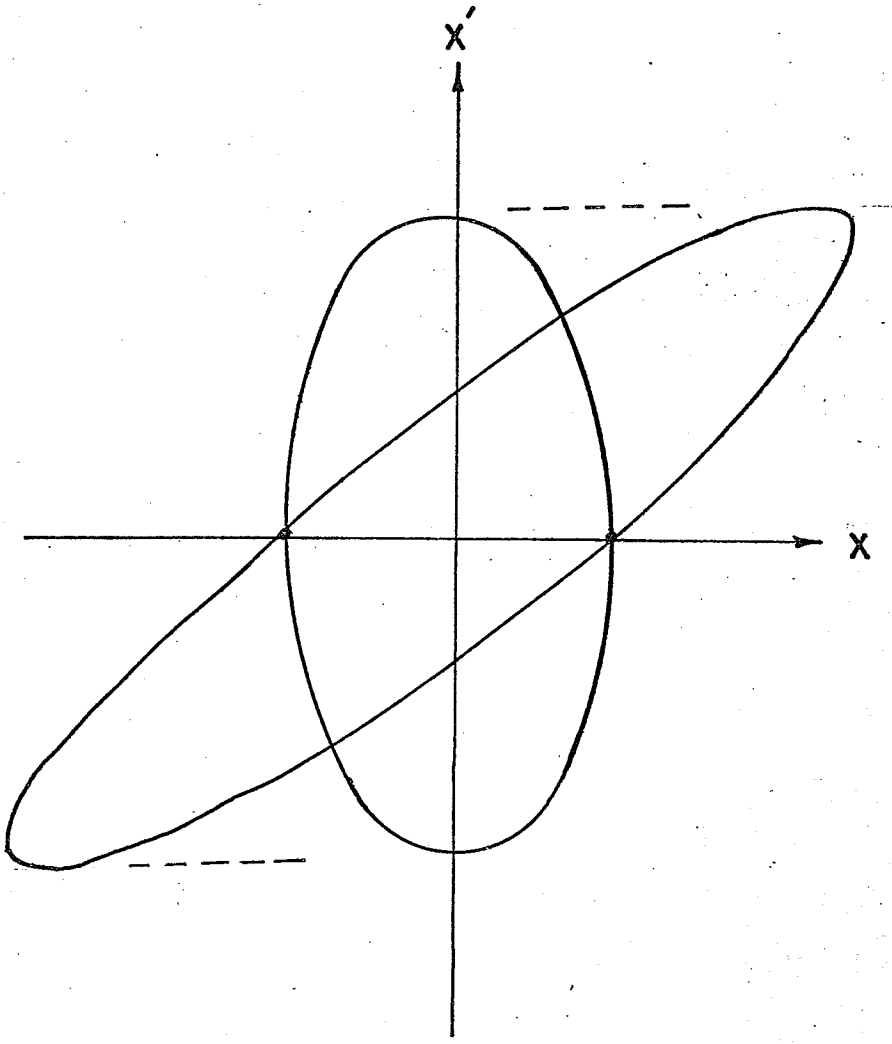

Fig (2.7) Effect of Field-free Region

the intersections with the x-axis acting as fixed pivots, while the area of the ellipse remaining constant by the virtue of Liouville's theorem[14]. So as a conclusion we can say that the drift space causes the ellipse to rotate in the clockwise direction, and undergo a shearing deformation as indicated in Fig(2.7) .

* * *

Now return to the kinematic matching condition. Typically the experimentalist selects the parameters of the beam optics so as to produce a horizontal waist (upright phase space ellipse) at the target position, as shown in Fig(2.8)b . At x=0 the beam has half-divergence of $x\omega'$. If this horizontal waist is moved to a point down stream, according to section 2.4, a rotated ellipse will be arranged on the target as shown in Fig(2.8)a. Clearly, the half-divergence at x=0 is reduced. This reduction depends on the distance to which the waist is moved, i.e the degree of rotation of the phase space ellipse. Moreover, particles lying on the axis A-A of the rotated ellipse of Fig(2.8)a can be arranged so that they satisfy the kinematic matching condition set forth in eq.(2.4). To the extent that particles along the axis A-A are representative of all particles in the beam, the kinematic matching condition is fulfilled. The modus operandi suggested by the foregoing is the following :

From the knowledge of the properties and location of the

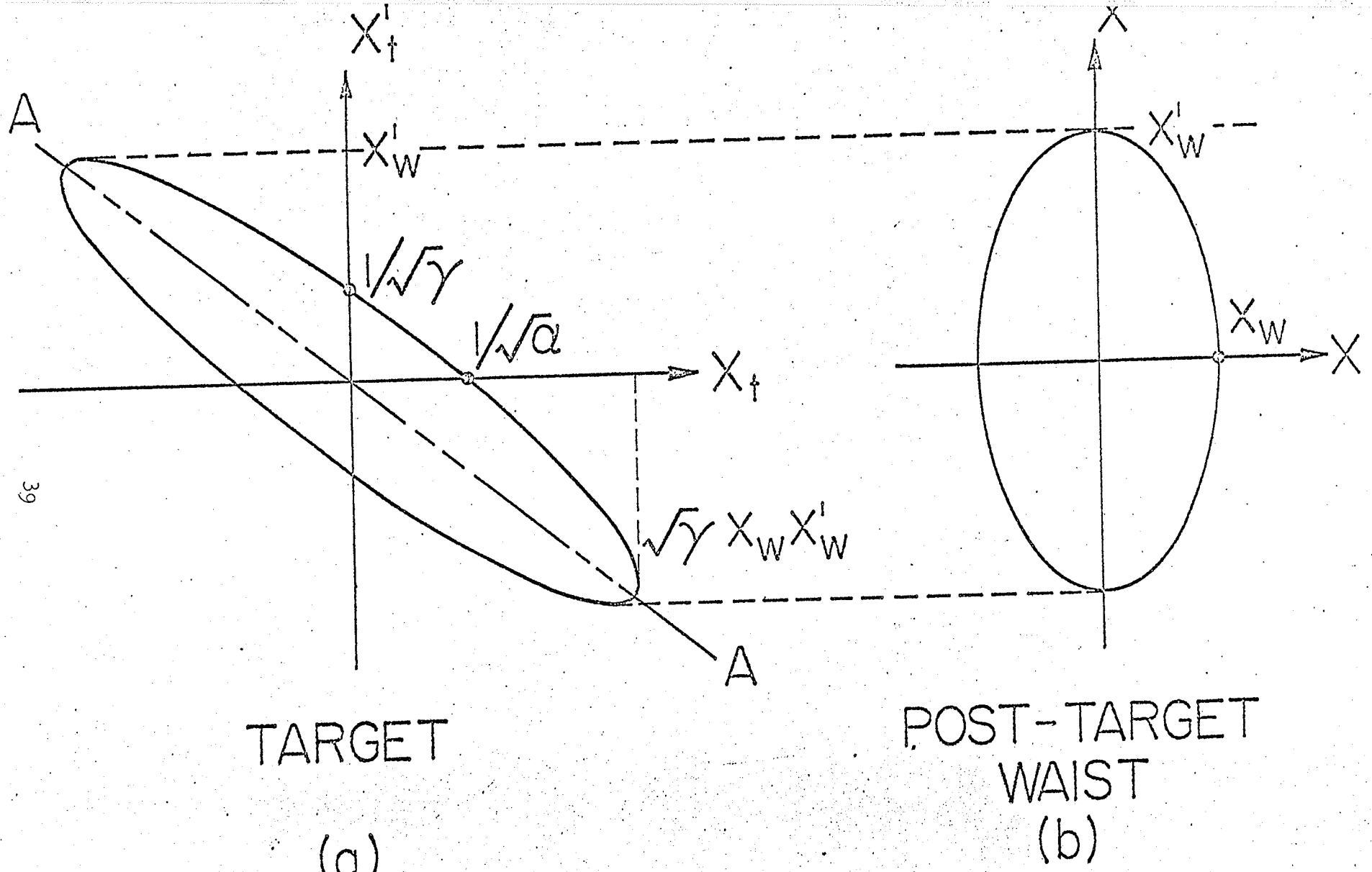

TARGET

(a)

POST-TARGET WAIST

(b)

Fig (2.8)

horizontal waist at a post-target location, the properties of the phase space ellipse on target can be determined. i.e another expression for x_t/x_t' can be obtained in terms of the properties of the post-target waist and its location. this relation will be derived in the following section.

In the case of the backward scattering, the above argument is still aplicable, except that the phase space ellipse on the target will be rotated in the clockwise direction since the waist is in front of the target.

2.5 Properties of the phase space ellipse on target

The upright ellipse (waist) at distance L beyond (or in front) the target, shown in Fig(2.8) can be expressed as :

$$\alpha_\omega x^2 + \gamma_\omega x'^2 = 1 \qquad (2.10)$$

where

$$\alpha_\omega = 1/x_\omega^2$$
$$\gamma_\omega = 1/x_\omega'^2$$

x_ω and x_ω' represent the horizontal half-width and half-divergence, respectively.

Any point (x_t, x_t') in the ellipse at the target position is related to a point (x, x') on the waist ellipse by the simple drift-space transport equation :

$$\begin{bmatrix} x \\ x' \end{bmatrix} = \begin{bmatrix} 1 & L \\ 0 & 1 \end{bmatrix} \begin{bmatrix} x_t \\ x_t' \end{bmatrix} \qquad (2.11)$$

where L is the distance between target and post-target waist. Substituting eq.(2.11) into eq.(2.10) we get :

$$\alpha_\omega x_t^2 + 2L\alpha_\omega x_t x_t' + (\alpha_\omega L^2 + \gamma_\omega) x_t'^2 = 1 \qquad (2.12)$$

Equation (2.12) represents the phase space ellipse on target. The cross-product term $2L\alpha_\omega x_t x_t'$ indicates that the ellipse is tilted anticlockwise (waist beyond target, L positive) or clockwise (waist in front of target, L negative).

Introducing the dimensionless quantities :

$$\left.\begin{aligned} \epsilon &= x_t / x_\omega \\ \zeta &= x_t' / x_\omega' \end{aligned}\right\} \qquad (2.13)$$

and writing eq. (2.12) in terms of these two quantities, we get :

The orientation of this target phase space ellipse is best described by choosing a new coordinate system (u, v). In Fig (2.9) let u and v be the two axes along the major and minor axes of the ellipse, respectively. Assuming that the ellipse is rotated by an angle θ, we can write :

$$\left.\begin{aligned} \epsilon &= v\cos\theta - u\sin\theta \\ \zeta &= v\sin\theta + u\cos\theta \end{aligned}\right\} \qquad (2.15)$$

squaring both eq. (2.15)

$$\left.\begin{aligned} \therefore \epsilon^2 &= v^2\cos^2\theta - 2uv\sin\theta\cos\theta + u^2\sin^2\theta \\ \zeta^2 &= v^2\sin^2\theta + 2uv\sin\theta\cos\theta + u^2\cos^2\theta \end{aligned}\right\} \qquad (2.16)$$

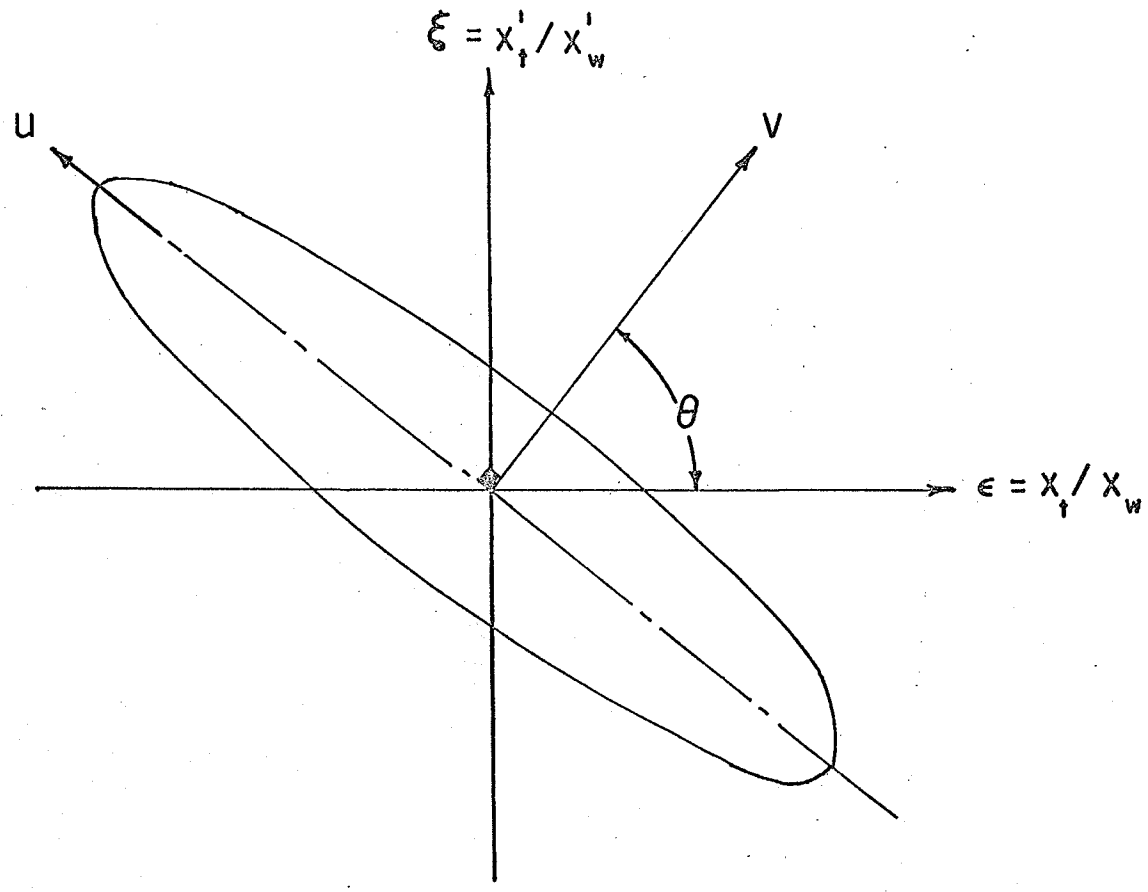

Fig (2.9)

Substituting (2.16) into (2.14), we get :

$$v^2 \cos^2\theta - 2uv \sin\theta \cos\theta + u^2 \sin^2\theta +$$

$$2L \frac{x'_\omega}{x_\omega} \left(v^2 \sin^2\theta \cos\theta - u^2 \sin\theta \cos\theta + uv \cos^2\theta - uv \sin^2\theta \right) +$$

$$\left(\frac{\alpha_\omega}{\gamma_\omega} L^2 + 1 \right) \left[v^2 \sin^2\theta + u^2 \cos^2\theta + 2uv \sin\theta \cos\theta \right] = 1 \qquad (2.17)$$

For eq. (2.17) to represent an ellipse with u and v the major and minor axes, the coefficient of uv term should vanish, i.e.

$$-2L \frac{x'_\omega}{x_\omega} \left(\sin^2\theta - \cos^2\theta \right) - 2 \sin\theta \cos\theta + 2 \sin\theta \cos\theta \left(\frac{\alpha_\omega L^2}{\gamma_\omega} + 1 \right) = 0$$

Using the double-angle relations, the last equation can be written as :

$$2L \frac{x'_\omega}{x_\omega} \cos 2\theta - \sin 2\theta + \left(\frac{\alpha_\omega}{\gamma_\omega} L^2 + 1 \right) \sin 2\theta = 0$$

$$\therefore \tan 2\theta = -2L \frac{x'_\omega}{x_\omega} \Big/ \frac{\alpha_\omega}{\gamma_\omega} L^2$$

$$\text{i.e.} \quad \frac{2\tan\theta}{1 - \tan^2\theta} = \frac{-2 x_\omega}{x'_\omega L} = -2X / L \qquad (2.18)$$

X = characteristic length of the beam

(This characteristic legth is just a quantity to characterize the beam waist)

L = distance (in mm) between target and waist position.

Particles along axis (A-A) in Fig(2.9) are characterized by :

$$\frac{\epsilon}{\xi} = -\tan\theta \qquad (2.19)$$

using eq.(2.13) we can write :

$$\frac{\epsilon}{\xi} = \frac{x_t \cdot x_\omega}{x_t' \cdot x_\omega'} = \frac{x_t}{x_t' X} \qquad (2.20)$$

Substituting eq.(2.20) into eq.(2.19) , we get :

$$\tan \theta = \frac{-x_t}{x_t' X} \qquad (2.21)$$

Substituting eq.(2.21) into eq.(2.18) :

$$\frac{-2x_t/x_t' X}{1-(x_t/x_t' X)^2} = \frac{-2X}{L} \qquad (2.22)$$

THe solution of this equation is :

Fig(2.10) shows a plot of x_t/x_t' vs. L for different values of X , according to eq.(2.20).

Equations (2.4) and (2.23) are used together in kinematic matching as follows :

For a particular experiment with scattering angle (θ) and target angle (α) we use eq.(2.4) (or Fig(2.4)) to calculate the quantity $-x_t/dx_t'$. Knowing the target-detector distance (d) and the beam characteristic length X we use eq.(2.23) or Fig(2.10) to determine the distance L . If we move the waist to this distance L the kinematic matching is fulfilled.

It should be kept in mind that this distance L is calculated assuming that all the particles in the phase space ellipse on target are represented by particles along the major axis AA shown in Fig(2.8)a .

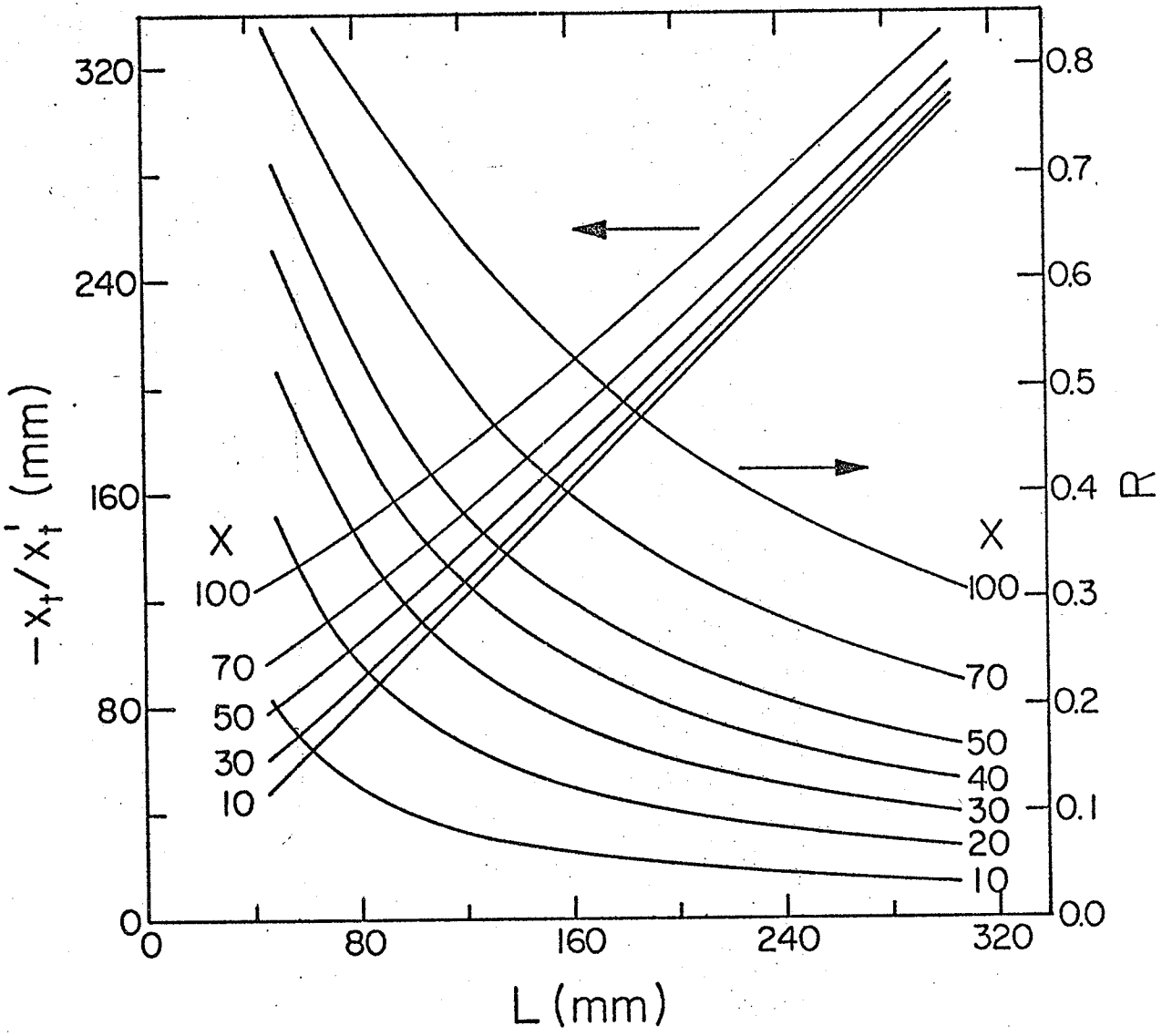
320
240
160
80
0
0
80
160
240
320
L (mm)
$-x_t/x_t'$ (mm)
R
0.8
0.7
0.6
0.5
0.4
0.3
0.2
0.1
0.0
X
100
70
50
30
10
X
100
70
50
40
30
20
10

Fig (2.10)

2.6 Divergence reduction ratio

The reduction in the beam maximum divergence on target accompanied by moving the waist to a point downstream (or upstream) is expressed through the "figure of merit" R where $R = \left.\frac{x'_t}{x'_\omega}\right|_{x_t=0}$

To get a mathematical expression for R, we set $x_t = 0$ in eq. (2.12). this will give :

$$R = 1 \Big/ \sqrt{\frac{x'^2_\omega L^2}{x^2_\omega} + 1}$$

$$\therefore \quad R = \left[1 + \frac{L^2}{X^2}\right]^{-1/2} \qquad (2.24)$$

Fig (2.10) shows a plot of R vs. L for different values of X . From this set of curves we can calculate the expected reduction in the beam maximum divergence for each distance L and hence, we can get a rough estimation for the energy resolution improvement factor .

2.7 Detector shape

The energy resolution improvement expected from theory above is obviously of little value for a detector of infinitesimal solid angle, as in the case of using a very narrow collimator in front of the detector. So, a position sensitive surface barrier detector is an obvious choice for this application , where we use the position information to apply kinematic corrections (this will be discussed in details in section 3.6).

Because these detectors are relatively long (typically

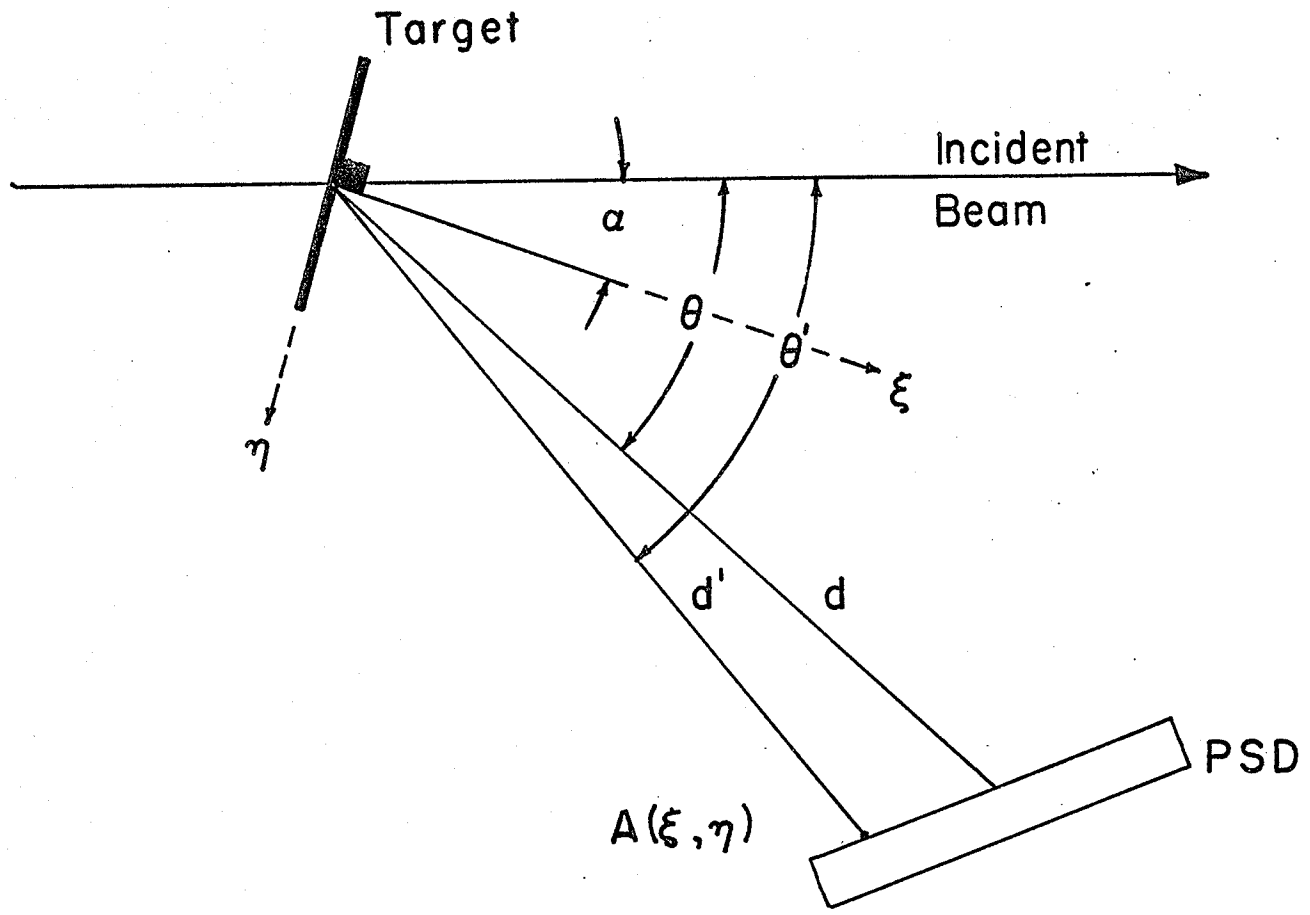

Fig (2.11)

25 mm) , it is important to satisfy the kinematic matching condition specified by eq.(2.4) for all the points along the length of the detector. Fig(2.11) shows a scattering geometry with the centre of the position sensitive detector placed at a scattering angle θ and distance d away from the target. Taking two coordinate axes ξ , η to be along the target and the normal direction, respectively, any point A(ξ,η) on the detector surface with scattering angle θ' and distance d' away from the target satisfies the following relations :

$$\frac{\xi}{d'} = \cos(\theta' - \alpha) \qquad (2.25)$$

and

$$\frac{\eta}{d'} = \sin(\theta' - \alpha) = \sqrt{1 - \cos^2(\theta' - \alpha)} \qquad (2.26)$$

But in section (2.2) we showed that particles along the major axis of the phase space ellipse on target should satisfy the following matching condition :

$$-\frac{x_t}{x_t'} = \frac{d\cos\alpha}{\cos(\theta - \alpha)} = \frac{d'\cos\alpha}{\cos(\theta' - \alpha)} \qquad (2.4)$$

but along the major axis of the ellipse we have :

$$-\frac{x_t}{x_t'} = \text{constant } C \qquad (2.27)$$

eq.(2.4) can be written as :

$$d' = \frac{-x_t\cos(\theta' - \alpha)}{x_t'\cos\alpha} = \frac{C\cos(\theta' - \alpha)}{\cos\alpha} \qquad (2.28)$$

substituting (2.28) into (2.25) , we get :

$$d' = (\xi C/\cos\alpha)^{1/2} \qquad (2.29)$$

using eq.(2.28) and (2.29) , eq.(2.26) can be written as :

$$\eta / \sqrt{\frac{\xi C}{\cos\alpha}} = \sqrt{1 - \frac{d'^2\cos^2\alpha}{C^2}} = \sqrt{1 - \frac{\xi\cos\alpha}{C}} \qquad (2.30)$$

by squaring eq.(2.30)

$$\therefore \quad \eta^2 = \frac{\xi c}{\cos\alpha}\left(1 - \frac{\xi\cos\alpha}{c}\right)$$

$$= \frac{\xi c}{\cos\alpha} - \xi^2$$

$$\therefore \quad \eta^2 + \left(\xi - \frac{c}{2\cos\alpha}\right)^2 = \frac{c^2}{4\cos^2\alpha} \qquad (2.31)$$

The locus of points defined by eq.(2.31) is a circle shown in Fig(2.12) with radius

$$\frac{c}{2\cos\alpha} = \frac{(d/2)}{\cos(\theta-\alpha)}$$

and its centre lies along the ξ-axis at a distance

$$\frac{c}{2\cos\alpha} = \frac{d/2}{\cos(\theta-\alpha)}$$

from the target position. This means that the detector surface should be a portion of a circle in order that the kinematic matching condition can be fulfilled for each point on the position sensitive detector.

Of course, it is practically difficult to obtain such a detector. But as an approximation we place the detector along the tangent of the circle defined by eq.(2.31), as shown in Fig(2.12). Placing the detector along the tangent means we place it at an angle (β), where the value of β can be determined at once from Fig(2.12) to be :

$$\beta = \theta - \alpha$$

where

θ = scattering angle

α = target angle

2.8 Theoretical calculations

To test the energy resolution improvement discussed above, a Monte Carlo calculations were made using the computer program KCORR described below :

2.8.1 The computer program KCORR

This Fortran program has the provision to trace a large number of rays from the object slits, through the analyzing magnets, see Fig(1.1), and to the waist position in the scattering chamber. All rays in the beam at the object slits had been assumed to have a maximum energy bite of $\frac{\Delta E}{E} = \pm 2.2 \times 10^{-4}$. Energy deviation for each ray from the assumed central trajectory energy was choosen at random from that interval. The maximum displacement (x_o) and the maximum divergence (x'_o) in the horizontal (scattering) plane were given as input and the program chooses the coordinates of each ray (x, x') at random using a random number generator. The particle distribution within the phase space ellipse is not uniform but it was assumed to have approximately a Gaussian shape. This Gaussian distribution is characterized by a quantity 'β' (simply β is proportional to the reciprocal of the variance of the Gaussian distribution). By increasing the value of β the Gaussian shape becomes narrow and vice versa. Events whose coordinates (x, x') were chosen at random should satisfy this Gaussian shape condition otherwise they are rejected.

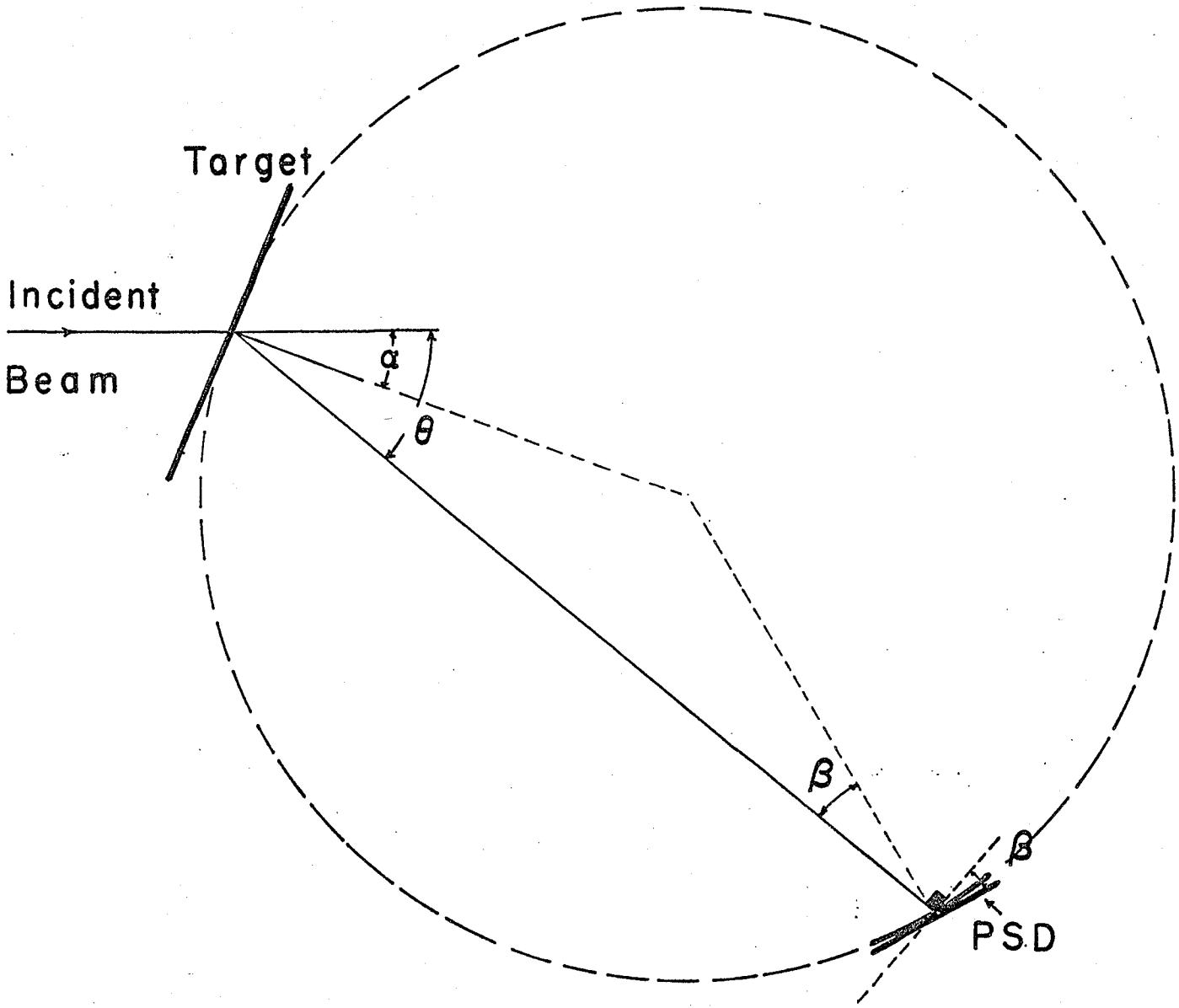

Fig (2.12)

In regard to the choice of the coordinates of the rays in the vertical plane, it was shown in Fig(1.5) that the beam in the vertical plane is almost parallel, therefore the vertical divergence of the rays (y′) was taken to be zero while the vertical displacements (y) of rays were chosen such that they clear the analyzing magnets gaps (Typical value is ± 1 cm).

After choosing the rays parameters at the object slits ($x, x', y, y', \Delta p$) , the program traces each ray individually through the two analyzing magnets and calculates the coordinates of each ray at the image slits, shown in Fig(1.1) using the second order transfer equation :

$$x_i(1) = \sum_j R_{ij}\, x_j(0) + \sum_{jk} T_{ijk}\, x_j(0)\, x_k(0) \qquad (1.3)$$

The coefficients R_{ij}, T_{ijk} were precalculated using the computer code RAYTRACE described in section 1.5, and they were given to KCORR as input data. The reason that the transfer matrix for the analyzing magnets was calculated using RAYTRACE code rather than the widely used TRANSPORT code is that RAYTRACE permits the use of the analytic expression of the fringing field while TRANSPORT assumes a standard fringing field function for all magnets .

After that the program traces the rays through the quadrupole triplet QE3, QE4, QE5 to the target and the waist position. The final coordinates of each ray at the target position (x_t, x_t') were calculated using the second order transfer equation with the coefficients R_{ij}, T_{ijk}

precalculated using the computer code TRANSPORT. The target coordinates (x_t, x_t') for each ray were used to calculate the exact scattering angle $(\theta_1 + x_t')$. The expression for θ_1 can be easily seen from Fig(2.13) to have the following form :

$$\theta_1 = \arctan \frac{d \sin\theta_o + x_t}{d \cos\theta_o - x_t \tan\alpha}$$

where

θ_o = scattering angle for the central ray with momentum P and divergence= 0

d = target-detector distance

α = target angle

x_t = final displacement of the projectile on the target.

Finally , the program calculates the energy of the outgoing particle (E3) of the reaction under investigation, and hence, calculates a histogram for the number of particles vs. (E3-E0) where E0 is the energy of the outgoing particle with scattering angle θ_o.

The FWHM of the resulting histogram is a measure for the energy resolution. So by running the program twice, once with the coefficients R_{ij} and T_{ijk} of the transfer equation (1.3) from the image slits to the target position corresponding to a waist at the target position, then run it once more using the coefficients R_{ij} and T_{ijk} corresponding to a waist distance L away from the target , the resulting energy distributions can be used to test

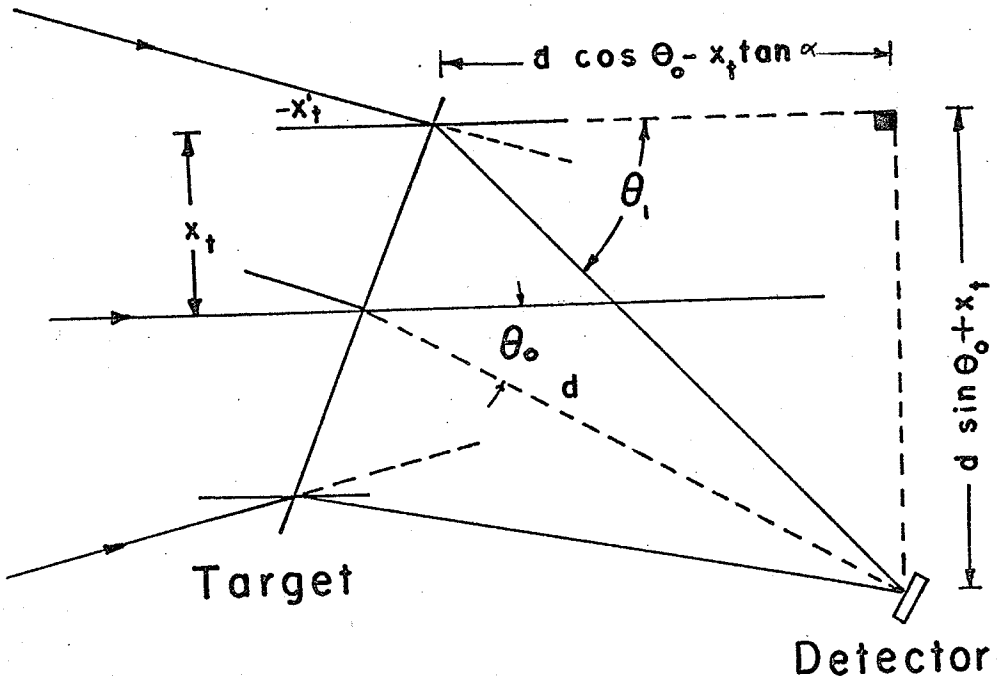

Fig (2.13)

the theory and determine the factor of improvement in energy resolution.

The uncertain factor in these calculations was the characteristic length X, since this was found to depend on the fine tuning of the cyclotron. A value was selected for each run which consistent with the constrains of the divergence limiting slits at the entrance to the first magnet.

One more difficulty was encountered in using this program, namely, assigning numerical values for the quantitiy β mentioned above. To overcome this difficulty we chose for each run a value for β which gave an energy distribution whose FWHM value was equal to that measured experimentally for the case L = 0 , then used the same value for the run with L≠0.

2.8.2 Calculation results

As a preliminary test for the theory , we considered the reaction $^{1}H(P,P)^{1}H$ with the following simulated data :

Incident proton energy	=42.5 Mev
Lab scattering angle	$=40^{\circ}$
Target angle	$=20^{\circ}$
Target detector distance	=180 mm
Beam characteristic length	=50 mm/rad
β	= 0.9

The distance L for the kinematic matching was calcu-

Table (2.2)

The coefficients of the transfer eq.

from object to image slits

First order

1.05857	0.00132	0.004	0.006	0.0	-4.6871
13.12818	0.9613	0.2932	0.03104	0.0	-29.914
o.o	o.o	1.42283	0.7147	0.0	0.0
o.o	0.0	1.41174	1.3334	o.o	0.0
o.o	0.0	0.0	0.0	1.0	0.0
0.0	0.0	0.0	0.0	0.0	1.0

Units are cm for coordinates and mrad for divergences

Second order

5.294D1

1.758D-1 1.337D-4

0.0 0.0 4.870D-2

0.0 0.0 -2.63D-2 5.006D-3

0.0 0.0 0.0 0.0 0.0

-1.56D-1 -1.23D-2 0.0 0.0 0.0 -2.34D2

6.564D2

4.939D1 9.61D-2

0.0 0.0 2.93D-1

0.0 0.0 -1.28D-1 2.58D-2

0.0 0.0 0.0 0.0 0.0

-2.59D-1 -4.43D-2 0.0 0.0 0.0 -1.49D3

Table (2.3)

Coefficients of the transfer eq.

from the image slits to target position

(case of L = 0)

First order

1.04952	0.0	0.0	0.0	0.0	-46.997
0.00131	0.95281	0.0	0.0	0.0	-0.0299
0.0	0.0	1.0	217.768	0.0	0.0
0.0	0.0	0.0	1.0	0.0	0.0
0.0	0.0	0.0	0.0	1.0	0.0
0.0	0.0	0.0	0.0	0.0	1.0

Units are mm for coordinates and rad for divergences

Second order

-8.17D-6					
-2.22D-2	-1.69D1				
0.0	0.0	8.084D-3			
0.0	0.0	4.95D1	8.89D4		
0.0	0.0	0.0	0.0	0.0	
-9.19D-2	-1.37D2	0.0	0.0	0.0	9.33D-1

-4.24D-9					
-1.28D-5	-1.102D-2				
0.0	0.0	5.15D-6			
0.0	0.0	2.83D-2	4.66D1		
0.0	0.0	0.0	0.0	0.0	
-5.23D-5	-8.81D-2	0.0	0.0	0.0	4.49D-4

Table (2.4)

Coefficients of the transfer eq. from image slits to target position (L=167mm)

First order

-.65628	221.938	0.0	0.0	0.0	0.0
-/0058	-1.3289	0.0	0.0	0.0	0.0
0.0	0.0	.8047	53.9303	0.0	0.0
0.0	0.0	0.0	0.0	1.0	0.0
0.0	0.0	0.0	0.0	0.0	1.0

Units are mm for coordinates and rad for divergences

Second order

0.0					
0.0	0.0				
0.0	0.0	0.0			
0.0	0.0	0.0	0.0		
0.0	0.0	0.0	0.0	0.0	
7.185D-3	2.88D1	0.0	0.0	0.0	0.0

0.0					
0.0	0.0				
0.0	0.0	0.0			
0.0	0.0	0.0	0.0		
0.0	0.0	0.0		0.0	
-7.765D-6	1.33D-1	0.0	0.0	0.0	0.0

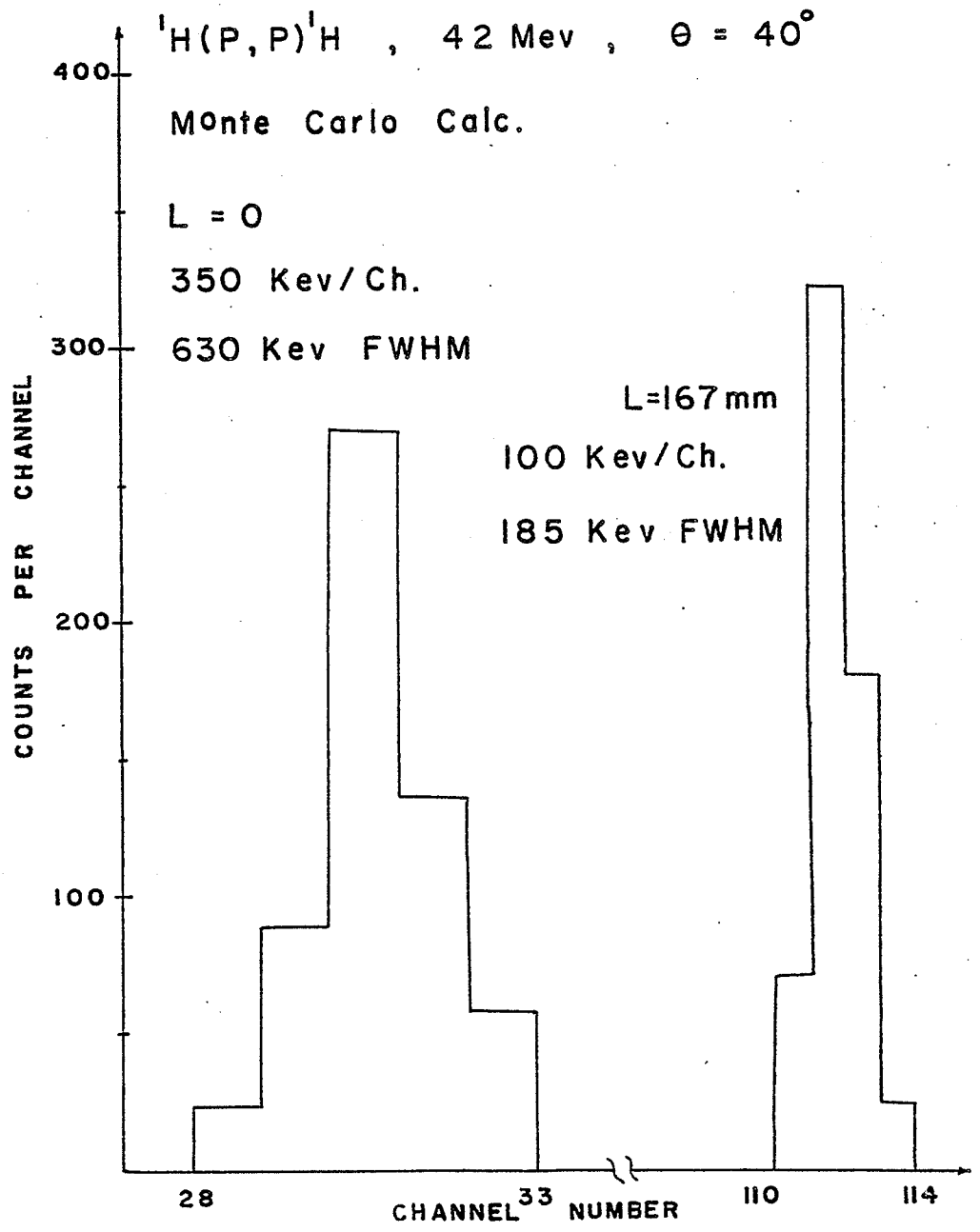
$^1H(P,P)^1H$, 42 Mev , $\theta = 40^\circ$
Monte Carlo Calc.
L = 0
350 Kev/Ch.
630 Kev FWHM
L=167mm
100 Kev/Ch.
185 Kev FWHM
COUNTS PER CHANNEL
400
300
200
100
28
33
110
114
CHANNEL NUMBER

Fig (2.14)

lated as follows :

From Fig(2.4) for $\theta = 40^{\circ}$, $\alpha = 20^{\circ}$ we can find that $-x_t/x'_t\, d = 1$ i.e. $-x_t/x'_t = 180$. Using Fig(2.10) we can get at once that L =167 mm. . The computer program KCORR was run twice. Once for the case L = 0, the coefficients of the transfer equation from the object slits to the image slits and from the image slits to the target position are shown in tables (2.2) and (2.3). The second run of the program was for the case L = 167 mm . The coefficients of the transfer eq. from the object slits to the image slits and from the image slits to the target position for this case are shown in tables (2.2) and (2.4), respectively.

Fig(2.14) shows the resulting energy distributions. For the case of L=0 the energy resolution is 630 Kev FWHM, while it is 185 Kev FWHM for the case of L=167 mm i.e. the energy resolution has been improved by a factor of 3.4 .

Before we tested the theory experimentally, we had to know if the distance L calculated as described is the optimum one. For this purpose similar runs for the same reaction were done for different values of L (greater and smaller than the calculated one).

Fig(2.15) and (2.16) show the energy distributions for L = 130 mm and L = 200 mm , respectively. The energy resolution for both cases is more than that for the case

of L = 167 mm . After similar runs with different distances we conculded that the distance L calculated as described above is the optimum one within ±1 cm .

$^{1}H(P,P)^{1}H$, 42 Mev , $\theta = 40^{\circ}$

Monte Carlo Calc.

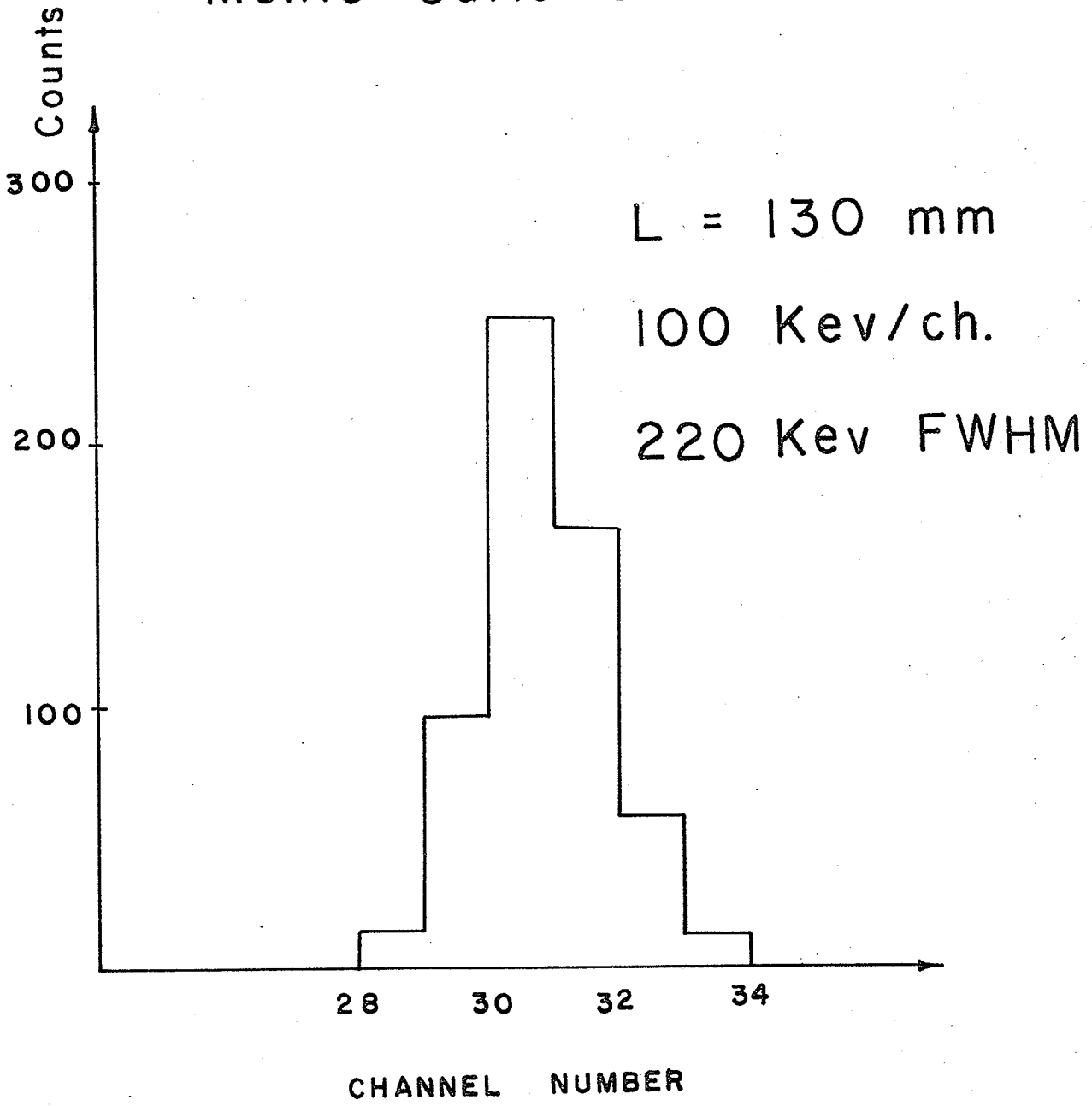

Fig (2.15)

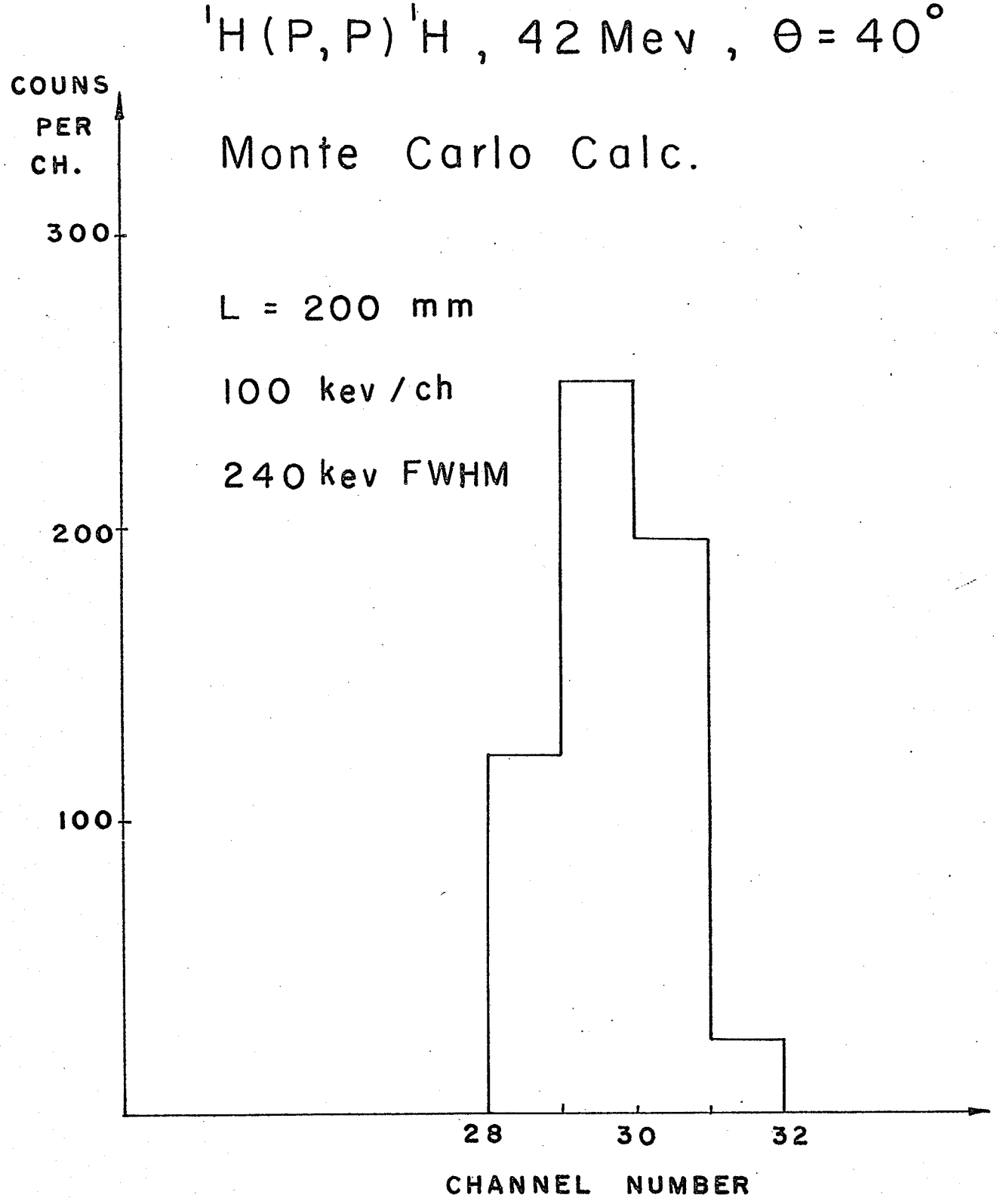
$^{1}H(P,P)^{1}H$, 42 Mev , $\theta = 40^{\circ}$
Monte Carlo Calc.
L = 200 mm
100 kev / ch
240 kev FWHM
COUNS PER CH.
300
200
100
28
30
32
CHANNEL NUMBER

Fig (2.16)

CHAPTER 3

EXPERIMENTAL PROCEDURE

3.1 Cyclotron, External Beam Facility

The high resolution beam line shown in Fig(1.1) was used in this experiment. The proton beam used was produced by the University of Manitoba 42" sector focused cyclotron[9]. A recently installed axial injection system injects a beam of negative hydrogen ions into the centre of the cyclotron at 11 kev[7]. The ions are deflected into the median plane by an electrostatic mirror and accelerated by a 28 kev RF voltage. Extraction is achieved by stripping the two electrons from the negative hydrogen ions using a thin Aluminium foil, the magnetic force reverses, sweeping the beam out of the cyclotron field. Changing the stripping foil radius and angle by the use of small magnetic field (the combination magnet) allows extraction of proton beams varying in energy from 20 - 50 Mev.

Setting up the beam through the high resolution beam line was described in details in section 1.6 .

3.2 Scattering Chamber

The 22" scattering chamber of the high resolution beam line was used in this experiment. The chamber has a rotating table which has grooves 10° apart for mounting detectors. There are 12 vacuum sealed connectors for detectors connections. the top of the chamber carries a vacuum lock and the target ladder slides through this

lock into the chamber.

The target ladder can hold 3 targets at the same time, although one place is normally occupied by a BeO screen used to observe the beam spot size through a T.V. closed circuit. Target angle and scattering angle are controllable from outside the chamber.

3.3 Targets

Carbon and Hydrogen targets were used in this experiment. The carbon target used was a self supported carbon foil with thickness 0.1 mg/cm² prepared by evaporation by Atomic Energy of Canada LTD - Chalk River Lab . For the hydrogen target we used a Mylar foil with thickness 0.86 mg/cm² .

3.4 Detectors

The detector used in this experiment was an ORTEC P-series position sensitive ion implanted detector. This detector is capable of simultaneously measuring the energy of the incoming particle and its position of interaction on the detector.

The detector used has the following measured specifications :

Alpha resolution	30 kev FWHM
Noise resolution	18.2 kev FWHM
Position resolution	0.3 mm
Length	25 mm

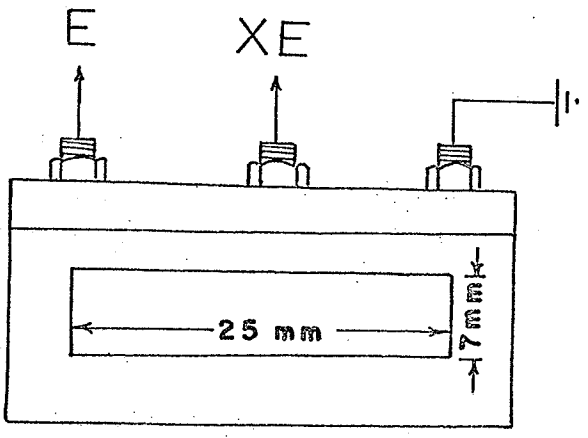

Position Sensitive Detector

Fig (3.1)

Fig (3.2)

Position Sensitive Detector Mount

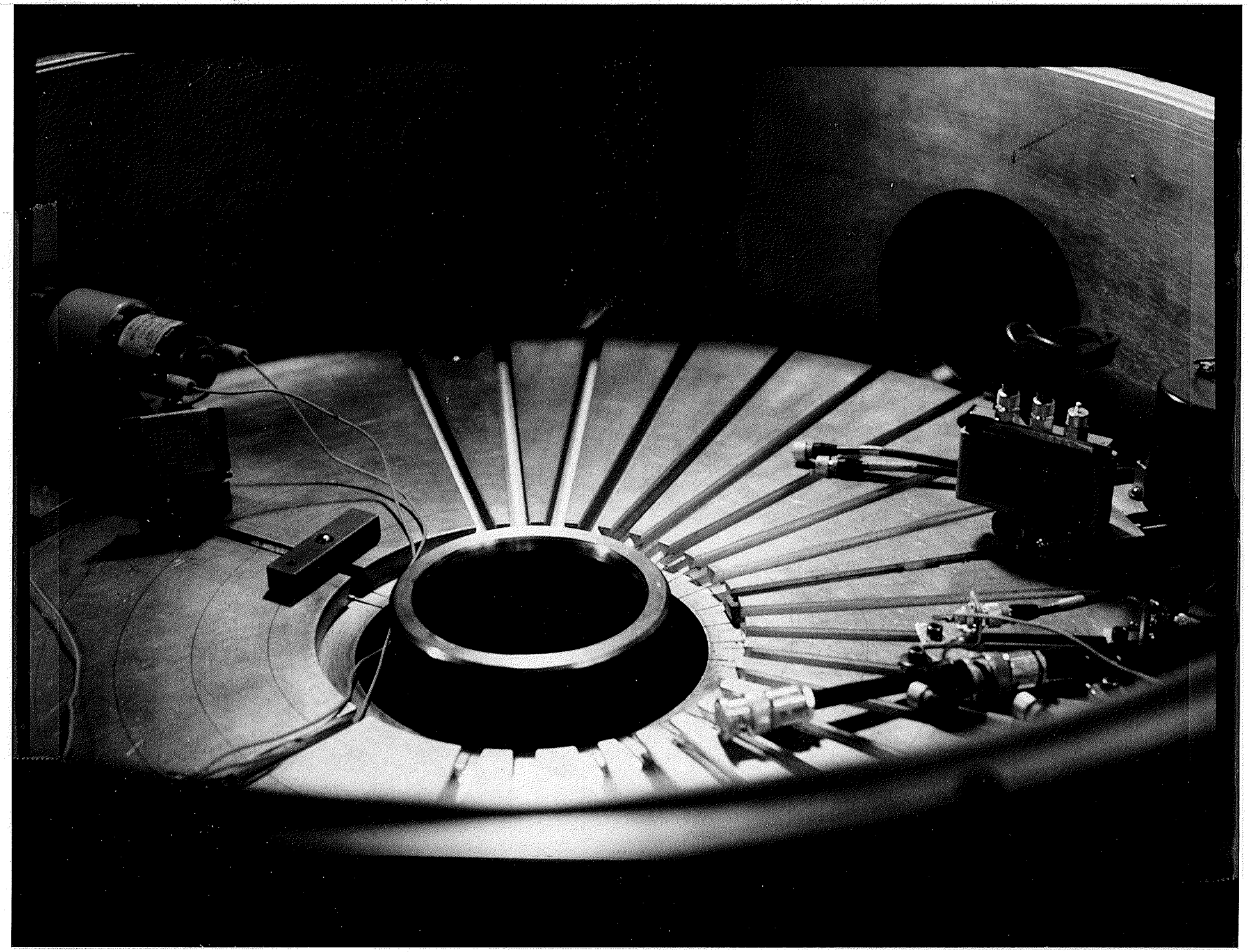

Width	7 mm
Depth	1000micron at 125V

Fig(3.1) shows a sketch for the position sensitive detector. One end terminal should be earthed, the middle terminal will give a pulse proportional to the energy of the incoming particle, the third terminal will give a pulse proportional to XE where X is the position of the impact of the incoming particle measured from the earthed end.

According to the discussion in section(2.7), the position sensitive detector (PSD) should be rotated to an angle which depends on both the scattering angle and the target angle. Hence , it was necessary to design a special detector mount that could be rotated and controlled from outside the scattering chamber. Fig(3.2) shows a photograph for the PSD mount used for that purpose.

3.5 Electronics

A block diagram for the electronics used and a diagram for the relative timing of the pulses are shown in Fig(3.3) and (3.4) respectively. The pulses proportional to E, XE,and ΔE -if any - were fed to 3 amplifiers then 3 single channel analyzers (SCA). By adjusting the levels of SCA we permitted only pulses with the required energy to pass. The outputs of the SCA's were fed to a coincidence unit.

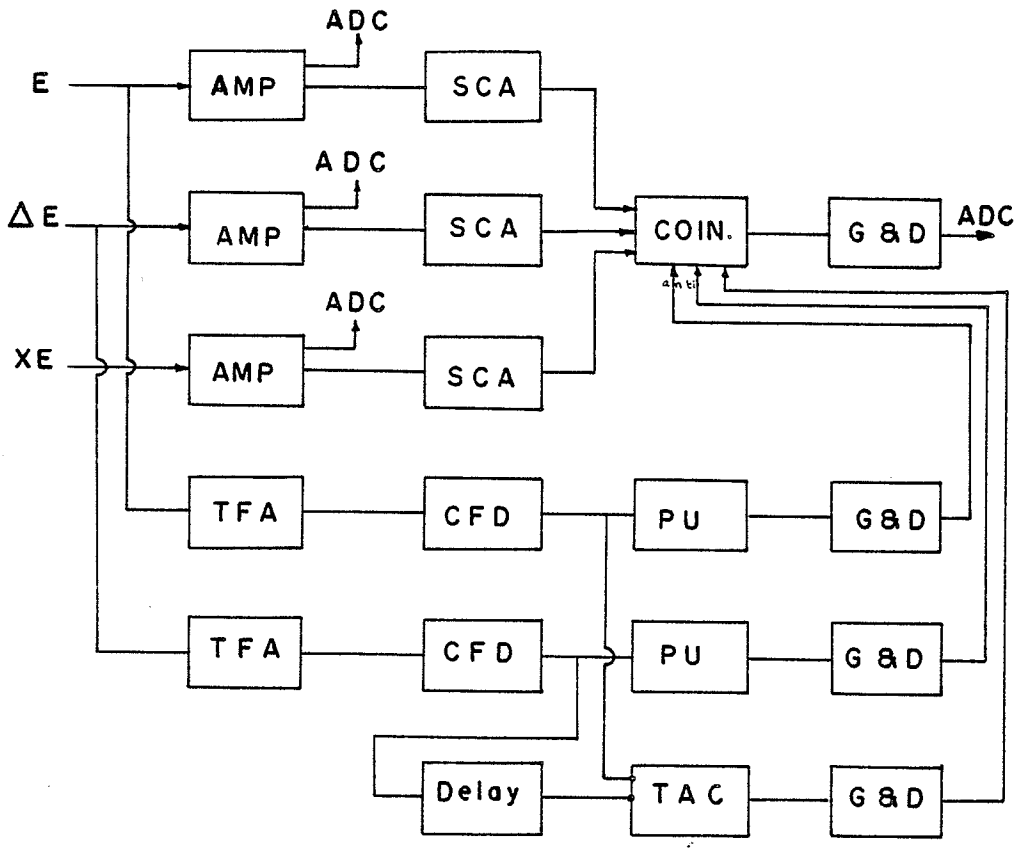

SCA= Single channel analyzer

CFD= Constant fraction discriminator

COIN= Coincidence unit

G&D= Gate & Delay

PU = Pile up gate

TAC = Time to amplitude converter

Fig (3.3) Electronic circuit diagram

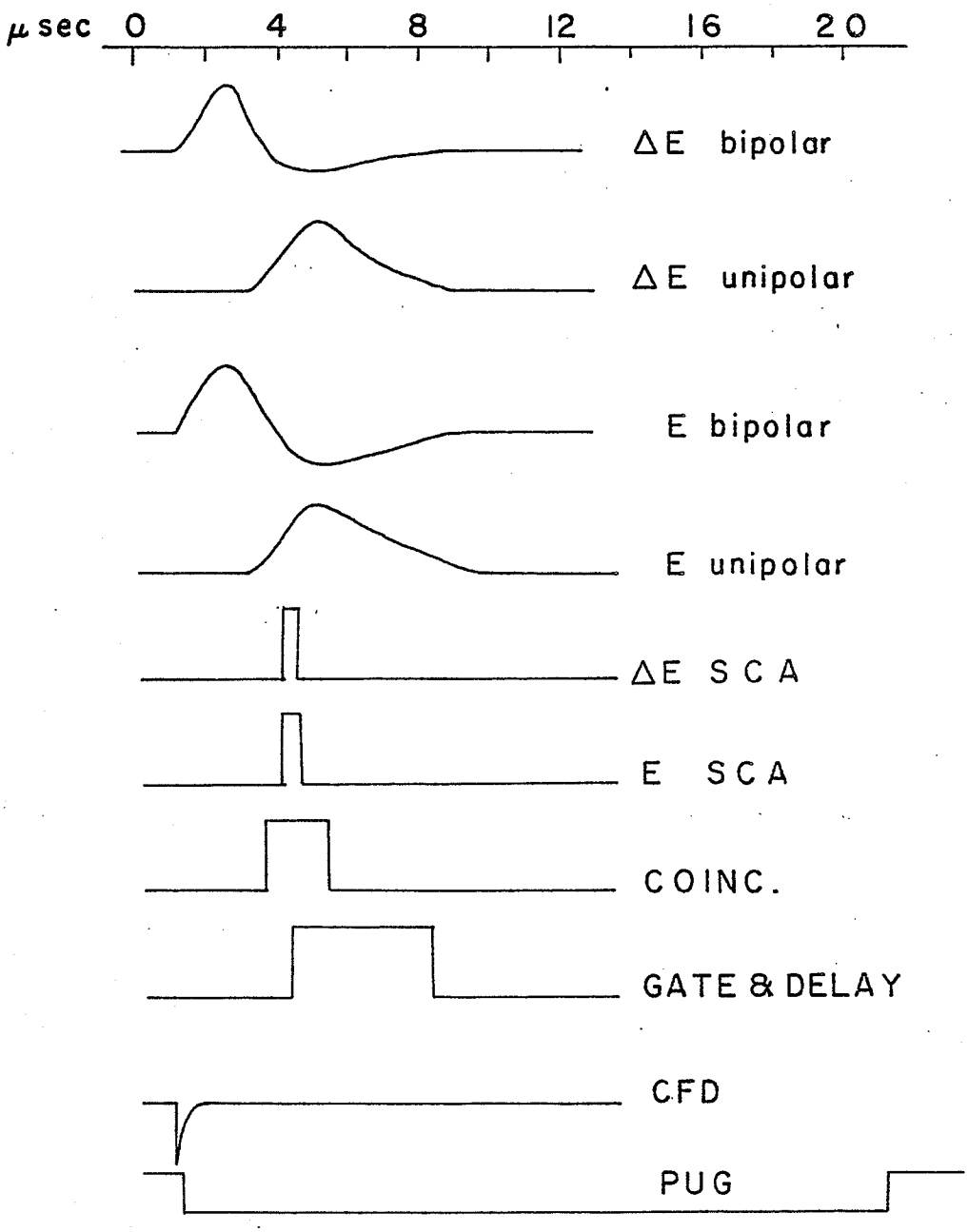
μsec 0 4 8 12 16 20
ΔE bipolar
ΔE unipolar
E bipolar
E unipolar
ΔE SCA
E SCA
COINC.
GATE & DELAY
CFD
PUG

Fig (3.4)

A pile up rejection circuit was used to reject the overlapping pulses - for ΔE and E lines only - which resulted in distorted pulses. The outputs from the constant fraction disc. (CFD) units were used to impose a fast coincidence on the pulses going to the ADC's.

3 Analog to Digital Converters (ADC) were used, interfaced to the PDP 15/40 computer which displayed the data and applied kinematic correction, as will be discussed in the following section.

3.6 Data processing

Two computer programs (one off-line and the other on-line) were used to process the data collected. Each event recorded by the position sensitive detector gives two pulses, proportional to E and XE respectively, besides we may have a E signal. The aim of using these computer programs was to collect an energy spectrum at a specified position (x_o) on the detector (corresponding to scattering angle θ_o). Particles arriving along the detector at positions different than that specified for collection should be corrected kinematically.

By using these programs we have the provision either to collect a single energy spectrum by specifying only one position on the detector to which the energy of all events should be corrected, or to collect several energy spectra by dividing the detector into a number of segments. For each segment we specify a single point to

which we correct the energy of other events in the segment.

Treating the detector as one region is useful in the case of low cross-section scattering experiments, while dividing the detector into segments is useful when one needs energy spectra with 2-3° intervals.

The off-line computer program POSEDE[12] was used to calculate two two-dimensional kinematic correction coefficient matrices of position on the detector vs. excitation energy. These coefficients - as will be seen below- were used to correct the energy of all events recorded along the segment under consideration. The size of these matrices was limited to 10X10 due to computer core limitation, i.e. the maximum number of segments to which we can divide the detector is 10.

The matrices calculated by POSEDE were then incorporated into the on-line data taking program and appropriate corrections to the data were made on an event-by-event basis.

In the following sections we will give a brief description of these programs

3.6.1 The off-line program POSEDE[12]

This Fortran program gets as input detailed information about the masses of the particles involved in the reaction , the projectile energy, geometrical arrangement (target angle, detector angle, ...), ADC offsets, number

of segments desired on position sensitive detector, number of energy intervals, a reference peak to calibrate the position, the gain factor between E and ΔE -if any-, and the angles to which the data in the segments have to be corrected (one angle for each segment). The computer program uses this informations to calculate first-order correction coefficients as follows :

Consider a segment on the detector with position limits x_1, x_2. Suppose that we want to collect data at the position x_o.

The relation between the energy (E) of an event arriving in this interval at position x (i.e. with scattering angle θ_o) and the energy (E_o) of an event arriving at the position x_o (corresponding to scattering angle) can be written as : (to the first order)

$$E = E_o + \frac{dE}{dx}(x - x_o)$$

$$\text{i.e.} \quad E_o = E - \frac{dE}{dx}(x - x_o)$$

According to the last equation, if we add the correction term $-\frac{dE}{dx}(x-x_o)$ to the energy of the event arriving at x its energy will be kinematically corrected as if it arrived at x_o.

Faster computation made it necessary to write the last equation on the following form :

$$E_o = E + Z(x - x_1) + T$$

where

$$Z = -\frac{dE}{dx} \quad , \quad T = -\frac{dE}{dx}(x_1 - x_o)$$

The program calculates these coefficients Z, Y for each position interval, recalculate them for each energy interval corresponding to different states of excitation of the final nucleus.

To show that the above linear correction used in calculating the coefficients Y, Z gives results with enough accuracy, we consider the following example :

Consider the reaction $^{12}C(P,\alpha)^{9}B$ with an incident proton energy of 35.2 Mev . A PSD (25 mm long) is placed normaly at 180 mm away from the target position with its centre placed at a lab scattering angle of 40°. The length of the detector will subtend a range of scattering angles = 8°.

First, consider the whole detector as one region and suppose that the energy specrum will be collected at the position corresponding to scattering angle $\theta=40^{\circ}$. As mentioned earlier, the energies of all events arriving alsewhere on the detector (i.e. with scattering angle $\neq 40^{\circ}$) should be corrected using the linear relation :

$$E_{\circ} = E - \frac{dE}{d\theta}(\theta - 40)$$

If we consider the worst case, namely the case of an event arriving at the edge of the PSD with scattering angle = 44°. From the kinematic curve shown in Fig(3.6), $E(\theta=44^{\circ}) = 22.6945$ Mev, and

$\frac{dE}{d\theta} = -0.1177$ Mev/

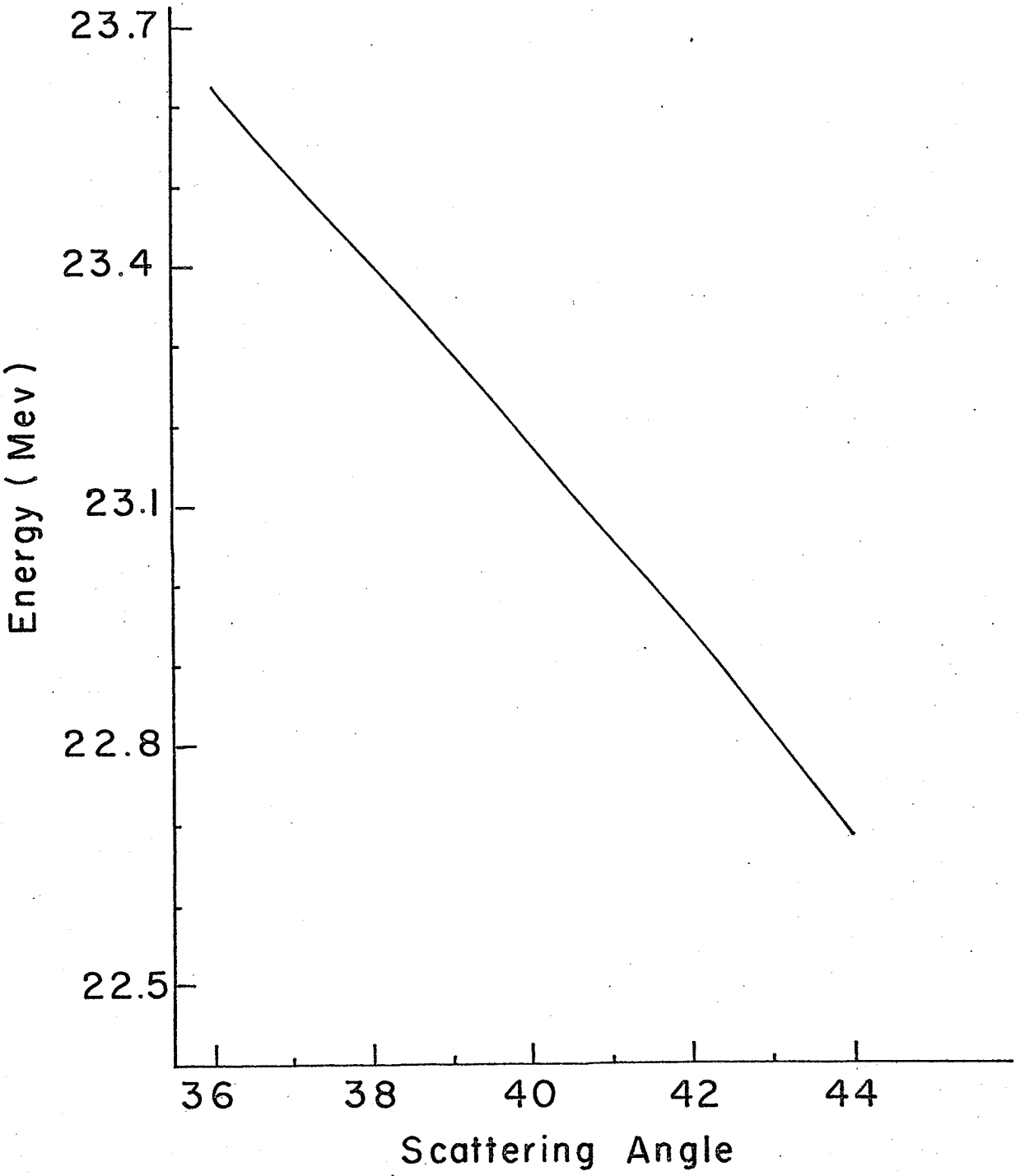

Fig (3.6)

$E(\theta = 40^{\circ}) = 22.6945 + .117\ (44-40) = 23.1625$ Mev

i.e. the program will correct the energy of this event to be 23.1625 Mev while it is actually 23.1764 Mev according to Fig(3.6). That means that the error is 14 Kev in the worst case.

Of course, by dividing the detector into several regions this difference will decrease significantly. e.g. consider the above example when we divide the detector into 4 segments. Each segment will subtend 2 . Again , cosider the segment whose centre is placed at 40° scattering angle . For an event arriving with scattering angle = 41°, its energy will be corrected as follows :

$E(\theta = 40^{\circ}) = 23.0586 + .117X1 = 23.1756$ Mev

The error in this case is 1 Kev .

From the above examples we conclude that the linear correction adopted by the program is reasonable. The greater the number of divisions on the detector the better the accuracy of the kinematic corrections. Also it is preferable to choose the correction refrence points to be in the middle of each segment, in this way the correction will be more accurate.

3.6.2 The on-line computer program (mirad+ adcmlp+ possen)

This program receives from the ADC's 3 signals for each event :

signal A : proportional to ΔE

signal B : proportional to E

signal C : proportional to XE

The program performs the following data reduction :

i. calculates D = A / N

where N is the ratio of the gain used on E and amplifiers.

ii calculates G = C*K /(B + I)

where

G = position X in a 500 channel spectrum (channel 500 corresponde to 25 mm)

I = offset on the energy ADC

K = rescaling factor, depends on XE-signal amplification.

iii. calculates F =D + B

After these calculations the aquisition program selects the appropriate matrix elements calculated by POSEDE by searching through position and energy interval arrays in which the event falls , as shown in Fig(3.7) then uses the numbers Y(i,j) and Z(i,j) to calculate the corrected energy E' of the event :

$$E' = F + Y(i,j) + Z(i,j)\,(G - X(i-1))$$

where

X(i-1) = the lower boundary of the position interval in which the event falls.

All the quantities A, B, C, D, G, F, E' can be displayed by MIRAD.

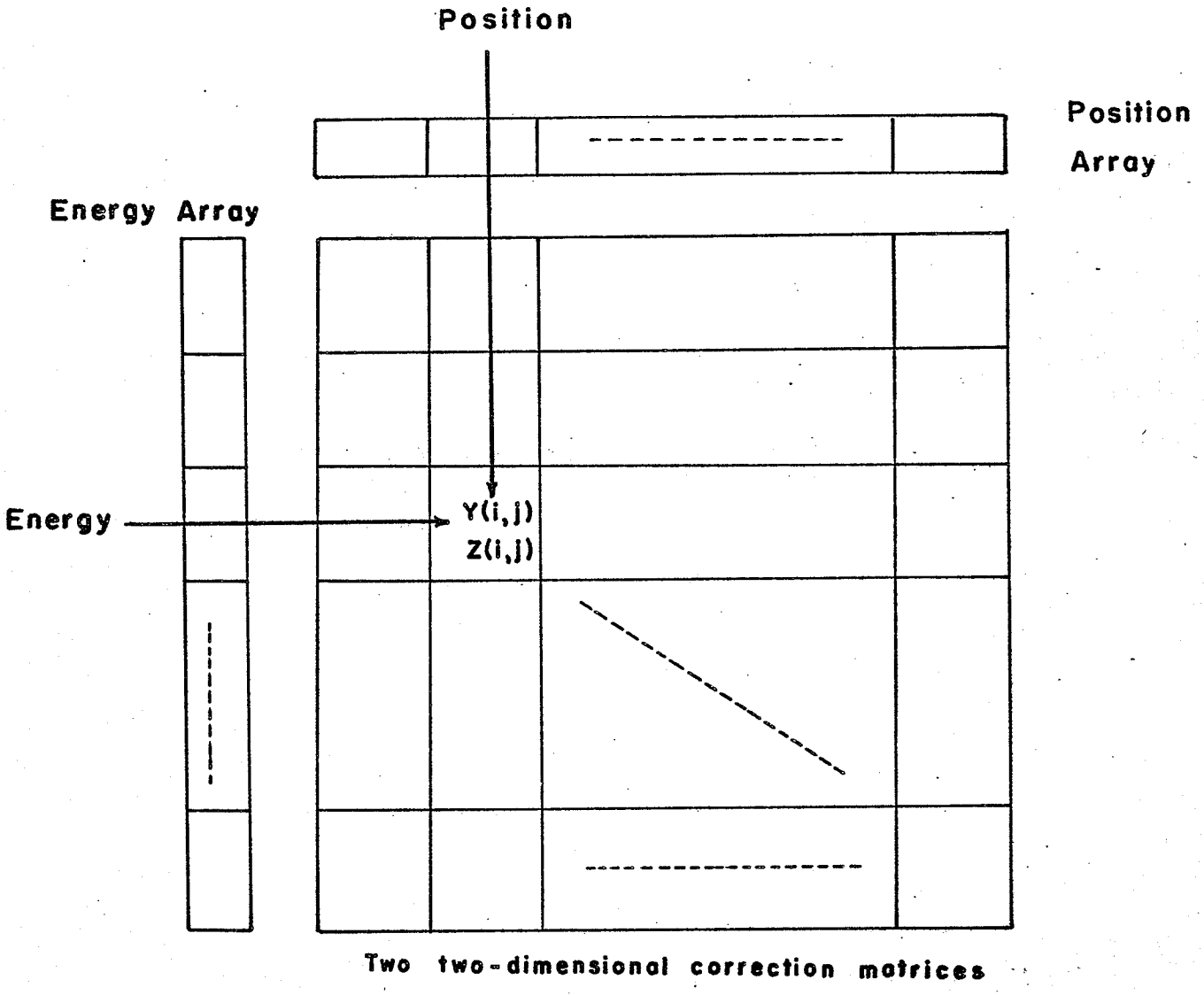
Position
Position Array
Energy Array
Energy
Y(i,j)
Z(i,j)
Two two-dimensional correction matrices

Fig (3.7)

Programs listings, loading procedure, and the required assignments can be found in ref.(12) .

3.7 Quadrupole triplet setting

The major difficulty in the experimental measurement was the determination of the quadrupole triplet QE3,QE4, QE5 field strengths for waist condition at the target and post-target positions.

Since at the time of performing this experiment there was no apparatus available in the lab for beam scanning, we depended on calculations to determine the quadrupole triplet strengths for waist conditions.

As we have seen in Fig(1.7), the phase space ellipse at the image slits is almost upright in the horizontal plane. So the method described by Resmini[11] for waist-to-waist transfer can be used.

Before we used this method we tested the accuracy of the calculated values as follows :

We started with the design values of the field strengths B3 and B4 of the quadrupoles QE3 and QE4[2] and used the method mentioned above to determine the field strength B5 in the quadrupole QE5 corresponding to a waist condition at the target position. The data used was as follows :

B3 = 1.59 KG

B4 = 3.74 KG

E_p = 42 Mev

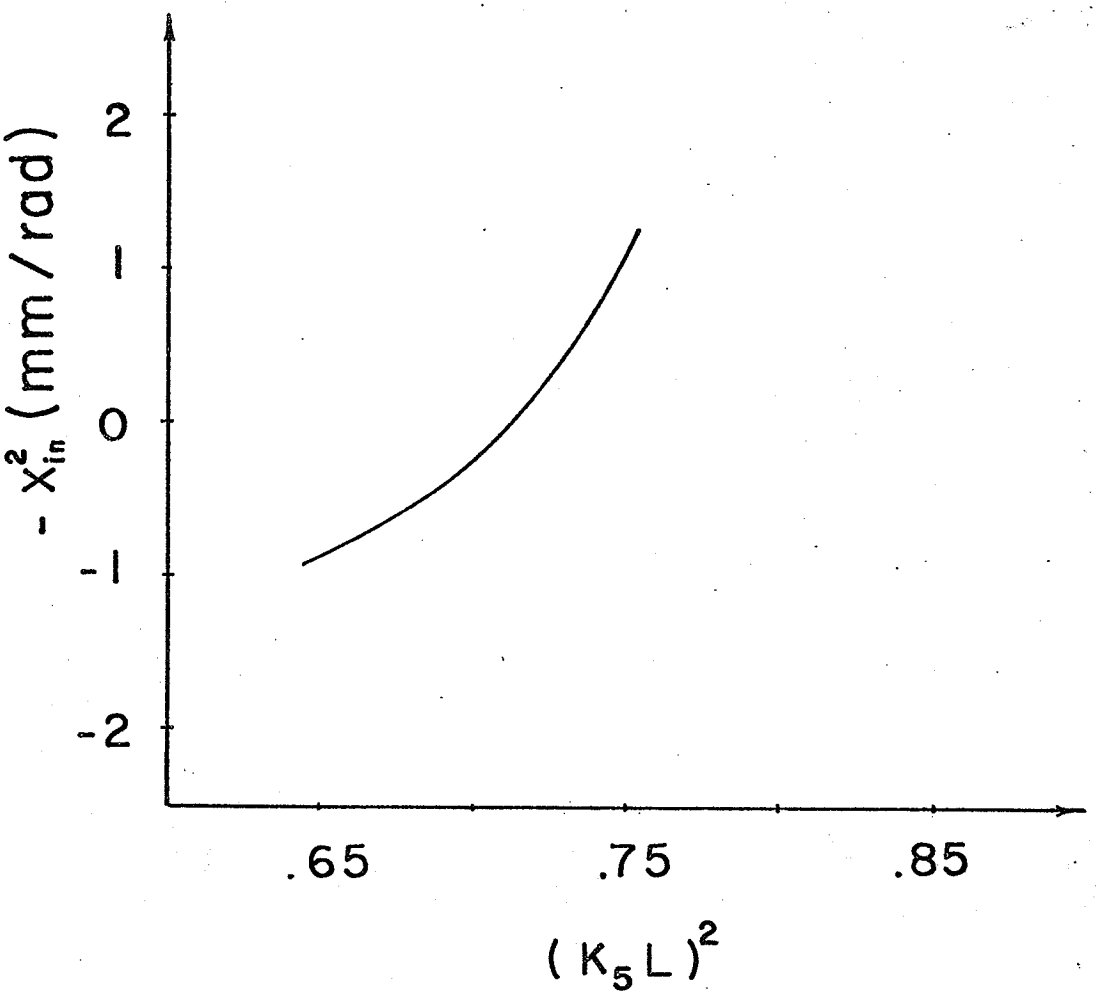

Fig (3.8)

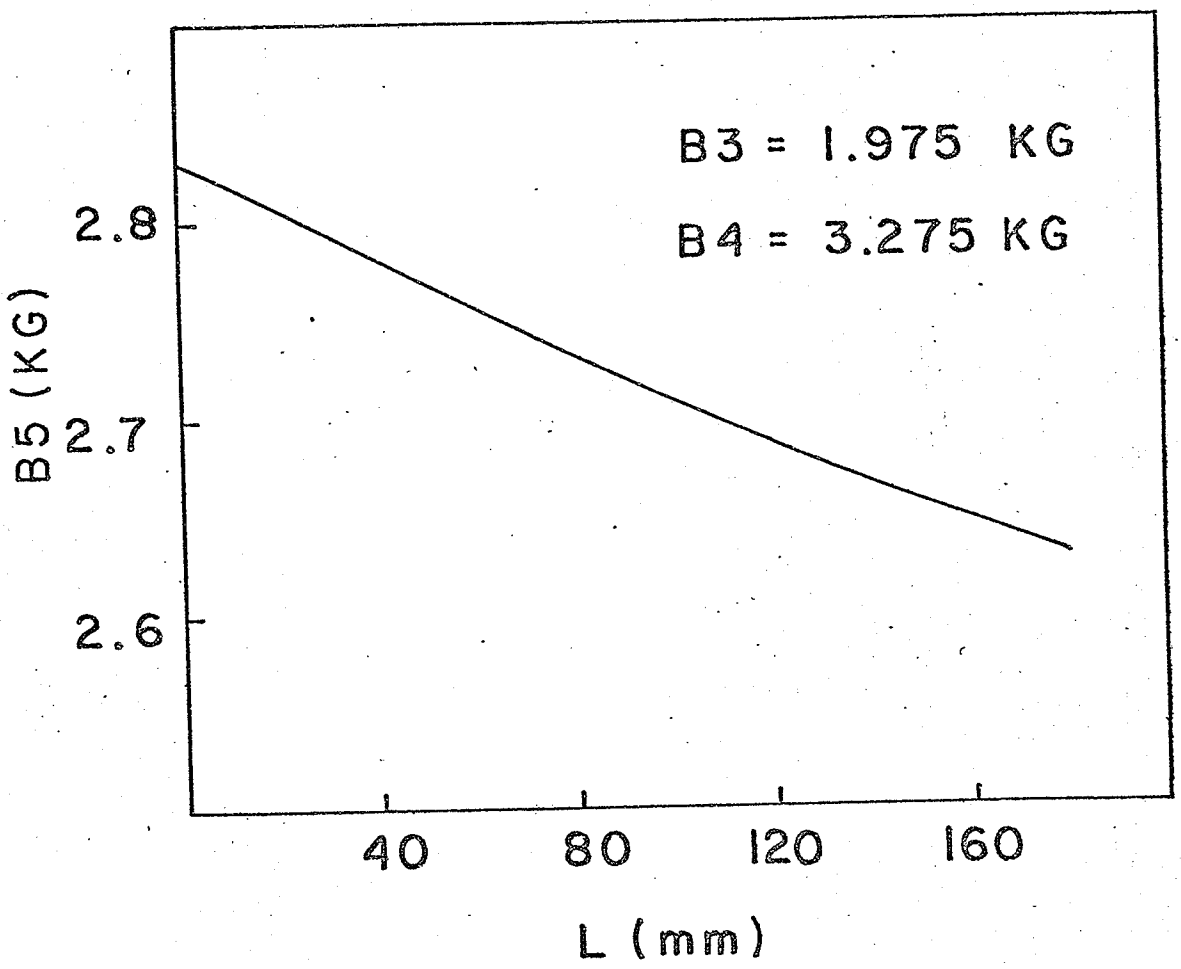

Fig (3.9)

Following the procedure described by the Resmini we got the plot shown in Fig(3.8) for K L)^2 vs. X where

$$K^2 = \frac{B5}{5.156 \times \text{rigidity of particles}}$$

L = length of QE5

X = characteristic length of the beam.

For a beam with typical characteristic length X = 0.016 mm/mrad Fig(3.8) shows that the value of the field B5 of the quadrupole QE5 should be 2.72 KG in order to get a waist while the design value is 2.74 KG . The effect of this difference was investigated and it was found that by using this method the actual position of the waist will be uncertain by 1 cm . We considered this error reasonable and we used this method to determine the field strengths corresponding to a waist at any required position.

Fig(3.9) shows a plot for the values of the field B5 vs. the waist distance L. This curve can be used to calculate the value of B5 corresponding to a waist condition at any distance L. The curve shown in Fig(3.9) was calculated using the following data :

B3 = 1.975 KG

B4 = 3.275 KG

E_p = 42.5 Mev

X^2 = 2.6×10^{-4} (mm/mrad)^2

Fig(3.9) and other similar curves were used in determining the quadrupole settings for a waist condition during the run of this experiment.

3.8 Experimental contribution to the resolution

The experimentally measured energy resolution is not due to beam divergence only, but there are several contributions which have to be calculated and substracted from the measured values before any proper judgement on the theory or comparison with the theoritical calculations can be made.

A brief discussion for these contributions is given below.

(i) Instrumental resolution of the detector system

The PSD used for this experiment has an energy resolution of 30 Kev FWHM. Besides, the electronic modules used (amplifiers) contribute also to the energy resolution. The overall contribution of the detector system to the energy resolution was estimated to be 35 Kev .

(ii) Contribution due to detector position resolution

The PSD used has a position resolution of 0.3 mm, this will result in an angular uncertainity. The contribution of this position resolution to the energy resolution depends on the target-detector distance and the kinematic energy spread of the reaction under investigation. e.g.

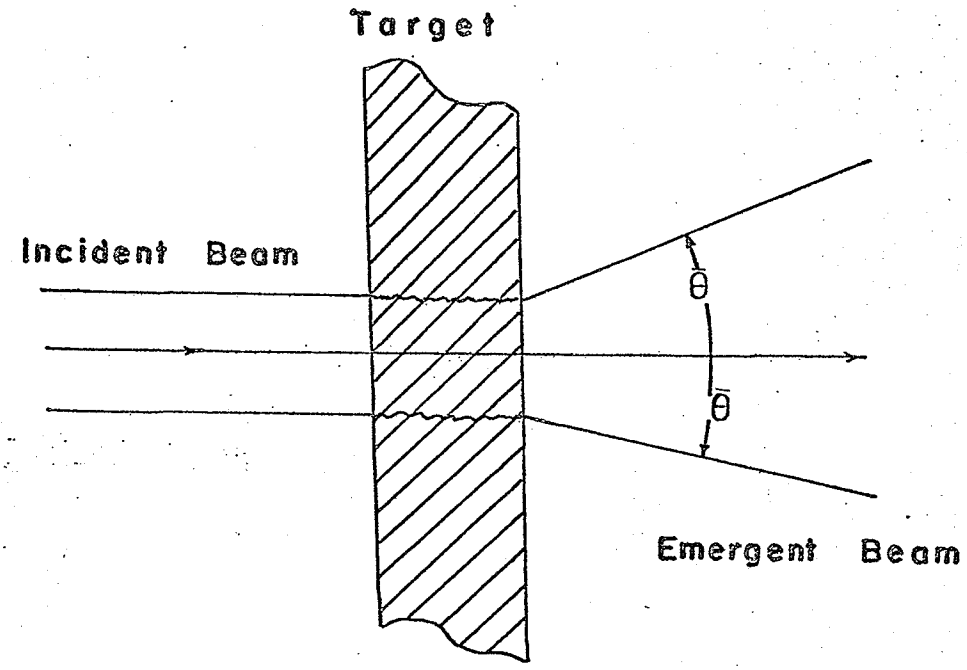

Fig (3.10)

Schematic Illustration of Angle Straggling

if the detector is 180 mm away from the target, then the position resolution will result in angular resolution of 0.3/180 rad. .

(iii) Multiple scattering

Due to multiple collisions in the target, the originally collimated beam will broaden and the emergent beam will exhibit some angle straggling, as shown in Fig(3.10). This straggling can be described by the mean angle $\bar{\theta}$. The value of can be calculated for a particle of energy E and charge Ze from the expression given by Marmier[10].

The problem in calculating accurate value for was whether to assume that the nuclear reaction took place at the begining of the target, or after the projectile had traversed part or the whole target thickness. For this experiment, we calculated the value of $\bar{\theta}$ for both extreme cases, then we chose a value for $\bar{\theta}$ which lies between these two extremes. As an illustration, consider the reaction $^{12}C(P,\alpha)^{9}B$ with the following data :

Target thickness	0.1 mg/cm^2
Target angle	20°
Scattering angle	40°
Incident proton energy	35.2 Mev

Using the expression mentioned above, the value of will be $2.78 \times 10^{-2^{\circ}}$ if the reaction takes place at the end of

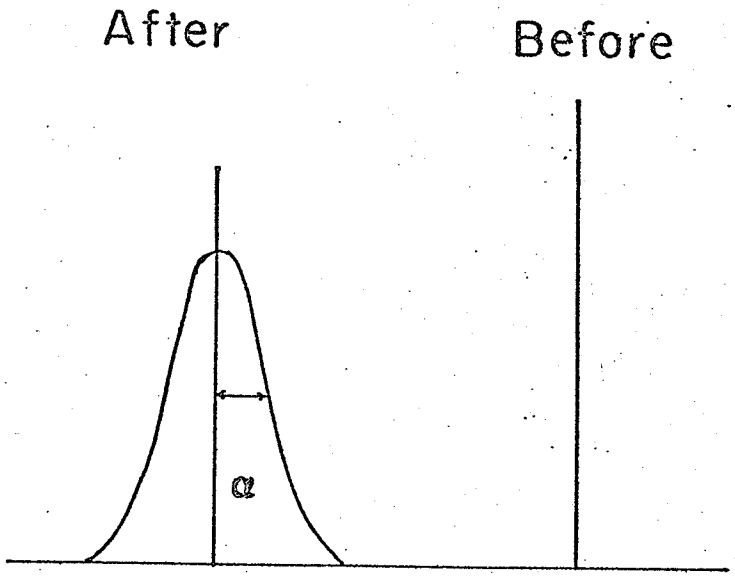

Fig (3.11) Illustration of energy straggling

the target thickness, while the value of will be 8.3×10^{-20} if the reaction takes place at the begining of the target. In our estimation the value of we would consider is 5×10^{-20}. The contribution to the energy resolution is then readily determined from the kinematics of the reaction.

The same procedure was done for all the reactions investigated in this experiment.

(iv) Energy straggling[10]

The energy loss of the charged particles is caused mainly by discrete , random collisions with atomic electrons. The statistical nature of this process produces fluctuations of energy losses from an initially monoenergetic beam as it passes through the target. This will lead to a statistical distribution of the end energy. The parameter which describes this straggling ( ) -shown in Fig(3.11) - can be calculated from the expression given by Marmier[10] . As in the case of multiple scattering, the actual value of energy straggling we considered was a value between the two extremes. As an illustration consider the same example as in (iii) :

If we assume that the incident proton will suffer the energy sraggling , the straggling parameter (α) will be 3.1 Kev i.e. the contribution to the energy resolution due to energy straggling is 7.32 Kev FWHM. On the other

hand, if the reaction takes place at the beqining of the target the straqqling parameter α will be 6.2 Kev i.e. the contribution in this case will be 14.6 Kev FWHM . In our estimation we would consider the contribution to the energy resolution due to energy straqqling as 11 Kev FWHM.

(v) Energy loss in target

The proper value of energy loss for each reaction was obtained from special tables[13].

CHAPTER 4

EXPERIMENTAL PROCEDURE

4.1 Run set up

Experimental measurements were carried out for the reactions $^{12}C(P,\alpha)^{9}B$ and $^{1}H(P,P)^{1}H$ to demonstrate experimentally the theory discussed in chapter 2.

The beam extracted from the cyclotron was 1-2 μA at the stripping foil. This resulted in a 5-15 nA beam at the Faraday cup. The correct beam energies were maintained by setting the analyzing magnet field strengths according to Fig(1.8). The quadrupole triplet QE3,QE4, QE5 field strengths corresponding to a waist condition were calculated using the method described in section (3.7). A closed circuit television camera was used to observe the beam spot as it struck a flourescent BeO screen.

4.2 The $^{12}C(P,\alpha)^{9}B$

Experimental measurements were carried out on the reaction C(P,) B to test the theory described in chapter 2. Data was collected for different scattering angles, different incident proton energies , and different number of detector segments. Table (4.1)I shows the data selection for this reaction.

Fig (4.1), (4.2), (4.3) show the experimental results obtained for the ground state peak only. Each of the figures displays the measurements for L=0 and L≠0 cases . The beam used in these measurements had a characteristic

Table (4.1)

Data Selection and Experimental

for $^{12}C(P,\alpha)^{9}B$ Reaction

I. DATA SELECTION

Scattering angle	40	60	70
Target angle	20	30	35
Proton energy (mev)	35.2	42.5	34.6
Detector-target distance (mm)	192	170	192
Number of detector segments	4	1	4
Beam characteristic length X(mm/rad)	30	30	30
L (mm)	186	166	186

II. EXPERIMENTAL RESULTS

(resolution FWHM Kev)

Waist at target position	205	350	220
Waist at distance L (as in I)	63	175	65
Improvement factor	3.25	2	3.38

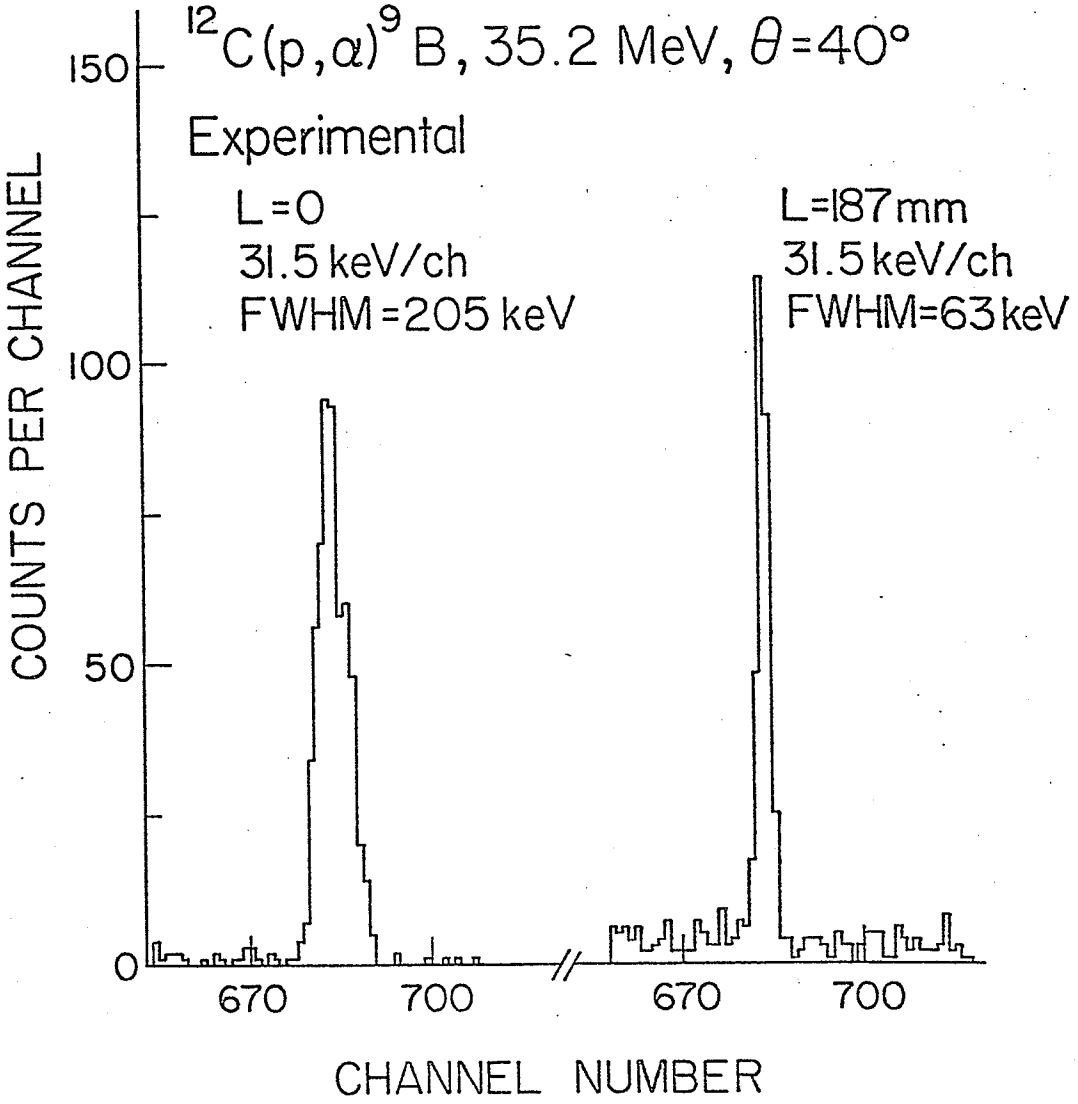
$^{12}C(p,\alpha)^{9}B$, 35.2 MeV, θ=40°
Experimental
L=0
31.5 keV/ch
FWHM=205 keV
L=187mm
31.5 keV/ch
FWHM=63keV
COUNTS PER CHANNEL
150
100
50
0
670
700
670
700
CHANNEL NUMBER

Fig (4.1)

$^{12}C(P,\alpha)\,^{9}B$, 42.5 Mev , $\theta = 60°$

Experimental

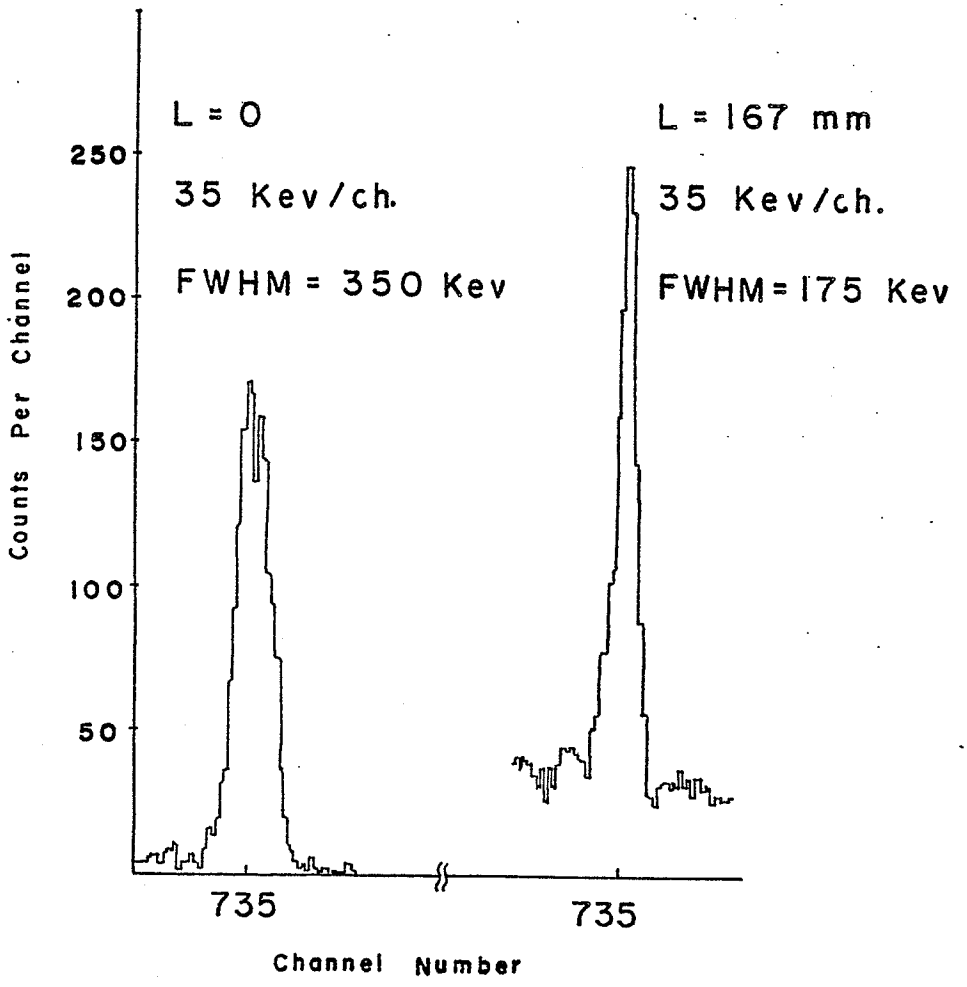

Fig (4.2)

$^{12}C(p,\alpha)^{9}B$, 34.6 Mev, $\theta = 70°$

Experimental

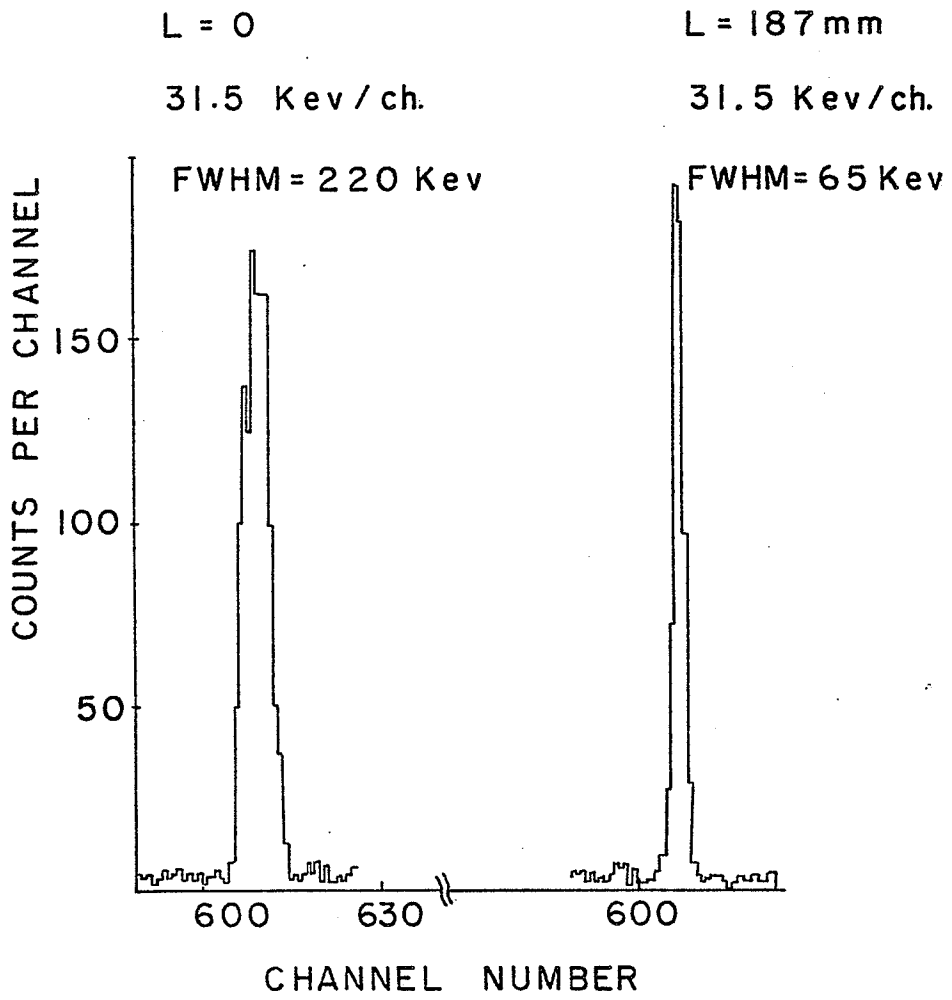

Fig (4.3)

length of X=30 mm/rad, and the kinematic matching distance L was calculated on this basis from Fig(2.4) and (2.10). The measured energy resolution values are tabulated in table (4.1)II togather with the improvement factors. It should be noticed that this improvement factor is the one before substracting the experimental contributions mentioned in section (3.8).

It may be noticed that in some measurements , as in Fig(4.1) the background in the case of L≠0 is greater than that in the case of L=0. The reason for this is that by moving the waist to a certain distance beyond the target, the physical size of the beam spot increases to the extent that the beam may hit the target frame and causes this background.

4.3 The $^{1}H(P,P)^{1}H$ reaction

Data selection for this reaction is shown in table (4.2)I. The beam used had a characteristic length X=50 mm/rad, and all kinematic matching distances were calculated on this basis. Figs(4.4) and (4.5) show the results obtained which are tabulated as well in table (4.2)II.

4.4 Comparison of the theoretical calculations with experiments

Before comparing the energy resolution improvement measured experimentally with those the theory predicts,

Table (4.2)

Data selection and experimental results

for the $^{1}H(P,P)^{1}H$ reaction

I. DATA SELECTION

Scattering angle	60	63
Target angle	30	30
Proton energy (Mev)	42.5	42.5
Detector-target distance (mm)	170	165
Number of detector segments	3	3
Beam characteristic length	50	50
L (mm)	155	155

II. EXPERIMENTAL RESULTS

(resolution FWHM Kev)

Waist at the target position	720	740
Waist at distance L (as in I)	260	280
Improvement factor	2.77	2.64

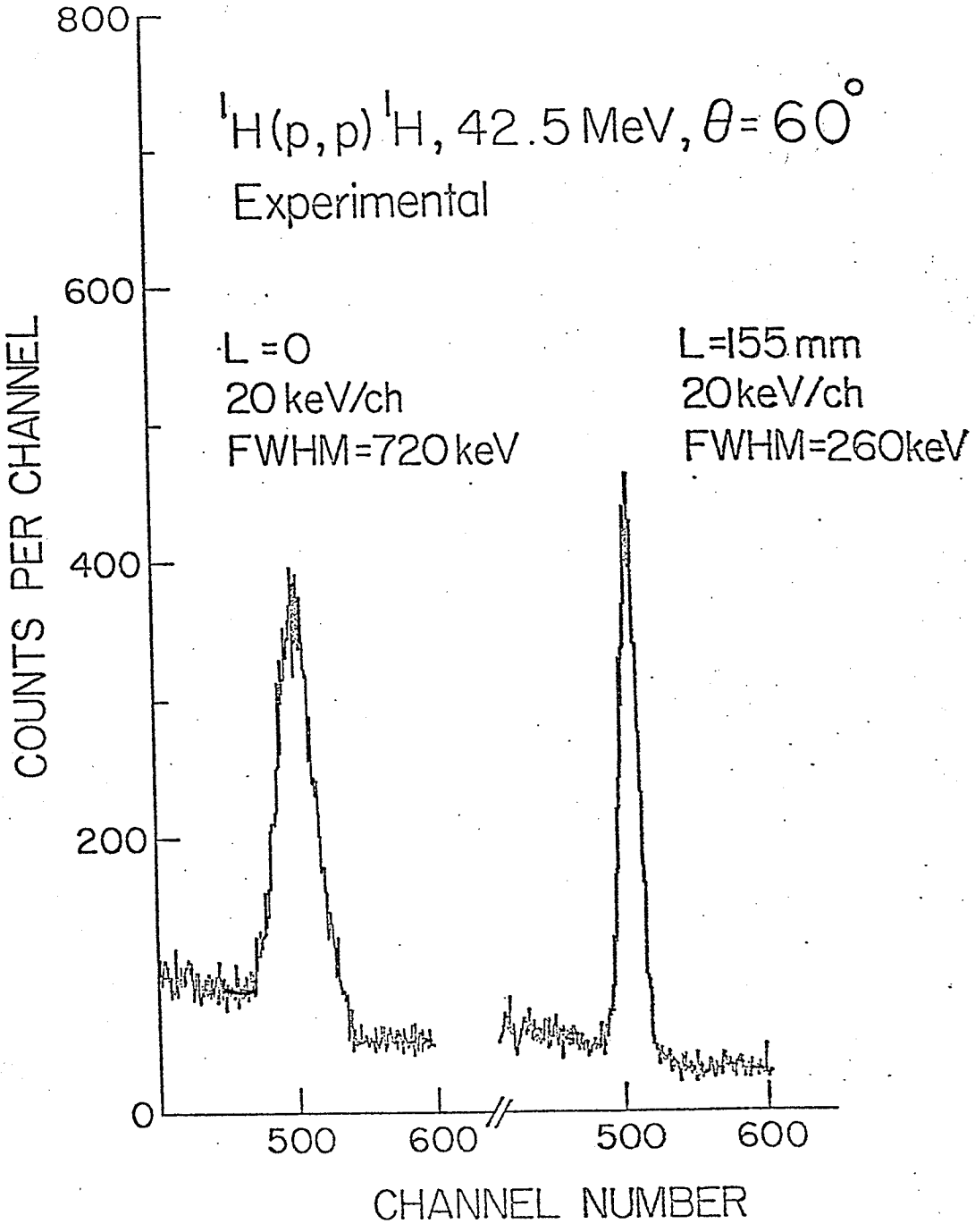
800
600
400
200
0
COUNTS PER CHANNEL
$^1H(p,p)^1H$, 42.5 MeV, $\theta = 60^\circ$
Experimental
L = 0
20 keV/ch
FWHM = 720 keV
L = 155 mm
20 keV/ch
FWHM = 260 keV
500
600
500
600
CHANNEL NUMBER

Fig (4.4)

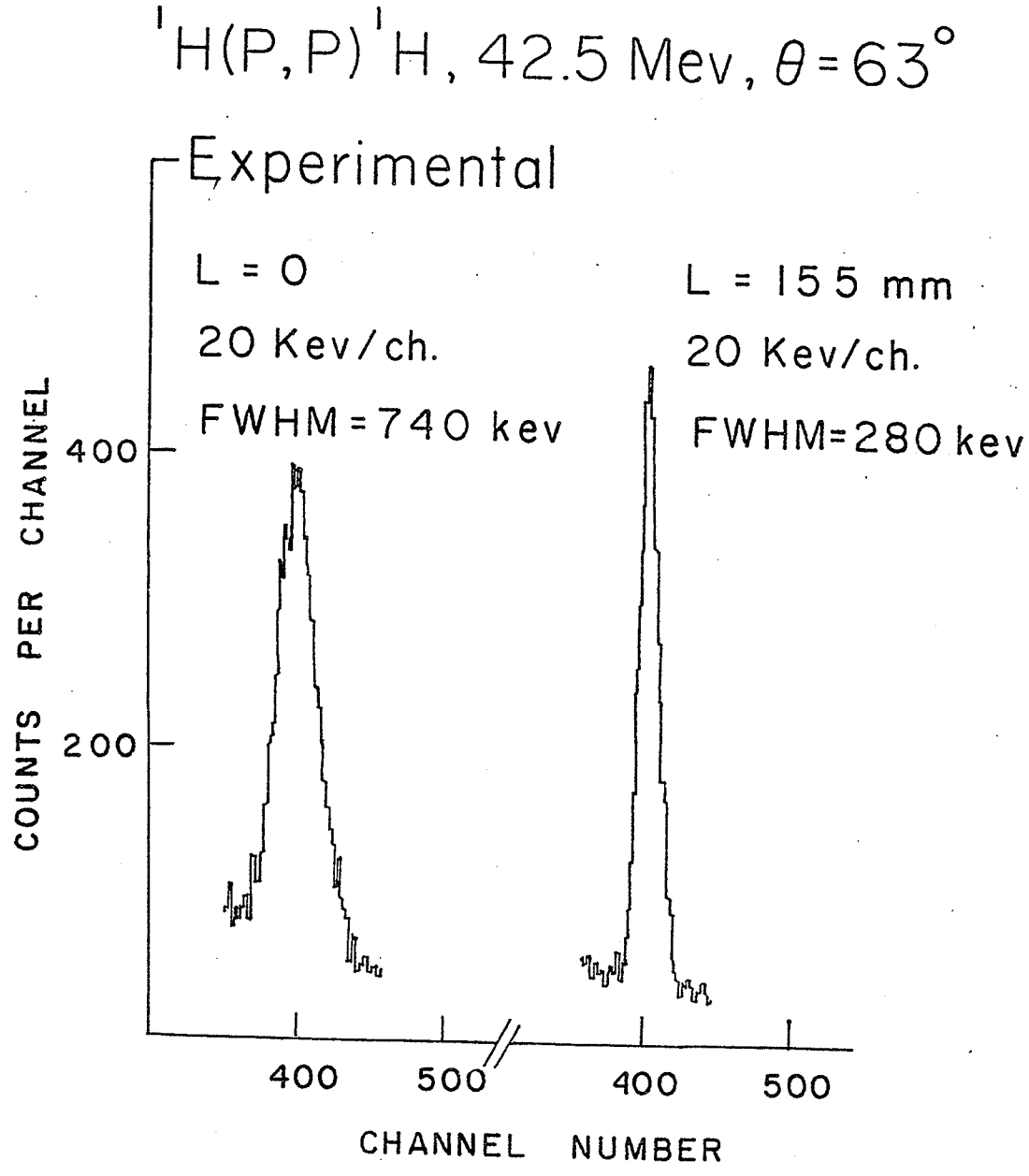
$^{1}H(P,P)^{1}H$, 42.5 Mev, $\theta = 63°$
Experimental
L = 0
20 Kev/ch.
FWHM = 740 kev
L = 155 mm
20 Kev/ch.
FWHM = 280 kev
COUNTS PER CHANNEL
400
200
400
500
400
500
CHANNEL NUMBER

Fig (4.5)

we have to substract all the experimental contributions to the energy resolution discussed in section (3.8).

Tables (4.3)I and (4.4)I show the experimantal contributions to the energy resolution for the reactions $^{12}C(P,\alpha)^{9}B$ and $^{1}H(P,P)^{1}H$, respectively. These contributions were added in quadrature and substracted from the measured energy resolution in order to get the energy resolution due to beam divergence only. The results are shown in tables (4.3)II and (4.4)II.

Theoretical calculations of the energy resolution for the two reactions mentioned above had been done using the computer program KCORR described in section (2.8.1) using the same experimental data shown in tables (4.1)I and (4.2)I. (scattering angle, target angle, beam characteristic length,...). The value of the quantity β was assigned as described in section (2.8). The results are shown in Figs(4.6), (4.7), (4.8), and (4.9).They are also tabulated in tables (4.5) and (4.6) for the reactions $^{12}C(P,\alpha)^{9}B$ and $^{1}H(P,P)^{1}H$, respectively.

Now, a comparison can be made between the results of the theoretical calculations and the measured energy resolution due to beam divergence only. The best way -in our opinion- to do such a comparison is through the improvement factor i.e. the energy resolution for L≠0 divided by the energy resolution for L=0. Such a comparison is shown in tables (4.7) and (4.8) for the two

Table (4.3)

Experimental contribution to the measured energy resolution for the reaction $^{12}C(P,\alpha)^{9}B$

I. Parameter	$\theta=40^{\circ}$	$\theta=70^{\circ}$
1. Detector and electronics (kev)	35	35
2. Detector angle	11	12.5
3. Energy loss in target +multiple scattering+energy straggling	40	43
Total of above contributions (added in quadrature) Kev	54.3	56.8
II. Measured energy resolution due to beam divergence only (Kev)		
L =0	198	213
L = Matching	32	32

Table (4.4)

Experimental contribution to the measured energy resolution for $^{1}H(P,P)^{1}H$ reaction

I. parameter	$\theta=60$	$\theta=63^{\circ}$
1. Detector and electronics (Kev)	35	35
2. Deictor pcsition resolution	65	60
3. Energy loss in target + multiple scattering + energy straggling	152	152
Total of above contributions (added in quadrature Kev)	169	167
Measured energy resolution due to beam divergence only (Kev)		
L =0	700	721
L = Matching	198	225

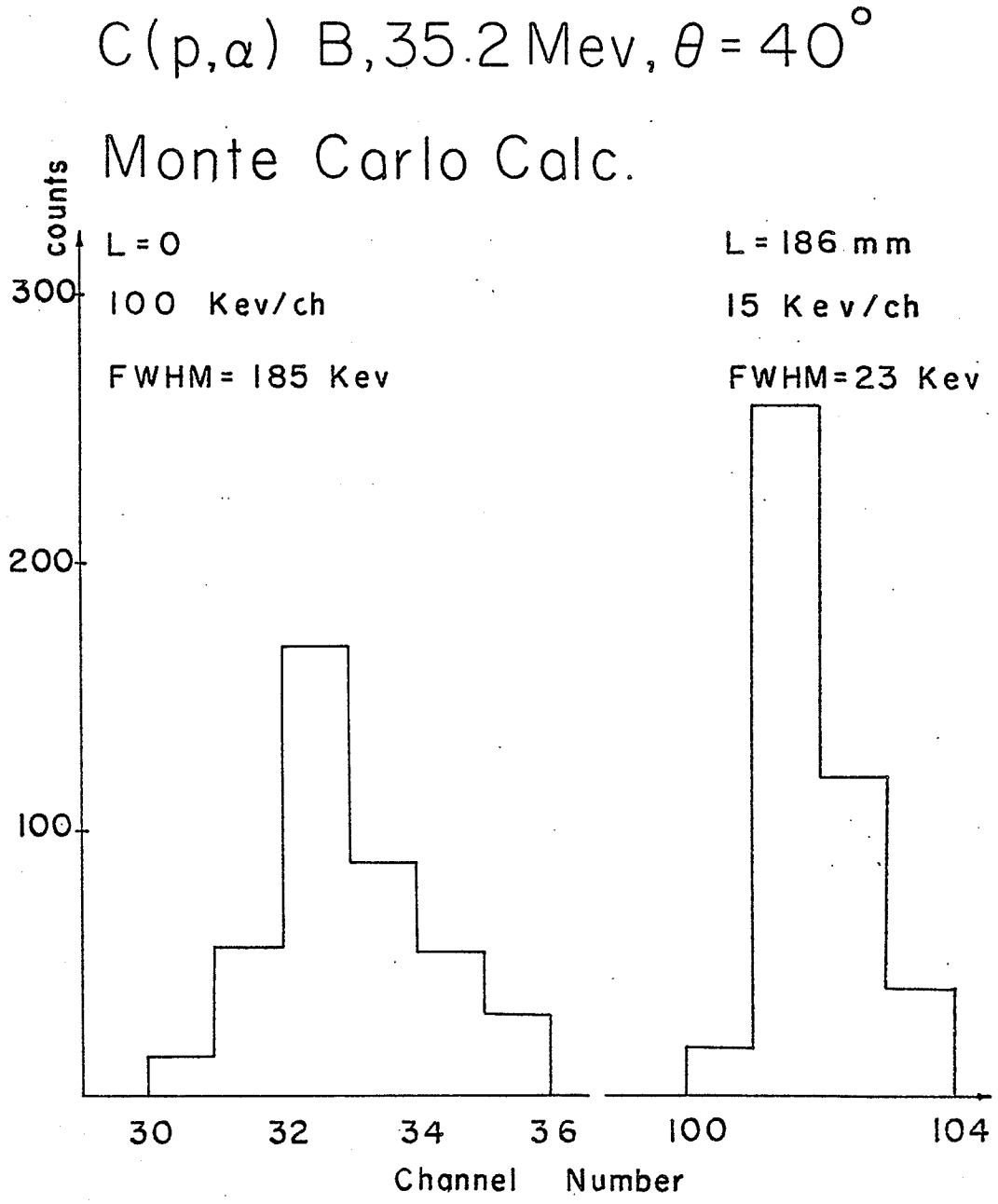
C(p,α) B, 35.2 Mev, θ = 40°
Monte Carlo Calc.
counts
300
200
100
L = 0
100 Kev/ch
FWHM = 185 Kev
L = 186 mm
15 Kev/ch
FWHM = 23 Kev
30
32
34
36
100
104
Channel Number

Fig (4.6)

$^{12}C(P,\alpha)^{9}B$, 34·6 Mev , $\theta = 70°$

Monte Carlo Calc.

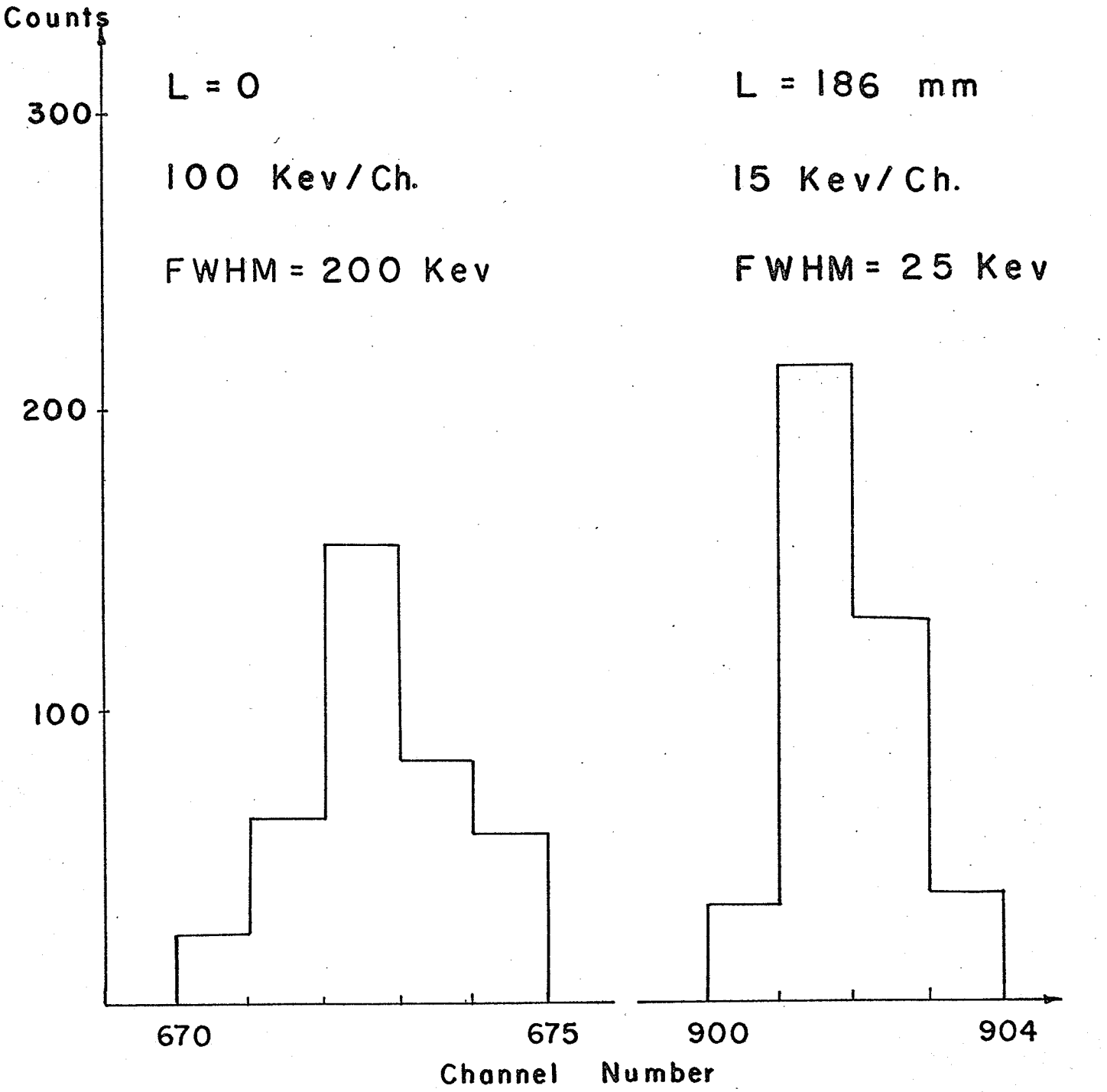

Fig (4.7)

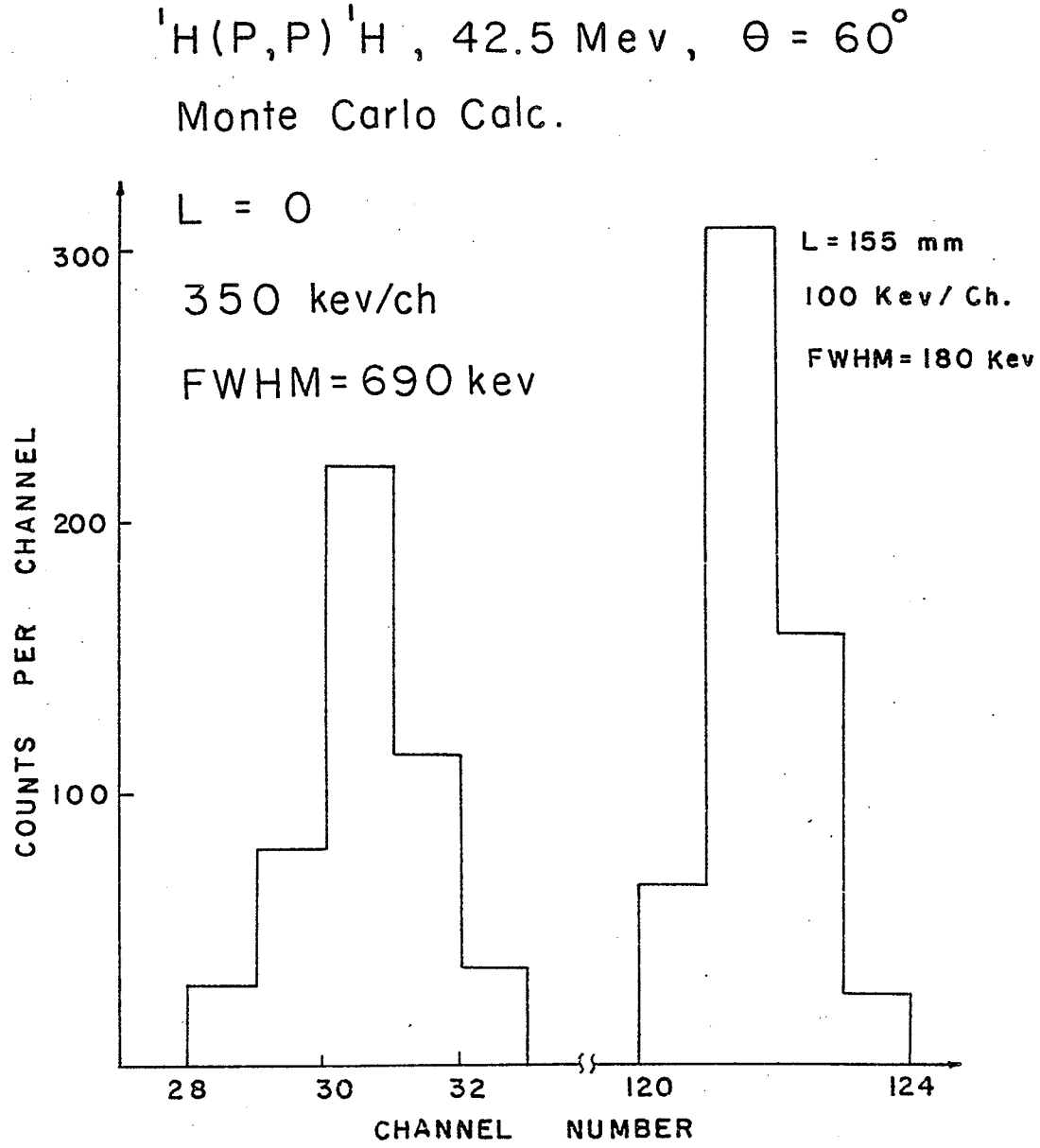
$^1H(P,P)^1H$, 42.5 Mev , $\Theta = 60^\circ$
Monte Carlo Calc.
L = 0
350 kev/ch
FWHM = 690 kev
L = 155 mm
100 Kev / Ch.
FWHM = 180 Kev
COUNTS PER CHANNEL
300
200
100
28
30
32
120
124
CHANNEL NUMBER

Fig (4.8)

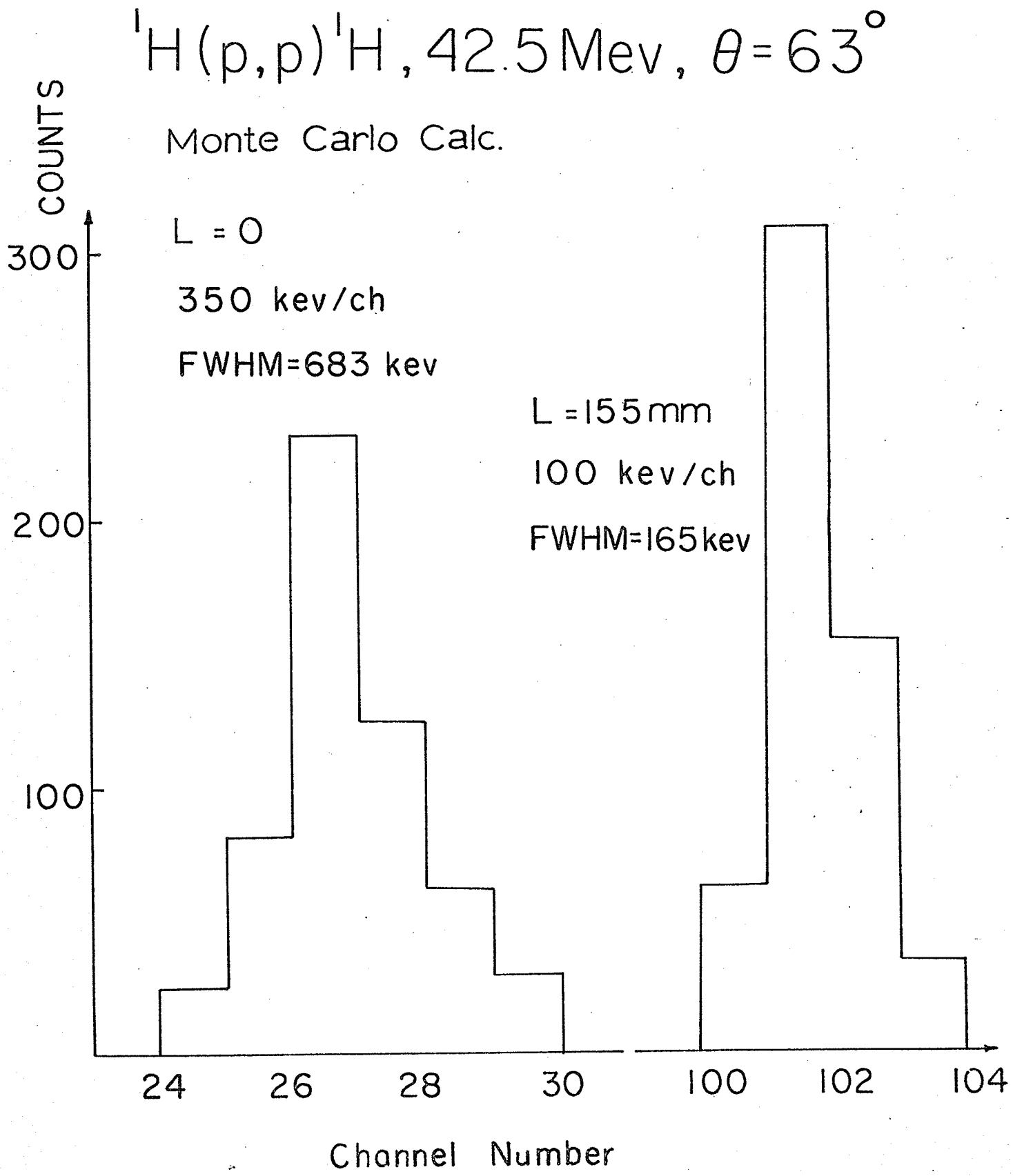
$^1H(p,p)^1H$, 42.5 Mev, $\theta = 63°$
Monte Carlo Calc.
COUNTS
300
200
100
L = 0
350 kev/ch
FWHM=683 kev
L = 155 mm
100 kev/ch
FWHM=165 kev
24
26
28
30
100
102
104
Channel Number

Fig (4.9)

Table (4.5)

Calculated energy resclution for the reaction $^{12}C(P, \alpha)^{9}B$

Scattering angle	40	70
Target angle	20	35
Proton enrgy (Mev)	35.2	34.6
Detector-target distance (mm)	192	192
Beam charac. length (mm.rad)	30	30
" β "	.01	.01
Energy resolution FWHM (Kev):		
L = 0	185	200
L = Matching	23	25

Table (4.6)

Calculated enrgy resolution for

the reaction $^{1}H(P,P)^{1}H$

Scattering angle	60	63
Target angle	30	30
Proton energy (Mev)	42.5	42.5
Detector-target distane (mm)	170	165
Beam charac. length (mm/rad)	50	50
" β "	0.9	0.9
Energy resolution FWHM(Kev):		
L =0	690	683
L = Matching	180	165

Table (4.7)

Comparison between the measured and the calculated enrgy resolution improvement factor for the reaction $^{12}C(P,\alpha)^{9}B$

Scattering angle	Target angle	Impr. fact. (calculated)	Impr. fact. (measured)
40	20	8.0	6.2
70	35	8	6.6

Table (4.8)

Comparison between the measured and the calculated energy resolution improvement factor for the reaction $^{1}H(P,P)^{1}H$

Scattering angle	Target angle	Impr. fact. (calculated)	Impr. fact. (measured)
60	30	3.8	3.2
63	30	4.1	3.5

reacticns under consideration .

Discussion

From tables (4.7) and (4.8) we noticed that althouqh we improved the measured energy resolution by a factor of 3.5-6.6 , the theory still predicts a slightly higher improvement factors. There are several reasons responsible for this :

1. The approximation used in the derivation of the kinematic matching condition (2.4).
2. The assumption that all the particles in the phase space ellipse on target are represented by those along the axis A-A in Fiq(2.8)a .
3. The approximation made in section (2.7) regarding the shape of the position sensitive detector.
4. The uncertainity in determination of the waist condition at different positions.
5. The uncertainity in the determination of the value of the beam characteristic length X and β .
6. The first-order approximation used in calculating the kinematic correction coefficients in the computer program POSEDE.

4.5 Measurements at backward scattering angle

A single experimental measurement was performed for the reaction $^{12}C(P,\alpha)^{9}B$ at backward scattering angle of 110°. The waist was moved to a point in front of the

$^{12}C(P,\alpha)\,^{9}B$, 35.2 Mev , $\theta = 110°$

Experimental

L = -186 mm

31.5 Kev / Ch.

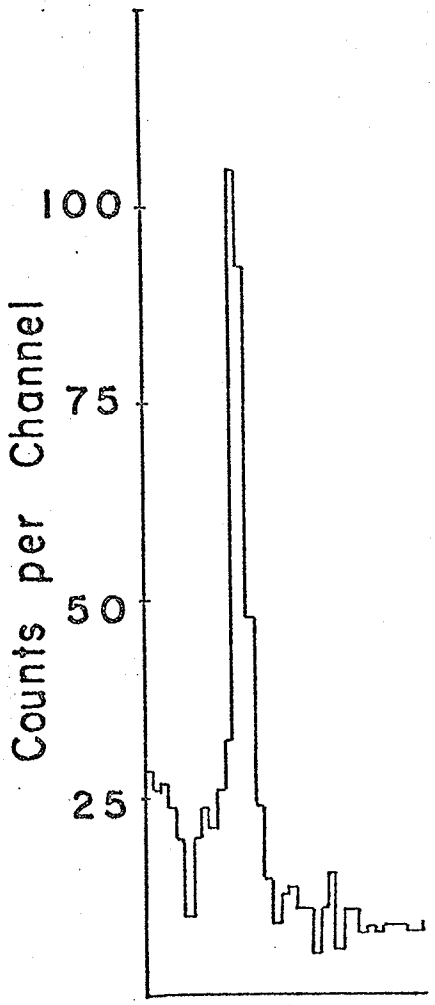

FWHM = 63 Kev

Fig (4.10)

target,as discussed in section (2.2). The target angle was 325°,the detector-target distance =192 mm , proton energy = 35.2 Mev. The beam used had a characteristic length of 30mm/rad. The kinematic matching distance was calculated to be -186 mm. (the - sign means that the waist is in front of the target).

Fig(4.10) shows the result of the measurement. The measured energy resolution is 63 KevFWHM, while for the case of L=0 we predict an energy resolution of about 200 Kev FWHM. This shows that the kinematic matching is effective also for backward angles.

SUMMARY AND CONCLUSION

First part of this thesis included a summary of details of the momentum analysis system of the high resolution beam line.

In the second part a technique was described for improving the energy resolution of scattering experiments by shifting the horizontal waist at the target position to a point downsrteam. This has been tested by a computer program which traces rays through the analysis system and calculates the energy resolution. An improvement in the energy resolution by a factor of 4-8 had been obtained.

The technique has been tested experimentally using Carbon and Hydrogen targets. The results showed the technique to be effective , hence improvement by a factor of 3-6 has been observed.

The slight difference between the calculated and the observed improvement factors came from the error accompanied with shifting the waist to a certain distance, the detector shape approximation , and the first-order approximations used in performing the kinematic corrections.

Appendix I

a. First order matrix R

The first order transformation matrix used by TRANSPORT has the following construction :

$$\begin{matrix} R_{11} & R_{12} & R_{13} & R_{14} & R_{15} & R_{16} \\ R_{21} & R_{22} & R_{23} & R_{24} & R_{25} & R_{26} \\ R & R & R & R & R & R \\ R & R & R & R & R & R \\ \vdots & & & & & \\ R_{61} & R_{62} & R_{63} & R_{64} & R_{65} & R_{66} \end{matrix}$$

where the subscript 1 refers to x, 2 to x', 3 to y, 4 to y', 5 to l, and 6 to d.

b. Second order matrix T

The second order transformation matrix has the follow-

ing construction :

T_{111}

T_{112} T_{122}

T_{113} T_{123} T_{133}

T_{114} T_{124} T_{134} T_{144}

T_{115} T_{125} T_{135} T_{145} T_{155}

T_{116} T_{126} T_{136} T_{146} T_{156} T_{166}

⋮

T_{611}

T_{612} T_{622}

T_{613} T_{623} T_{633}

T_{614} T_{624} T_{634} T_{644}

T_{615} T_{625} T_{635} T_{645} T_{655}

T_{616} T_{626} T_{636} T_{646} T_{656} T_{666}

Appendix II

NUCLEAR INSTRUMENTS AND METHODS 137 (1976) 261–266; © NORTH-HOLLAND PUBLISHING CO.

ENERGY RESOLUTION IMPROVEMENT IN SCATTERING EXPERIMENTS USING HIGHLY DIVERGENT ACCELERATOR BEAMS

W. R. FALK, O. ABOU-ZEID and L. PH. ROESCH

Cyclotron Laboratory, Department of Physics, University of Manitoba, Winnipeg, Canada

Received 14 June 1976

A method of improving the energy resolution in scattering experiments that employ a highly divergent accelerator beam is discussed. The technique involves displacing the usual beam-waist at the target location to a point downstream from the target. Angular resolution is improved along with the improvement in the energy resolution.

1. Introduction

The high resolution beam analysis system[1]) at the Cyclotron Laboratory of the University of Manitoba has been designed to accept as input a beam characterized by an emittance (half-width times half-divergence) in the horizontal plane of $xx' = 15$ mm·mrad. Typically this results in an angular divergence of up to $\pm 2°$ on target if the full acceptance of the system is utilized. Kinematic energy spread resulting from this divergence is very serious for the lighter target nuclei, to the extent that use of the momentum-analyzed beam is completely negated. For example, in the $^{12}C(p, \alpha)^{9}B_{gs}$ reaction at 40 MeV and a scattering angle of 30°, the kinematic energy spread is 109 keV/deg, increasing to 165 keV/deg at 70°. For heavier targets where the kinematic energy spread is less serious, the angular divergence may still be unacceptably large for measurement of an angular distribution.

In this paper a technique is described that greatly reduces the kinematic energy spread (by a factor of 3–8), and results in a corresponding improvement in the angular resolution, while at the same time utilizing the full beam acceptance into the system. A similar technique, referred to as dispersion matching, is well known and applied in magnetic spectrograph detector systems[2,3]), which are matched to the characteristics of the beam incident on target. The present detector system is a more conventional one comprising a solid state position sensitive detector. A solid angle of up to 7 mstr can be achieved with the detector employed.

The momentum analysed beam is characterised by a fractional energy spread of $\Delta E/E = 5 \times 10^{-4}$, or 25 keV at 50 MeV incident proton energy[1]). This energy spread is thus considerably smaller than that arising from kinematic effects, and hence in the discussion following we concentrate solely on improving the latter contribution to the overall energy spread.

2. Description of technique

Fig. 1 illustrates a typical scattering (or reaction) geometry for a projectile beam incident on a target, and a detector placed at a laboratory scattering angle θ. It is at once clear from the diagram that if the scattering angle to the detector is to have the same value θ for each incident projectile, a one-to-one correspondence between position and slope of the particle trajectory on target is implied. The position and slope are denoted by x_t and x_t' respectively. Equality of the scattering angles obviously eliminates the kinematic energy spread, not only for elastic scattering but for any and all nuclear reactions as well. Simultaneously, the unique value of the scattering angle removes the problem of the angular resolution in determining the angular distribution. The detector of fig. 1 has been assumed to subtend a negligibly small horizontal angle as seen from the target.

The relation between x_t and x_t' to achieve the above conditions is readily shown to be

$$x_t/x_t' = -\frac{d\cos\alpha}{\cos(\theta-\alpha-x_t')} \approx -\frac{d\cos\alpha}{\cos(\theta-\alpha)}, \qquad (1)$$

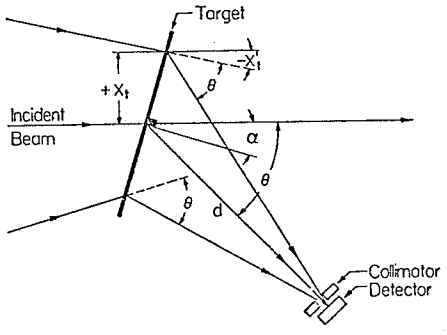

Fig. 1. Scattering or reaction geometry of a beam incident on a plane target to yield identical scattering angles for all projectiles. The position and slope of a projectile trajectory at the target are denoted by x_t and x_t' respectively.

since $x'_t \leqslant 1$ and $(\theta-\alpha)$ is generally selected to be less than $\frac{1}{4}\pi$. Here d is the target-detector distance, α the target angle, and θ the scattering angle as previously noted. Eq. (1) can be readily applied for cases $\theta > \frac{1}{2}\pi$ by simply reversing the direction of the incident beam.

Of course, this unique correlation between x_t and x'_t for trajectories of particles from an accelerator beam cannot be achieved. It is possible nonetheless, to approximate the desired condition. Consider the phase-space ellipse of the beam in the horizontal plane as depicted in fig. 2. Typically, the experimenter selects parameters of the beam-optics so as to produce a horizontal waist at the target position, i.e. an upright ellipse, as in fig. 2b. At $x=0$, the beam has a half-divergence of x'_w. If the ellipse is rotated to the position shown in fig. 2a the half-divergence at $x=0$ is clearly reduced, this reduction depending upon the degree of rotation. Particles lying on the axis A–A of this rotated ellipse are characterized by the condition $x_t/x'_t = -\text{constant}$, satisfying the condition set forth in eq. (1). To the extent that particles along the axis A–A are representative of all the particles in the beam, the kinematic matching condition is fulfilled.

The two ellipses shown in fig. 2 are simply related: a drift space rotates the ellipse in the clockwise direction[4]). Hence if the ellipse orientation shown in fig. 2a is arranged on target, a horizontal waist (an upright ellipse) will be produced at a point downstream. The modus operandi suggested by the foregoing is the following: from a knowledge of the location and properties of the horizontal waist at a post-target location the properties of the ellipse on target can be determined. Details of these calculations are presented in the next section.

3. Target ellipse properties deduced from the post-target waist

In the following discussion we adopt much of the notation and the conventions found in ref. 4. The ellipse at the post-target waist can be expressed as

$$\alpha_w x^2 + \gamma_w x'^2 = 1, \tag{2}$$

where $\alpha_w = 1/x'^2_w$ and $\gamma_w = 1/x'^2_w$, and x_w and x'_w represent the half-width and half-divergence respectively. Connecting the ellipse coordinates x_t and x'_t at the target to x and x' at the post-target waist is a simple drift space transformation matrix. Thus, for a drift space L

$$\begin{pmatrix} x \\ x' \end{pmatrix} = \begin{pmatrix} 1 & L \\ 0 & 1 \end{pmatrix} \begin{pmatrix} x_t \\ x'_t \end{pmatrix}. \tag{3}$$

Combining the results of eqs. (2) and (3), the target ellipse can be expressed as

$$\alpha x_t^2 + 2\beta x_t x'_t + \gamma x'^2_t = 1, \tag{4}$$

where $\alpha = \alpha_w$, $\beta = \alpha_w L$, and $\gamma = \alpha_w L^2 + \gamma_w$. Solving eq. (4) for x_t and x'_t in turn permits determination of the intersection points $1/\sqrt{\alpha}$ and $1/\sqrt{\gamma}$ on the x_t and x'_t axes respectively, and the half-width and half-divergence as $\sqrt{\gamma} x_w x'_w$ and x'_w respectively, as shown in fig. 2a.

The relative reduction in divergence for an on-axis particle is defined by the ratio

$$R = 1/\sqrt{\gamma} \div x'_w = [1 + (L/X)^2]^{-\frac{1}{2}}, \tag{5}$$

where $X = x_w/x'_w$, is referred to as the characteristic length[5]). This ratio gives an indication of the improvement in resolution to be expected due to reduction of kinematic effects.

At the target the beam width is greater than at the waist by the ratio $\sqrt{\gamma} x_w x'_w/x_w = 1/R$.

The orientation of the ellipse on target is best described by first expressing eq. (4) in polar coordinates, $x_t/x_w = r\cos\theta$ and $x'_t/x'_w = r\sin\theta$, to yield

$$r^2[1 + (\gamma x'^2_w - 1)\sin^2\theta + \beta x_w x'_w \sin 2\theta] = 1. \tag{6}$$

The major and minor axes of the ellipse are then defined by $dr/d\theta = 0$, with the result that

$$\tan 2\theta = -\frac{2\beta x_w x'_w}{\gamma x'^2_w - 1}. \tag{7}$$

Along the axis labelled A–A in fig. 2a one then finds, using eq. (7)

$$x_t/x'_t = -\tfrac{1}{2}L\{1 + [1 + (2X/L)^2]^{\frac{1}{2}}\}. \tag{8}$$

Thus if X is known, the drift space L can be selected to yield a ratio x_t/x'_t equal to that given by eq. (1).

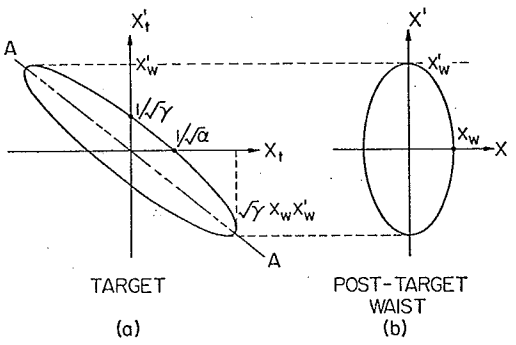

Fig. 2. Phase space ellipse in the horizontal plane for two locations separated by a drift space. The quantities α and γ are defined in section 3.

Curves of $-x_t/dx'_t$ as a function of θ for different values of α, calculated from eq. (1), are shown in fig. 3. It is to be noted that for $\theta=2\alpha$, this ratio is always unity. In a typical experimental situation the target–detector distance d has been fixed and a scattering angle θ, together with the target angle α, selected. The quantity x_t/x'_t is then obtained either from eq. (1) or the curves presented in fig. 3. The required value of L for a given X can then be read from the graphs of fig. 4, which were calculated from eq. (8). Also shown in this

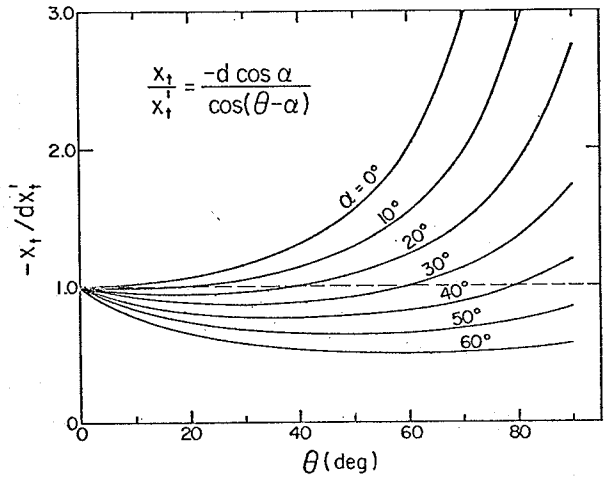

Fig. 3. Relationship between projectile trajectory slope and position on target to scattering (θ) and target (α) angle. The target–detector distance is d.

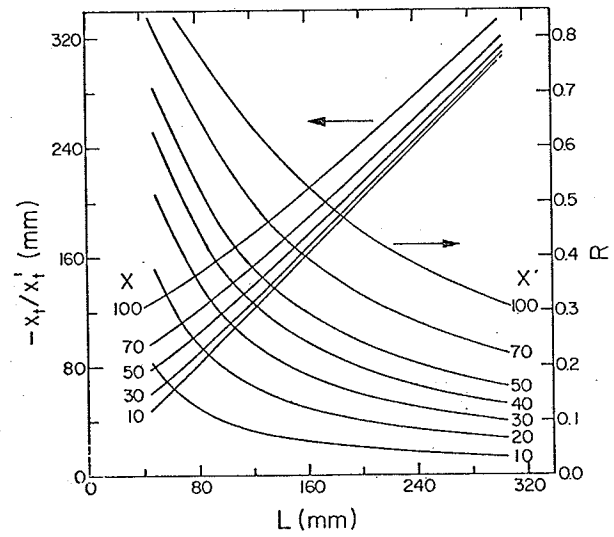

Fig. 4. Ratio x_t/x'_t for a projectile at the target as a function of L, the drift space to the post-target waist. R is an effective figure of merit indicating the reduction in the beam-divergence contribution to the resolution.

TABLE 1

Nuclear reaction and experimental parameters for the calculated and measured energy distributions.

Parameter	^{1}H(p,p)^{1}H	^{12}C(p,α)^{9}B$_{gs}$
I Reaction and geometrical details		
Incident proton energy (MeV)	42.5	35.2
Target thickness (μg/cm^2)	860 (mylar)	100 (carbon)
θ, scattering angle	63	40
α, target angle	30	20
β, detector rotation	33	20
d, detector distance (mm)	165	192.5
E_3, outgoing particle energy (MeV)	8.6	23.2
dE/dθ, kinematic spread (keV/deg)	600	108
X [a], characteristic length (mm/rad)	50	30
L, target–post-target waist distance (mm)	155	187
R, figure of merit	0.307	0.158
II Monte Carlo calculations: resolution fwhm (keV)		
(a) Waist at target ($L=0$)	720	192
(b) Waist beyond target (L = value given above)	125	18
III Experimental contributions to the measured resolution (keV)		
(a) Detector and electronics	35	35
(b) Detector angle[b]	60	11
(c) Energy loss, energy straggling and multiple scattering in the target	141	43
Total of above contributions[c]	157	57
IV Experimental results: resolution fwhm (keV)		
(a) Waist at target ($L=0$)		
Measured resolution	720	205
Beam divergence contribution[d]	703	197
(b) Waist beyond target (L = value given above)		
Measured resolution	260	63
Beam divergence contribution[d]	207	27

[a] $x_w = 0.5$ mm for all measurements and calculations.
[b] Position resolution of the PSD is 0.3 mm.
[c] Contributions added in quadrature.
[d] Experimental contribution subtracted from the measured resolution in quadrature.

figure is the ratio R, defined by eq. (5), an effective "figure of merit" for the reduction in the beam-divergence contribution to the resolution.

4. First-order transport calculations

A Monte Carlo program KCORR was written using

first order beam transport equations for the analysing magnets and quadrupoles, and energy distributions in the detector for given nuclear reactions were calculated. Details and parameters of the magnetic analysis system are given in ref. 1. Briefly summarized, the analysing system is comprised of two single-focusing 90° bending magnets of 76.2 cm bending radius. An intermediate image is formed between the two magnets which are symmetrically arranged with respect to the object and image distances. The energy resolution (fwhm) using 1 mm object and image slits is 25 keV at 50 MeV incident proton energy.

For the reactions investigated, $^{1}H(p,p)^{1}H$ and $^{12}C(p,\alpha)^{9}B_{gs}$, energy distributions were obtained for the cases $L=0$ (i.e. waist at target position) and for $L\neq 0$. In the latter case the appropriate value of L was calculated from eqs. (1) and (8), given the other parameters θ, α, d, X, etc. These quantities are summarized in table 1. The uncertain factor in these calculations was the characteristic length X, since this was found to vary from experiment to experiment, depending on the fine-tuning of the cyclotron. A value was selected that was consistent with the constraints of the divergence-limiting slit at the entrance to the first magnet, and one that yielded approximately the same resolution as that measured experimentally for $L=0$.

A further uncertainty was the distribution of particles over the area of the phase-space ellipse. Calculations were performed assuming Gaussian distributions that ranged from an essentially uniform distribution, to one where the particle density at the extremities of the ellipse was 30% of the central density.

These energy distributions are shown in figs. 5 and 6; for the $^{1}H(p,p)^{1}H$ reaction the resolution (fwhm) is reduced from a value of 720 keV for $L=0$ to a value of 125 keV at the appropriate L of the post-target waist, an improvement of a factor of about 6. In the case of the $^{12}C(p,\alpha)^{9}B_{gs}$ reaction the corresponding numbers are 192 keV and 18 keV, an improvement of almost a factor of 11. For comparison, the ratios $1/R$ are approximately 3 and 6 for these two cases respectively.

5. Experimental measurements with a position sensitive detector

The improvement in resolution demonstrated theoretically in the previous section is of limited practical value with a vanishingly small detector solid angle. A rather obvious solution is to replace the tightly colli-

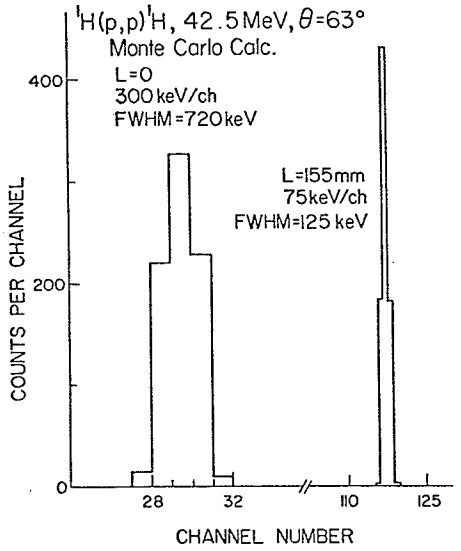

Fig. 5. Monte Carlo calculations for the energy distributions in the detector for a horizontal waist at the target position ($L=0$), and for the waist displaced downstream by 155 mm.

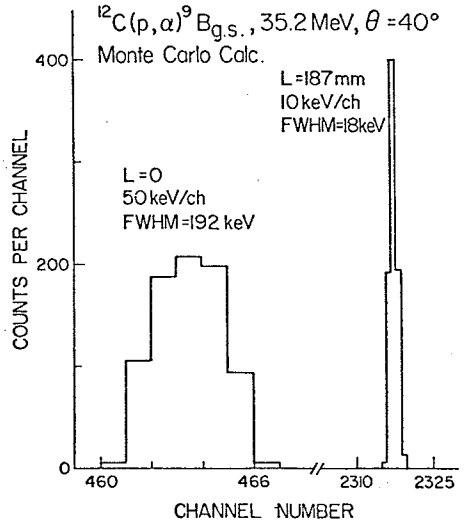

Fig. 6. Monte Carlo calculations for the energy distributions in the detector for a horizontal waist at the target position ($L=0$), and for the waist displaced downstream by 187 mm.

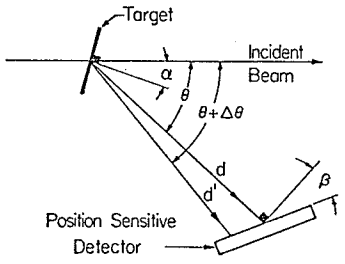

Fig. 7. Position sensitive detector geometry for kinematic matching conditions.

mated detector with a position sensitive detector (PSD) and use the position information to apply kinematic corrections from the angular information.

In order to use a larger portion of the length available in such detectors it is important to show that the condition specified by eq. (1) can be fulfilled for all points along the length of the detector. Referring to fig. 7, we require that

$$\frac{d' \cos\alpha}{\cos(\theta+\Delta\theta-\alpha)} = \frac{d \cos\alpha}{\cos(\theta-\alpha)}. \tag{9}$$

This condition can be satisfied, if $\Delta\theta$ is small, by rotating the detector from the normal position by the amount $\beta=\theta-\alpha$. [The actual locus of points defined by eq. (9) is a curve whose gentle curvature can be approximated by a straight line.]

A PSD counter 7×30 mm^2 and 1000 μm depletion depth was used in performing measurements for the two reactions just discussed. Pertinent experimental details are given in table 1. An off-line fortran program was used to calculate a two-dimensional kinematic correction matrix of excitation energy vs angle θ. This matrix was then introduced into the on-line data-taking program and appropriate corrections to the data were made on an event-by-event basis.

Several contributions to the experimentally measured resolution have to be subtracted before a comparison with the theoretical calculations can be made. These are the instrumental resolution of the detector system, the finite angular uncertainty due to the position resolution (0.3 mm) of the PSD, and energy loss, energy straggling and multiple scattering in the target. Contributions of 157 keV and 57 keV due to these effects are found for the ^{1}H(p,p)^{1}H and ^{12}C(p,α)^{9}B$_{gs}$ reactions as shown in the table.

The major difficulty in the experimental measurements was in the determination of the quadrupole field strengths for waist conditions at the target and post-target location. A quadrupole triplet located between the image slits and the scattering chamber in the present system provides a variable magnification lens system. Initially, detailed calculations using the code TRANSPORT[6]) had been carried out[1]) for the entire magnetic analysis system and the results for the final quadrupole triplet elements were used in subsequent calculations of waist-to-waist transfer according to the prescription given by Resmini[5]). (The image slits correspond very closely to a horizontal waist, and hence waist-to-waist transfer calculations from the image slits to the target or post-target waist form a quick and simple prescription for determining the quadrupole field strengths.) The calculated quadrupole settings were further investigated visually by observing the beam on a fluorescent BeO screen. Good qualitative correspondence between visual observations and calculations was obtained.

Experimental measurements for the ^{1}H(p,p)^{1}H reaction are shown in fig. 8, with resolutions of 720 and 260 keV for the $L=0$ and $L=155$ mm case respectively. Subtracting the experimental contributions of 157 keV discussed above, leaves contributions of 703 and 207 keV respectively for $L=0$ and $L=155$ mm due to the beam divergence. The improve-

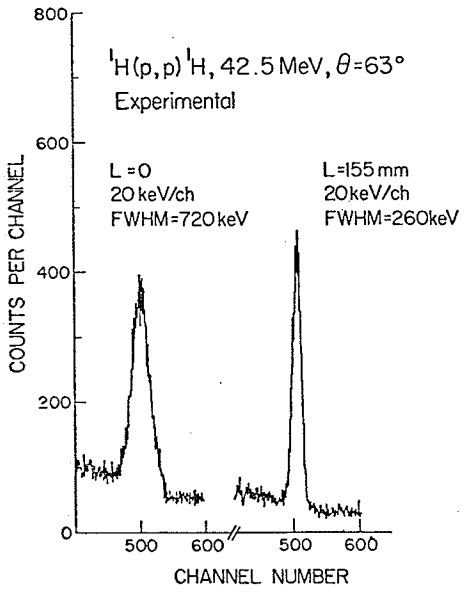

Fig. 8. Experimental measurements of the resolution for the ^{1}H(p,p)^{1}H reaction for $L=0$ and $L=155$ mm.

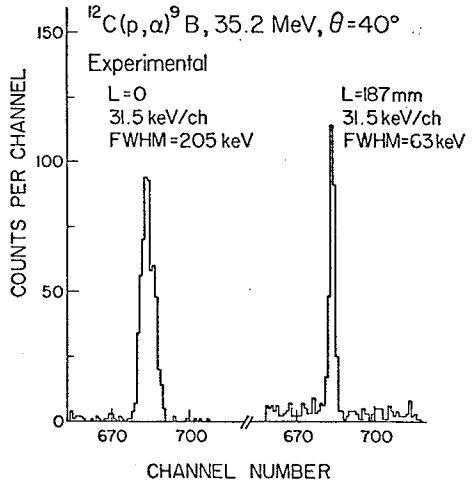

Fig. 9. Experimental measurements of the resolution for the ^{12}C(p,α)^{9}B$_{gs}$ for $L=0$ and $L=187$ mm.

ment is a factor of about $3\frac{1}{2}$ compared to 6 in the calculation. Similarly, fig. 9 displays the $^{12}C(p,\alpha)^{9}B$ measurements with the results of 205 and 63 keV for $L=0$ and $L=187$ mm respectively. Subtraction of the 57 keV experimental contribution leaves 197 and 27 keV as the contributions due to the divergence of the beam. Here the improvement is a factor of 7 compared to the calculated value of 11. For both these measurements the PSD was divided into six 5 mm long sections and appropriate kinematic corrections were applied within each section.

Second (and higher) order effects are known to be important[1]) in the magnetic analysis system and hence it is not surprising that the improvements in the measured resolutions are less than those predicted by simple first order calculations.

6. Conclusions

The method outlined for improving the energy resolution by shifting the horizontal waist to a point downstream from the target (for $\theta<\frac{1}{2}\pi$) has been demonstrated to be effective, although the experimental results show smaller improvements than the calculated values. Higher order effects in the beam preparation system (analysing magnets, quadrupoles, etc.) and detailed knowledge of the initial beam characteristics are clearly important in making more quantitative comparisons.

The method described in this paper should be of value in those experimental situations where the beam-divergence contribution to the energy resolution is larger than the intrinsic energy resolution of the beam itself, and where the detector either subtends a very small angle in the scattering plane, or provides position information.

References

[1]) University of Manitoba Cyclotron Laboratory Annual Report (1973–74) pp. 29, and to be published.

[2]) H. G. Blosser, G. M. Crawley, R. Deforest, E. Kashy and B. H. Wildenthal, Nucl. Instr. and Meth. **91** (1971) 61.

[3]) B. W. Ridley, D. E. Prull, R. J. Peterson, E. W. Stoub and R. A. Emigh, Nucl. Instr. and Meth. **130** (1975) 79.

[4]) J. J. Livingood, *The optics of dipole magnets* (Academic Press, New York and London, 1969) ch. 7.

[5]) F. Resmini, Nucl. Instr. and Meth. **68** (1969) 235.

[6]) K. L. Brown, F. Rothacker, D. C. Carey and Ch. Iselin, TRANSPORT, a computer program for designing charged particle beam transport systems, SLAC 91, Rev. 1, Stanford Linear Accelerator Center (1974).

Refrences

1. P. Debenham et al, Univ. of Man. Cyclotron progress report, 1972

3. J.J. Livingood, The optics of dipole magnets (Academic Press, New York, 1969)

4. K.L. Brown et al, TRANSPORT, a computer program for designing charged particles beam transport systems, SLAC91 Rev.1, Stanford Linac, (1974)

6. T.J. Devlin, Private communications

7. R.A. Batten et al, Nucl. Instr. and Meth., 136(1976) 6

8. J.J. Livingood, Cyclic particle accelator, Principles of (VONOstrand Co., New York, 1961)

9. J.J. Burgerjen et al, Nucl. Instr. and Meth., 43(1966)381

10. P. Marmier and E. Sheldon, Physics of Nuclei and Particles, Academic Press, New York, 1969

11. F. Resmini, Nucl. Instr. and Meth., 68(1969)235

13. Nuclear data tables, vol.7A, (Academic Press), 1970

14. A. Septier, Focusing of charged particles, Academic press, N.Y., 1967

15. H.G. Blosser et al, Nucl. Instr. and Meth., 91(1971)61